Fall 2016

Disorder Effects in Dirac Heterostructures

Martin Alexander Rodriguez-Vega
College of William and Mary, marodriguezveg@email.wm.edu

Recommended Citation

Disorder effects in Dirac heterostructures

Martin Alexander Rodriguez-Vega

Colima, Mexico

Master of Science, College of William and Mary, 2013
Bachelor of Science, Universidad de Colima, 2011

A Dissertation presented to the Graduate Faculty
of the College of William and Mary in Candidacy for the Degree of
Doctor of Philosophy

Department of Physics

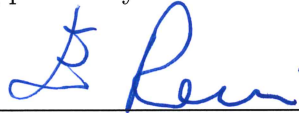The College of William and Mary
August 2016

APPROVAL PAGE

This Dissertation is submitted in partial fulfillment of
the requirements for the degree of

Doctor of Philosophy

_____
Martin Alexander Rodriguez-Vega

Approved by the Committee, May 2016

_____
Committee Chair
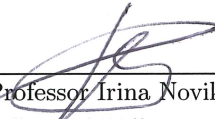Assistant Professor Enrico Rossi, Physics
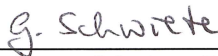The College of William and Mary

_____
Professor Shiwei Zhang, Physics
The College of William and Mary

_____
Professor Henry Krakauer, Physics
The College of William and Mary

_____
Associate Professor Irina Novikova, Physics
The College of William and Mary

_____
Dr. Georg Schwiete, Physics
Johannes Gutenberg Universität Mainz

ABSTRACT

In this dissertation, we study theoretically heterostructures based on Dirac materials, i.e. materials, such as graphene in which the electrons behave as massless Dirac fermions at low energies. We first examine how the presence of long-range disorder affects the electronic ground state of a double layer graphene heterostructure formed by two graphene layers separated by a thin dielectric film. We then identify the necessary conditions for the formation of an interlayer exciton condensate in such a system. We also comment on the effect of long-range disorder on the broken symmetry ground state induced by electron-electron interactions in bilayer graphene. Then, we study the transport properties of heterostructures obtained by stacking a graphene layer on the surface of a strong three-dimensional topological insulator (TI). In particular, we determine the non-equilibrium current-induced spin density accumulation for these systems using linear response theory and taking into account the effects of long- and short-range disorder both in the limit of strong and weak tunneling between the graphene layer and the TI. Finally, using some of the theoretical approaches developed to characterize the effect of long-range disorder in Dirac materials, we study the effect of long-range inhomogeneities in first-order phase transitions. In particular, we present a theoretical model to describe the effect of inhomogeneities on the relaxation dynamics of vanadium dioxide films after a photo-induced metal-insulator transition.

TABLE OF CONTENTS

ACKNOWLEDGMENTS

To my parents.

LIST OF TABLES

LIST OF FIGURES

DISORDER EFFECTS IN DIRAC HETEROSTRUCTURES

CHAPTER 1

Introduction

The isolation and identification of graphene [1], the theoretical proposal [2, 3] and later experimental realization of topological insulators [4, 5], along with previously known materials such as high-temperature d-wave superconductors [6] have given rise to a new class of materials, known as Dirac materials [7]. Despite the fact that they are very different in nature, all of them are characterized by an effective linear dispersion relation protected by various symmetries, depending on the particular material.

The recent development of experimental techniques related to the manipulation of 2D materials has allowed the creation of complex layered hererostructures based on Dirac materials [8–11] that combine individual properties to enhance or make emerge desirable properties for specific technological applications. However, the unavoidable presence of different kinds of disorder such as vacancies in the lattices, defects, charged impurities, etc. can undermine the system's capabilities. Hence, a detailed understanding of the disorder effects is imperative.

This dissertation focuses on the study of disorder effects in layered heterostruc-

tures composed of Dirac materials. In Chapter 2 we introduce the main building blocks of our heterostructures: graphene and topological insulators. In Chapter 3, we start with a detailed study of double-layer graphene heterostructures. These systems are fascinating because their experimental realization has opened up new interlayer Coulomb interaction regimes. Several experiments have revealed interesting physics. For example, Coulomb drag resistivity measurements have shown a strong zero-bias peak [11], indicating strong interlayer correlations. Also, metal-to-insulator transitions as a function of the charge carrier density have been observed [8]. The characterization of the electronic ground state nature, in the presence of inherent disorder due to charged impurities, allows a better understanding of all these phenomena. Therefore, we investigated the effect of long-range disorder in double-layer graphene heterostructures, determine the ground state properties, and explore in detail the parameter space. The theoretical description we present in this chapter is based on the work found in Ref. [12]. We then present a summary of experimental results of a collaboration between our theory group and the experimental group of Eva Andrei at Rutgers University on double-layer graphene heterostructures, where the screening properties of double-layer graphene systems are determined using different techniques. The results of this collaboration can be found in Ref. [13]. Also, we study the effect of long-range disorder on the possible broken symmetry ground states in bilayer graphene (BLG). BLG possesses an approximate SU(4) symmetry [14], which leads to a large variety of possible broken symmetry ground states driven by electron-electron interactions. Several experiments [15–23] have been performed to determine the nature of the BLG ground state, but results are not in agreement with each other. Previous theoretical works have addressed this issue, but the study of the effect of long-range disorder is still missing. This is a challenging problem because we have to carefully take into account the physics of electron-hole puddles,

and determine whether or not there is phase coherence in the system in the presence of disorder. We investigate the role that long-range disorder plays to drive the samples into one or another ground state, and determine self-consistently the charge density fluctuations and the order parameter.

In Chapter 4 we consider the possible formation of an exciton condensate in double-layer graphene heterostructures, which has been predicted near room temperature before [24, 25]. In collaboration with David Abergel (NORDITA), and Sankar Das Sarma (University of Maryland), we studied the effect of the charge density fluctuations induced by charged impurities on the formation of the exciton condensate and determined the experimental conditions under which this phenomenon is observable. The results of this work can be found in Ref. [26].

In Chapter 5, we consider the use of novel topological insulator-graphene-ferromagnet heterostructures for spintronic applications. This system combines the high mobility of graphene [27], with the strong spin-orbit coupling in topological insulators [28], to provide the ingredients necessary for the efficient manipulation of the ferromagnet magnetization direction using electric currents. We study in detail the non-equilibrium current-induced spin density accumulation and the transport properties of such heterostructures. A proper study of the system response requires to take into account the charged impurities usually present in Dirac systems [29–31]. Also, depending on the fabrication of the device, different coupling regimes can be obtained [32]. We first consider a weak coupling regime, dominated by random diffusive tunneling and calculate the disorder, and tunneling dressed graphene diffuson which allows us to compute the spin accumulation in the Kubo formalism. Then, we consider the strong coupling regime and assuming the presence of long-range disorder, we calculate the single particle lifetime and the transport time. We then calculate the non-equilibrium spin accumulation and conductivity.

In Chapter 6, we move away from Dirac materials and consider instead the interesting problem posed by vanadium dioxide VO_2 and its metal to insulator transition as a function of temperature. In collaboration with the Ale Lukaszew, and the Irina Novikova experimental groups (William and Mary), we did a combined theoretical-experimental study of the effect of inhomogeneities and the substrate on the metal-to-insulator transition in VO_2 thin films. We develop a model to describe the dynamics of the transition, taking the film inhomogeneities into account. The model is general, and can be applied to any first-order phase transition. This work can be found in Ref. [33].

Finally, in Chapter 7 we summarize the main results presented in this dissertation.

CHAPTER 2

Dirac materials.

Condensed matter systems with effective linear dispersion relations are known as Dirac materials [7, 34]. The most notable examples include graphene, the surface of three-dimensional (3D) topological insulators, high-temperature d-wave super-conductors, and 3D Weyl and Dirac semimetals. Despite the fact that the linear dispersion originates from different mechanisms in each of these materials, they all share common features in their transport properties, and response to perturbations.

Let us start by writing down the Dirac Hamiltonian [35]

$$H = cp_j \alpha^j + mc^2 \beta \ . \tag{2.1}$$

In Eq. (2.1), α and β are matrices that satisfy the anticommutation relations $\{\alpha^i, \alpha^j\} = 2\delta^{ij}$, $\{\alpha^i, \beta\} = 0$, and $\beta^2 = 1$. The Dirac equation, $i\hbar\partial_t\psi = H\psi$, describes the motion of free massive fermions of spin $1/2$. It is Lorentz invariant, and compat-ible with quantum mechanics. In covariant form it is given by $(i\gamma^\mu\partial_\mu - m)\psi = 0$, where the γ matrices satisfy the algebra $\{\gamma^\mu, \gamma^\nu\} = 2\eta^{\mu\nu}$, and η corresponds to the Minkowski space metric. One of the most interesting consequences of this equation

is the existence of solutions with negative energy, which were interpreted by Dirac as antiparticles. These antiparticles obey the same equation as the particles, with the only difference being that the charge changes sign, $q \to -q$.

In condensed matter systems, the Dirac Hamiltonian (2.1) emerges as an effective description of low-energy excitations. It is not a consequence of Lorentz invariance, but of the symmetries of particular systems. Some properties that are common for all Dirac materials [7] are, the specific heat temperature dependence, $C(T \to 0) \sim T^2$ in 2D, the square-root dependence of the Landau levels in the magnetic field and energy level $\epsilon_n = \sqrt{2e\hbar v^2 B |n|}$, backscattering suppression due to the chirality.

In the rest of this section, we introduce the main building blocks of the heterostructures we consider in this dissertation: topological insulators and graphene.

2.1   Graphene

Graphene is a two-dimensional array of carbon atoms arranged in a honeycomb lattice with an inter-carbon separation $a = 0.142$ nm. The honeycomb structure can be understood as a Bravais lattice with a basis, with primitive vectors $\vec{a}_1 = a/2(3, \sqrt{3})$, $\vec{a}_2 = a/2(3, -\sqrt{3})$, and basis $\{(0,0), (-a,0)\}$ (see Fig. (2.1a)). The motion of particles living on graphene can be described using a tight-binding Hamiltonian, which can be written in real space, taking into account nearest neighbor hopping, in the following way

$$H = -t_{nn} \sum_{\vec{R}, \{\vec{\delta}\}} c^{\dagger}_{A,\vec{R}} c_{B,\vec{R}+\vec{\delta}} \; + \; \text{h.c.} \,. \tag{2.2}$$
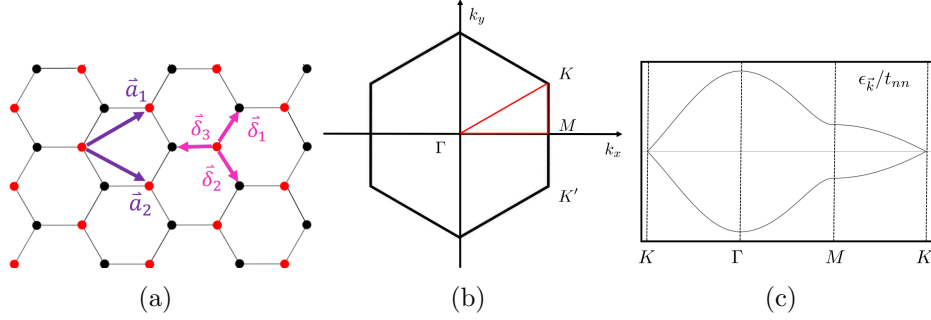
FIG. 2.1: (a) Graphene hexagonal lattice structure composed of two triangular sublattices. The $\vec{\delta}_i$ vectors indicate nearest neighbors, and $\vec{a}_i$ are the lattice vectors. (b) The hexagonal lattice Brillouin zone. (c) Graphene band structure along the red path in (b).

In Eq. (2.2), $c_{i,\vec{R}}^\dagger$ $(c_{i,\vec{R}})$ creates (annihilates) an electron in sublattice $i = \{A, B\}$, at position $\vec{R}$. The nearest-neighbor hopping is characterized by the parameter $t_{nn} \approx 2.7$ eV [36]. In the tight-binding description, we could have allowed for next nearest neighbor hopping characterized by the parameter t_{nnn}, which breaks particle-hole symmetry and introduces trigonal warping in the energy spectrum. However, t_{nnn} is considerable smaller than t_{nn}, with a ratio $t_{nnn}/t_{nn} \approx 0.13$, so this term is usually neglected [37]. The nearest neighbors are located at $\vec{\delta}_1 = \frac{a}{2}\left(1, \sqrt{3}\right)$, $\vec{\delta}_2 = \frac{a}{2}\left(1, -\sqrt{3}\right)$ and $\vec{\delta}_1 = a\left(-1, 0\right)$.

The Hamiltonian, Eq. (2.2), can be rotated to momentum space, where we obtain

$$H = -t_{nn} \sum_{\mathbf{k}} \tilde{f}_{\mathbf{k}} c_{A,\mathbf{k}}^\dagger c_{B,\mathbf{k}} + \text{h.c.} = \sum_{\mathbf{k}} \psi_{\mathbf{k}}^\dagger H_{\mathbf{k}} \psi_{\mathbf{k}} \ , \tag{2.3}$$

where $\tilde{f}_{\mathbf{k}} = \sum_{i=1}^{3} \exp\left(i\mathbf{k} \cdot \vec{\delta}_i\right)$. In the right side of Eq. (2.3) we have introduced the spinor $\psi_{\mathbf{k}}^\dagger = (c_{A,\mathbf{k}}^\dagger, c_{B,\mathbf{k}}^\dagger)$. The momentum Hamiltonian $H_{\mathbf{k}}$ acts in sublattice space,

and can be decomposed in the basis formed by the pseudospin Pauli matrices

$$H_{\mathbf{k}} = h_0(\mathbf{k})\sigma_0 + \vec{h}(\mathbf{k}) \cdot \vec{\sigma} \, , \tag{2.4}$$

where σ_0 is the identity matrix, and $\vec{\sigma} = (\sigma_x, \sigma_y, \sigma_z)$. In the case of graphene, the mass term $h_z(\mathbf{k})$ is identically zero due to inversion and time reversal symmetries. Under space inversion, sublattice $A \to B$, and momentum $\mathbf{k} \to -\mathbf{k}$, $I : H_{\mathbf{k}} = \sigma_x H_{-\mathbf{k}} \sigma_x$. Under time reversal $t \to -t$, $T : H_{\mathbf{k}} = H_{-\mathbf{k}}^*$, with $T^2 = 1$, for spinless particles. Then, combining both symmetries, $T \circ I : H_{\mathbf{k}} = \sigma_x H_{\mathbf{k}}^* \sigma_x$, which implies $h_z(\mathbf{k}) = 0$. The energy spectrum is given by $\epsilon_\pm(\mathbf{k}) = h_0(\mathbf{k}) \pm |\vec{h}(\mathbf{k})|$ for $\mathbf{k} \in$ BZ [38]. Fig. (2.1c) shows a plot the band structure along the path K-Γ-M-K, as depicted in red in Fig. (2.1b). The dispersion relation vanishes at the inequivalent corners of the BZ $\vec{K}$, and $\vec{K}'$ (valleys) where the bands become approximately linear for momentum much smaller the inverse lattice spacing. A Taylor expansion of the energy spectrum around the $\vec{K}$ point, with $\mathbf{k} = \vec{K} + \mathbf{q}$, $|\mathbf{q}|a \ll 1$, leads to the linear dispersion $\epsilon_{\mathbf{q}} = \pm v_F q + O\left((q/K)^2\right)$, where $v_F = 3ta/2 \approx c/300$, and c is the speed of light in vacuum.

An expansion of the momentum Hamiltonian around the K point leads to

$$H_{\mathbf{q}}^K = v_F \mathbf{q} \cdot \vec{\sigma} \, , \tag{2.5}$$

which corresponds to the Hamiltonian for 2D massless Dirac particles. Close the $\vec{K}'$ point, the effective Dirac Hamiltonian is given by $H_{\mathbf{q}}^{K'} = \left(H_{\mathbf{q}}^K\right)^*$. The existence of Dirac cones at the inequivalent K, and K' points of the triangular BZ gives rise to the valley degeneracy. These two valleys are usually decoupled unless lattice scale scattering is present [39].

Now, some remarks regarding the Hamiltonian $H_{\mathbf{q}}^K$ are in order. (i) $H_{\mathbf{q}}^K$ commutes with the chirality operator $\Lambda = \mathbf{k} \cdot \sigma / k$, which has eigenvalues ± 1. This fact indicates that the pseudospin is locked with the momentum direction (either parallel or antiparallel), which has implications for the transport properties of graphene, like the suppression of backscattering. (ii) In graphene, the intrinsic spin-orbit (SOC) coupling is insignificant [40]. Thus, the electron spin is practically decoupled from momentum, so at each valley, we find two decoupled spin up and spin down Dirac cones. (iii) The Dirac energy spectrum in graphene has been confirmed by several experiments, such as Angle resolved photo-emission spectroscopy (ARPES) [41, 42], Fourier transformed scanning tunneling spectroscopy (FT-STS) [43], and Landau level spectroscopy (LLS) [44].

2.2   Topological insulators

This introduction to topological insulators is based Refs. [28, 45, 46].

In mathematics, topology is the study of the transformation of objects under continuous deformations. An example of a problem in this area is the classification of closed surfaces. For the case of 2D surfaces, we can consider a sphere and a torus. The sphere cannot be smoothly deformed into the torus because the torus has a hole at the center. It is said that they are topologically distinct. The property that characterizes the surfaces is called the Euler characteristic [47] and is given by the integration of the Gauss curvature K over the entire surface,

$$\chi = \frac{1}{2\pi} \int_S K dA \,, \tag{2.6}$$

The Gauss curvature is the product of the smallest (κ_1) times the largest (κ_2)

curvature at a given point, $K = \kappa_1 \kappa_2$. The number of holes in the surfaces, the genus g, is related to the Euler characteristic through the relation $\chi = 2(1-g)$. For the sphere $g = 0$ while for the torus $g = 1$. This basic mathematical concept can be extended to condensed matter systems in the non-interacting approximation. In the presence of a periodic potential, the Bloch theorem states that the eigenstates of the Hamiltonian can be written as $|\psi(\mathbf{k})\rangle = e^{i\mathbf{k}\cdot\mathbf{r}}|u(\mathbf{k})\rangle$, where $|u(\mathbf{k})\rangle$ shares the same periodicity with the Hamiltonian and have eigenvalues $\epsilon(\mathbf{k})$. The eigenvalues define the band structure of the system. Within this picture, a band insulator is a system with a conduction and a valence band separated from each other by an energy gap where the Fermi energy lies. The Bloch states are invariant under the gauge transformation

$$|u(\mathbf{k})\rangle \rightarrow e^{i\phi(\mathbf{k})}|u(\mathbf{k})\rangle \ . \tag{2.7}$$

In analogy with the case of gauge invariance in electromagnetic fields, we can define the vector $\vec{A}_m(\mathbf{k}) = -i\langle u_m(\mathbf{k})|\nabla_\mathbf{k}|u_m(\mathbf{k})\rangle$, known as the Berry connection. Then, we can define a magnetic field analog, known as the Berry curvature $F_m(\mathbf{k}) = \nabla \times \vec{A}_m(\mathbf{k})$. For an insulator, the sum of $F_m(\mathbf{k})$ over the occupied states is an invariant,

$$\sum_m \int_{\text{occupied states}} F_m d\mathbf{k} = 2\pi n, \ \ n \in \mathbb{Z} \ . \tag{2.8}$$

where the integer n is known as the Chern number. Different values of this invariant identify different topological phases [28]. Two insulators are topologically equivalent if there exists an adiabatic path that transforms one insulator into the other without closing the gap, or equivalently, if they have the same topological index. If two topologically inequivalent insulators get into contact, the gap must close at the interface, leading to the formation of metallic edge states.

The first system discovered with non-trivial topology was the integer quantum

Hall (IQH) effect [48, 50]. Consider a 2D electron gas in the presence of a strong magnetic field. The energy spectrum is given by discrete Landau levels $\epsilon_n(\mathbf{k}) = \hbar\omega_c\left(n + \frac{1}{2}\right)$, where n is an integer and ω_c is the angular frequency. Due to the presence of the magnetic field, the electrons trace circular orbits of radius $l_B = \sqrt{\hbar/(eB)}$. Upon the application of an electric field, these orbits drift allowing for propagation along the edges. These edge states are chiral, and exhibit ballistic transport with no elastic backscattering. The Hall conductivity can be calculated using the Kubo formula [49, 50]

$$\sigma_{xy} = \frac{e^2}{h}n, \;\; n \in \mathbb{Z} \,, \tag{2.9}$$

where n is an integer that corresponds to the number of edge states in the sample. In Ref. [50], it was demonstrated by Thouless, Kohmoto, Nightingale, and den Nijs (TKNN) that the integer n in Eq. (2.9) corresponds to the Chern number which is identified as the topological invariant for IQH states. If $n = 0$ we have a trivial insulator. If $n > 0$, we have an IQH state with n edge modes.

The fact that the time reversal (TR) symmetry is broken is crucial for the existence of the IQH effect. A natural question to ask is, can we have topologically non-trivial systems with TR symmetry? The answer is yes. The first theoretical step towards the realization of a topological state with TR symmetry was made by Haldane [51], when he considered a hexagonal lattice with a fictitious magnetic field with different signs at each sublattice such that it vanishes on average. However, this magnetic field cannot be realized experimentally.

Here, spin-orbit coupling (SOC) enters the picture. SOC arises as a non-relativistic approximation to the Dirac Hamiltonian Eq. (2.1) [52]. The SOC term

is given by

$$H_{SOC} = -\frac{\hbar}{4m^2c^2}\sigma \cdot \vec{p} \times (\nabla V) \,, \qquad (2.10)$$

where V is the Coulomb potential. The main contribution to ∇V comes from atoms in the crystal. The SOC term can be thought of as a momentum dependent magnetic field that acts with opposite forces on different spins while preserving TR symmetry and breaking inversion symmetry. A consequence of the presence of SOC is the spin Hall (SH) effect [53–55], where an electric field induces a spin current transverse to the applied electric current. It can be thought of as the spin counterpart of the Hall effect [56]. This effect has been observed in semiconductors [57, 58]. The presence of strong enough SOC could lead to a state of matter known as the quantum spin Hall (QSH) state [2, 3]. Loosely speaking, the QSH state consists of two copies of the IQH state with opposite magnetic fields acting on opposite spins. At the edges of the insulating bulk, we find counter-propagating states, one for each spin. In this situation, the TR symmetry is not broken. The QSH phase is robust even when S_z is not conserved [59].

In the QSH state the Chern number vanishes so it cannot be used to classify QSH states. The topological invariant for the QSH state is the Z_2 invariant. Physically, whether or not this state presents topological order depends on the number of Kramers pairs at the edge. If we have an odd number of pairs, single-particle backscattering is not allowed. If an electron wants to backscatter, it must change its spin, but this is not allowed due to TR symmetry. Notice that there is no restriction on inelastic backscattering or two-body scattering processes. However, if there is an even number of Kramers pairs at the edge, there is an available counter-propagating state that allows for backscattering. This physical picture motivates the introduction of the Z_2 topological index, that classifies insulators as even or odd, with trivial

or non-trivial topology respectively. The Z_2 invariant also tells us the way in which the Krammers pairs are connected, as shown in Fig. (2.2). The situation in panel (a) corresponds to a trivial insulator, while the situation in (b) is associated with a QSH state. In the case of 2D systems, if S_z is conserved, spins up and down have independent Chern numbers $n_\uparrow$, $n_\downarrow$. Their difference $(n_\uparrow - n_\downarrow)/2$ defines a quantized spin Hall conductivity [28]. Below we provide a rigorous definition of the Z_2 invariant [60]. In the 2D BZ there are four TR symmetric points Λ_i. We define the expectation value of the TR operator T between these states with TR related momenta,

$$B_{\alpha\beta}(\mathbf{k}) = \langle -\mathbf{k}\alpha|T|\mathbf{k}\beta\rangle \ . \tag{2.11}$$

For spin-1/2 particles, $T^2 = -1$ with $T = e^{-i\sigma_y}K$, where K is the complex conjugate operator. At the TR invariant points, $B_{\alpha\beta}(\mathbf{k}) = -B_{\beta\alpha}(\mathbf{k})$, so the index δ_i can be defined by [60],

$$\delta_i = \frac{\sqrt{det(B(\Lambda_i))}}{Pf(B(\Lambda_i))} = \pm 1 \ . \tag{2.12}$$

Then, the Z_2 invariant ν is defined as

$$(-1)^\nu = \prod_{i=1}^{4} \delta_i \ . \tag{2.13}$$

A trivial insulator corresponds to $\nu = 1$, while $\nu = -1$ characterizes a QSH state. The first theoretical proposal for a QSH system was due to Kane and Mele [2], who suggested adding SOC to graphene. However, because SOC in graphene is weak, experiments have not been able to detect it. Soon after the first proposal for a SQH state, Bernevig *et. al.* proposed a heterojunction with strong SOC formed by cadmium telluride (CdTe) and mercury telluride (HgTe) [3]. The effective model consists of a Dirac Hamiltonian with masses of opposite signs for opposite
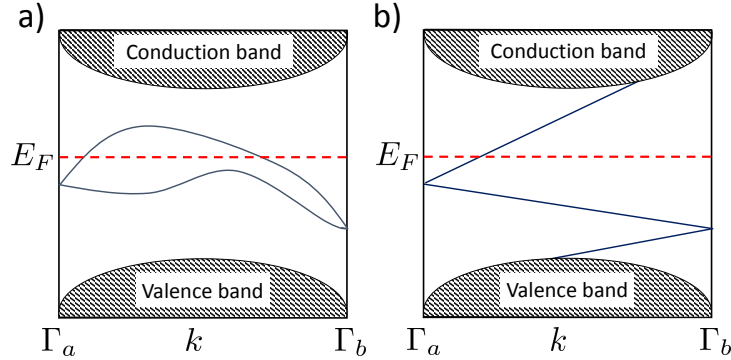
FIG. 2.2: Energy bands at the degenerate k-points Γ_a and Γ_b. (a) Shows an even number of states crossing the Fermi energy, the situation associated with a trivial insulator. (b) Shows an odd number of states crossing the Fermi energy, this situation leads to a topologically protected edge state.

spins. Soon after the theoretical proposal, measurements of the residual conductance $G = 2e^2/h$ gave confirmation of this effect [4, 61]. The term "2D TI" is a synonym of QSH effect. Other systems that host a QSH state have been proposed, for example, quantum wells made from InAs|GaSb|AlSb [62].

The next natural question is, can we have 3D TIs? In Refs. [63–65] 3D TIs were introduced. Under the single-particle approximation, and for clean systems, we can understand 3D TIs as a dimensional extension of 2D TIs. Consider a 2D projection plane of the 3D BZ. On this 2D plane projection, we have four TR invariant k-points. These points can be identified as Dirac points. How the states connect between these points defines whether or not we have a non-trivial topological state. The situation described here for one projection plane is analogous to what happens for 2D TIs. However, in the 3D case there are four Z_2 invariants. The first one, referred to as the strong topological invariant ν_0 is a scalar and tells us if there is an

even or odd number of Dirac points below the Fermi energy. It is given by [63, 66]

$$(-1)^{\nu_0} = \prod_{i=1}^{8} \delta_i \ .$$

(2.14)

The other three invariants are given by the product of four δ_i's lying on the same projected plane of the BZ. These three invariants define a vector, (ν_1, ν_2, ν_3). In principle, this gives rise to 16 different phases, but rotations of this vector connect several of these phases. If $\nu_0 = 0$, we have what is called a weak TI. This phase can be understood as a series of stacked 2D QSH systems, and is unstable against disorder. If $\nu_0 = 1$, we have a strong TI. The simplest case corresponds to the situation where we have only one Dirac point below the Fermi energy. The existence of another Dirac cone, with opposite chirality, on the opposite surface guarantees that the fermion doubling theorem [67] is satisfied. The surface states can be described by the effective Hamiltonian

$$H_S = \hbar v \left(k_y \sigma_x - k_x \sigma_y \right) \ ,$$

(2.15)

where v corresponds to the Fermi velocity, and the Pauli matrices σ_i are associated with spin [68]. These states are chiral, in the sense that the spin is locked with the momentum direction. The first material proposed to be a strong TI was the semiconducting alloy $Bi_{1-x}Sb_x$ [66]. Soon after the theoretical proposal, angle-resolved photoemission spectroscopy (ARPES) measurements were done to observe the surface states [69]. The second generation of topological insulator includes the compounds Bi_2Se_3, Bi_2Te_3, and Sb_2Te_3, which have a single Dirac cone on the surface [70] and larger band gaps compared to their first-generation counterparts. Systematic studies on these compounds have confirmed the topological band struc-

ture [71–75]. In this dissertation, we will focus on the surface states described by the Hamiltonian Eq. (2.15).

CHAPTER 3

Double-layer graphene heterostructures: Ground state in the presence of random charged impurities

3.1 Introduction

This chapter is based on Ref. [12]. As we have discussed in Chapter 1, the realization of single layer graphene (SLG) [1], bilayer graphene (BLG) [76], and other two-dimensional (2D) crystals [77], combined with recent advances in fabrication techniques [78, 79] in recent years has allowed the realization of novel 2D heterostructures [9, 10, 80–89]. In these structures, two or more 2D crystals are stacked in a designed sequence. Layers of hexagonal boron nitride (hBN) [27, 90, 91] have been used to electrically separate the graphenic layers (SLG or BLG) in multilayered

2D heterostructures. In particular, hBN allows the realization of graphene-based heterostructures in which the graphenic layers are very close and yet electrically separated [11, 92], a situation that is ideal to study the effects of interlayer interactions. It has been proposed that in these type of systems the interlayer interactions can drive the system into spontaneously broken symmetry ground states [93–98]. So far, experiments have not observed clear signatures of the establishment of these collective ground states. However, recent measurements of the drag resistivity in graphene double layers [11] have shown that the drag resistivity has a very large and anomalous peak when the doping in both graphene sheets is set to zero. This phenomenon indicates that a strong correlation is present between the carriers in the two layers. In most of the samples random charge impurities are present in the graphene environment, either in the substrate or trapped between the graphenic layer and the substrate. It has been shown theoretically [29] and experimentally [99–102] that the long-range disorder due to charge impurities induces strong, long-range, carrier density inhomogeneities in isolated SLG and BLG. The presence of random carrier density inhomogeneities has been predicted theoretically to strongly suppress the critical temperature (T_c) for the formation of an interlayer phase coherent state [26, 103, 104] in graphene heterostructures. This is in contrast to the short-range disorder that is not expected to suppress significantly T_c [98, 105, 106]. In addition, the presence of charge inhomogeneities, correlated in the two layers, is a necessary ingredient of the energy-transfer mechanism that has been proposed [107, 108] to explain the strong peak of the drag-resistivity at the double-neutrality point. Disorder-induced carrier density inhomogeneities are also expected to strongly affect the transport properties of graphene-based heterostructures [39, 109–113]. For these reasons, the accurate characterization of the carrier density inhomogeneities induced by long-range disorder in graphene-based heterostructures is essential to

understand the fundamental properties of these systems and to identify ways to increase their electronic mobility.

The characterization of the effects of disorder in graphene-based heterostructures is challenging for several reasons: (i) In most samples the disorder appears to be due predominantly to random charge impurities and to be quite strong and long-range, this fact makes the use of standard techniques, such as perturbation theory, not viable; (ii) Due to the linear dispersion in graphene, the screening of the long-range disorder due to the charge impurities is nonlinear; (iii) In graphene heterostructures the screening effects due to the different layers must be taken into account self-consistently; (iv) In bilayer graphene the presence of a perpendicular electric field opens a band-gap [114, 115]; (v) In heterostructures comprising BLG the component of the electric field perpendicular to BLG, and the BLG gap, must be obtained self-consistently taking into account the presence of the disorder and its screening by the metallic gates, and the other graphenic layer. In this work we present a systematic study of the effects of the long-range disorder due to random charge impurities on the ground state of graphene-based heterostructures taking into account all the effects mentioned above. As shown in Fig. 3.1 we consider heterostructures formed by two "graphenic" layers, either SLG or BLG, separated by a thin dielectric film. In the assumed configuration, using a top and a bottom gate, the doping of each graphenic layer can be set independently. We considered three classes of heterostructures: (i) double layer graphene (SLG-SLG) formed by two sheets of single layer graphene; (ii) double bilayer graphene (BLG-BLG) formed by two sheets of bilayer graphene; (iii) "hybrid structures" (BLG-SLG) formed by one sheet of BLG and one sheet of SLG. We find that the presence of charge impurities induces strong and long-range carrier density inhomogeneities in graphene-based heterostructures as in isolated SLG [29] and BLG [111]. However, for typical ex-

20

perimental situations we find that for the top graphenic layer the strength of the carrier density inhomogeneities is strongly suppressed due to the screening of the charge impurities by the bottom layer. We quantify this effect for most of the experimentally relevant conditions and find that for the top layer the amplitude of the density fluctuations can be reduced by an order of magnitude and that the effect is strongest in BLG-SLG heterostructures. We also show that the carrier density inhomogeneities in the different graphenic layers are well correlated. Finally, we show how the average band gap of BLG and its root mean square depend on the parameters, such as the impurity density, characterizing the heterostructure. Our results present a comprehensive characterization of the carrier density profile of graphene heterostructures in the presence of long-range disorder. By showing how the strength of the carrier density inhomogeneities depends on the experimental parameters, our results show how the quality of graphene-based heterostructures could be improved. In particular, the parameters that, within a certain range, can be easily tuned experimentally are the doping of each of the graphenic sheets forming the heterostructure, the type of graphenic sheets used, the impurity density (via annealing or the use of different substrates), and the distance between the graphenic sheets. For each of these parameters we present quantitative results that show how the values can be tuned to reduce the disorder strength in each of the graphenic sheets, or both, forming the heterostructure. The results presented in the remainder of this work, for instance, quantify how an increase of the doping in one of the two sheets forming the heterostructure can substantially reduce the strength of the disorder-induced long-range inhomogeneities in the other sheet, and quantify how much a reduction of the impurity density would reduce the strength of the disorder potential in the heterostructure. In addition, we show how a change of the distance between the two sheets can be optimized to reduce the overall disorder

strength in the heterostructure. Our results also show that, to reduce the strength of the disorder-induced long-range inhomogeneities in single layer graphene it is more efficient to have below it a sheet of bilayer graphene instead of SLG. The information on how to reduce, control, the disorder strength is essential for the study of fundamental effects in graphene heterostructures and for their use in technological applications.

3.2   Heterostructure model

Figure 3.1 presents a sketch of the type of graphene heterostructure that we consider. One graphenic layer (SLG or BLG), layer 1 in our notation is placed on an insulating substrate, typically SiO_2 . A thin buffer layer of high quality dielectric, typically hBN, might be present between the SiO_2 and the graphenic layer. A second graphenic layer, layer 2, is placed above the first one. Layer 2 and layer 1 are electrically isolated via a thin insulating film. The doping level of the two graphenic layers can be tuned independently via a top and a bottom gate.

There is compelling evidence [39] that in systems of the type depicted in Fig. 3.1 the dominant sources of disorder are random charge impurities located close to the surface of SiO_2 . It is known that on the surface of SiO_2 there is a large density of charge impurities. Transport measurements on single layer graphene have consistently observed a linear scaling of the conductivity with the doping (n), at low doping. The fact that the conductivity is suppressed at low dopings indicates that the effective strength of the disorder increases as the carrier density is decreased. Theoretical transport results in which charge impurities are the dominant source of scattering precisely predict at low dopings a linear suppression of the conductivity as n is decreased [39, 109, 116]. The agreement between transport theories

22

in which charge impurities are the main source of disorder and experimental transport measurements has also been confirmed by experiments in which the density of charge impurities was tuned [117]. In recent years there have been also several imaging experiments [99–102] that, close to the charge neutrality point, have observed the presence of electron-hole puddles with dimensions and amplitudes that are consistent with the presence of charge impurity densities in the graphene environment [29, 109, 110] of the order of the ones extracted from the transport results mentioned above.

The distribution of the charge impurities can be modeled as an effective 2D distribution $c(\mathbf{r})$ placed at a distance d below the bottom graphenic layer (layer 1). The dash-dot line in Fig. 3.1 shows schematically the location of the effective 2D plane where the random impurities are located. It is likely that some charge impurities will also be trapped between each graphenic sheet and the adjacent thin dielectric films. However, experimental evidence, especially for setups in which hBN is used as a dielectric material, strongly suggests that the density of such trapped impurities is at least an order of magnitude smaller that the density of the impurities close to the surface of the SiO_2 . For this reason we henceforth assume that the disorder potential is solely due to the charge impurities located close to the SiO_2's surface. Without loss of generality, we can assume $\langle c(\mathbf{r}) \rangle = 0$, where the angle brackets denote average over disorder realizations. Our formalism allows to easily take into account the presence of spatial correlation between the charge impurities [118, 119]. However, given the fact that in general the charge impurities are frozen and locked in a configuration that results from the fabrication process and that is not the thermodynamic equilibrium [120], we can assume that their position is uncorrelated so that $\langle c(\mathbf{r})c(\mathbf{r}') \rangle = n_{imp}\delta(\mathbf{r} - \mathbf{r}')$, where n_{imp} is the charge impurity density.
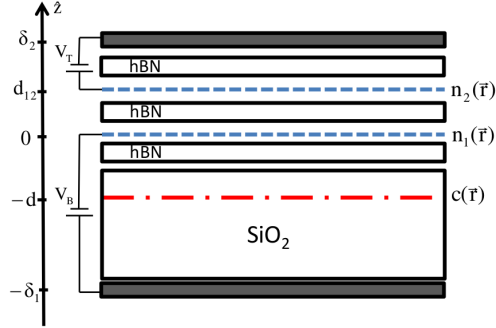
FIG. 3.1: Sketch of the typical graphene heterostructure considered in this work showing the graphenic layers (blue dashed lines) connected to independent metal gates (gray solid lines), isolated with hBN, and placed on a SiO_2 substrate. The charged impurities are modeled as a two-dimensional distribution $c(\mathbf{r})$ (red line) located at an effective distance d below the bottom graphenic layer.

At low energies the fermionic excitations of SLG are well described by a massless Dirac model with Hamiltonian [39, 121]:

$$H = \hbar v_F \, \sigma \cdot \mathbf{k} , \tag{3.1}$$

where $\hbar \mathbf{k}$ is the momentum operator, $\sigma = (\sigma_\mathbf{x}, \sigma_\mathbf{y})$ are the Pauli matrices in sublattice space, and $v_F \approx 10^6 \ \mathrm{ms^{-1}}$ is the Fermi velocity. Recent experiments for graphene on hBN have shown evidence of the opening of a gap [82, 122]. Considering that the fact that there is a 1.8% lattice mismatch between graphene and hBN and the fact that in current experiments a twist angle between the graphene layer and the hBN is normally present, the mechanism by which the gaps open is still not completely understood [108, 123], but is thought to be arising from the explicit breaking of the 'AB' sub-lattice symmetry in SLG due to the presence of the hBN substrate, and that it should not depend on the local electric field, but should depend on the twist angle between graphene and hBN in some complex manner. For our purposes this

means that for SLG on hBN the band-gap, if present, can be assumed to be fixed and independent of the local doping and electric field created by the nearby gates. In the presence of a band gap the low-energy Hamiltonian for single layer graphene becomes:

$$H = \begin{pmatrix} \Delta & \hbar v_F (k_x - ik_y) \\ \hbar v_F (k_x + ik_y) & -\Delta \end{pmatrix}.$$ (3.2)

At low energies the effective Hamiltonian describing the fermionic excitations in BLG is

$$H = \begin{pmatrix} \Delta & \frac{\hbar^2}{2m^*}(k_x - ik_y)^2 \\ \frac{\hbar^2}{2m^*}(k_x + ik_y)^2 & -\Delta \end{pmatrix},$$ (3.3)

where $m^* = 0.033 m_e$ is the effective electron mass and Δ is the band gap due a difference (U) in the electrochemical potential between the two layers of carbon atoms forming BLG. In our case, U is due to the presence of a perpendicular electric field $E_\perp$ induced by the metal gates, the other graphenic layer, and the charge impurities surrounding the BLG sheet. If BLG is layer 1, i.e. it is the graphenic layer closest to the charge impurities, we have:

$$E_\perp^{(1)}(\mathbf{r}) = \frac{e\, d}{\epsilon} \int d\mathbf{r}' \frac{c(\mathbf{r}')}{[|\mathbf{r} - \mathbf{r}'|^2 + d^2]^{3/2}} - \frac{e\, d_{12}}{\epsilon} \int d\mathbf{r}' \frac{n_2(\mathbf{r}')}{[|\mathbf{r} - \mathbf{r}'|^2 + d_{12}^2]^{3/2}}$$
$$- \frac{e\, \delta_1}{\epsilon} \int d\mathbf{r}' \frac{n_1(\mathbf{r}')}{[|\mathbf{r} - \mathbf{r}'|^2 + \delta_1^2]^{3/2}},$$ (3.4)

where d_{12} is the distance between the two graphenic layers and $\delta_1 \approx 300$nm is the distance between BLG and the bottom gate, Fig. 3.1. Notice that in general $E_\perp$ is not uniform, mostly due to the presence of the charge impurities. When BLG is

layer 2 we have:

$$E_\perp^{(2)}(\mathbf{r}) = (d + d_{12})\frac{e}{\epsilon}\int d\mathbf{r}'\frac{c(\mathbf{r}')}{[|\mathbf{r} - \mathbf{r}'|^2 + (d + d_{12})^2]^{3/2}} + \frac{e\,d_{12}}{\epsilon}\int d\mathbf{r}'\frac{n_1(\mathbf{r}')}{[|\mathbf{r} - \mathbf{r}'|^2 + d_{12}^2]^{3/2}}$$
$$+ (\delta_2 - d_{12})\frac{e}{\epsilon}\int d\mathbf{r}'\frac{n_2(\mathbf{r}')}{[|\mathbf{r} - \mathbf{r}'|^2 + (\delta_2 - d_{12})^2]^{3/2}} \ , \tag{3.5}$$

where $\delta_2 \approx 150$nm is the distance between the first graphenic layer and the top metal gate, Fig. 3.1. Using these expressions for the perpendicular component of the electric field we can calculate U. We have

$$U^{(i)}(\mathbf{r}) = e d_m E_\perp^{(i)}(\mathbf{r}) \ , \tag{3.6}$$

where $i = 1$ $(i = 2)$ if BLG is the bottom (top) graphenic layer, and $d_m = 0.335$nm is the BLG interlayer separation. Taking into account screening effects [124–126] the band gap of BLG due to a finite value of U is given by the equation

$$\Delta(x, y) = \frac{\gamma_1|U(x, y)|}{\sqrt{|U(x, y)|^2 + \gamma_1^2}} \ , \tag{3.7}$$

where $\gamma_1 = 0.34$ eV is the BLG interlayer tunneling amplitude [121].

3.3 Thomas-Fermi-Dirac theory

To obtain the ground state carrier density distribution in the presence of charge impurities we use the Thomas Fermi Dirac theory (TFDT). The TFDT is a generalization of the Thomas-Fermi theory to include cases in which the electronic degrees of freedom behave as massless Dirac fermions, as in single layer graphene. In this case both the kinetic energy functional and the functional due to the exchange part

of the Coulomb interaction are different from those valid for systems in which the electrons behave as massive fermions [29, 127]. In the TFDT the ground state of the system is obtained by minimizing the energy functional, $E[n]$, of the carrier density n. The TFDT is similar in spirit to the density functional theory (DFT), the difference being that in the TFDT the kinetic energy is also approximated by a functional of the density, $E_K[n]$, whereas in the DFT it is treated via the full quantum-mechanical operator acting on the wave function Ψ. The TFDT returns accurate results as long as the length-scale of the carrier density inhomogeneities $L_n \equiv |\nabla n/n|^{-1}$ is larger than the Fermi wavelength λ_F. Prior results on SLG [29, 111] and BLG [128, 129] have shown that in graphene-based systems this inequality is satisfied for typical experimental conditions. The value of n that enters in the inequality $L_n \gg \lambda_F$ is the typical local value inside the "puddles" characterizing the inhomogeneous carrier density landscape. At the charge neutrality point (CNP) $\langle n \rangle = 0$, however, everywhere the local density $n(\mathbf{r})$ is different from zero and therefore locally λ_F has a finite value. As a consequence, close to the CNP the average density cannot be taken as a measure of the typical carrier density inside the puddles and a better estimate is given by the density root mean square $n_{(rms)}$. Given that $n_{(rms)} \approx n_{imp}$ [29, 128] we have that the TFDT is valid at all densities as long as n_{imp} is not too small ($n_{imp} > 10^{11} cm^{-2}$) [130]. This is confirmed by prior results on SLG [29, 111] and BLG [128, 129]. The two major advantages of the TFDT are: (i) Being a functional theory is not perturbative with respect to the strength of the density fluctuations and can therefore take into account nonlinear screening effects; (ii) It is computationally very efficient and this makes the TFDT able to return disorder-averaged results.

For the systems of interest, the TFDT energy functional $E[n_i]$ will be a functional of the density profiles, $\{n_i(\mathbf{r})\}$, in the two graphenic layers. Neglecting exchange-

correlation terms that have been shown to be small for most of the situation we are interested in [29, 128], the general form of the functional $E[n_i]$ is:

$$E[n_i] = \sum_i E_K[n_i] + \sum_i \frac{e^2}{2\epsilon} \int d^2r \int d^2r' \frac{n_i(\mathbf{r})n_i(\mathbf{r}')}{|\mathbf{r} - \mathbf{r}'|} +$$
$$+ \sum_{i,j\neq i} \frac{e^2}{2\epsilon} \int d^2r \int d^2r' \frac{n_i(\mathbf{r}')n_j(\mathbf{r})}{\left[|\mathbf{r} - \mathbf{r}'|^2 + d_{ij}^2\right]^{1/2}}$$
$$+ e \sum_i \int d^2r V_D^i(\mathbf{r})n_i(\mathbf{r}) - \sum_i \mu_i \int d^2r n_i(\mathbf{r}) \qquad (3.8)$$

where ϵ is the dielectric constant of the medium surrounding the graphenic layers, d_{ij} is the distance between the graphenic layers, V_D^i is the bare disorder potential in layer i, and μ_i is the chemical potential in layer i. The second term in Eq. (3.8) is the Hartree part of the intralayer Coulomb interaction, the third term is the Hartree part of the interlayer Coulomb interaction, and the fourth is the one due to the disorder potential V_D^i. Assuming that charge impurities close to the surface of SiO_2 are the dominant source of disorder we have

$$V_D^{(1)} = \frac{e}{\epsilon} \int d\mathbf{r}' \frac{c(\mathbf{r}')}{[|\mathbf{r} - \mathbf{r}'|^2 + d^2]^{1/2}}; \qquad (3.9)$$
$$V_D^{(2)} = \frac{e}{\epsilon} \int d\mathbf{r}' \frac{c(\mathbf{r}')}{[|\mathbf{r} - \mathbf{r}'|^2 + (d + d_{12})^2]^{1/2}}. \qquad (3.10)$$

The ground state is obtained by minimizing E with respect to $\{n_i\}$. This gives rise to two coupled equations. In general, for the cases we are interested in, the term $\mu_{\text{kin}} \equiv \delta E_K / \delta n_i$ is nonlinear. For the case of gapless SLG μ_{kin} scales as the square-root of the density:

$$\mu_{\text{kin}}^{(SLG)}[n] = \hbar v_f \, \text{sgn}(n(\mathbf{r})) \sqrt{\pi |n(\mathbf{r})|}. \qquad (3.11)$$

For the case of gapped SLG we have

$$\mu_{\text{kin}}^{(SLG)}[n, \Delta] = \text{sgn}(n(\mathbf{r}))\sqrt{\hbar^2 v_f^2 \pi |n(\mathbf{r})| + \Delta^2} \tag{3.12}$$

For BLG, neglecting the presence of a nonzero band-gap (Δ), μ_{kin} depends linearly on n. This fact allows us to obtain analytical results for the carrier density ground state of BLG-BLG heterostructures in the limit $\Delta = 0$ (see Sec. 6.5). In the presence of a band gap the screening is strongly non-linear and this is reflected by the nonlinear dependence of μ_{kin} with respect to the density. Taking into account the band-gap for BLG we have

$$\mu_{\text{kin}}^{(BLG)}[n] = \sqrt{\left(\frac{\hbar^2}{2m^*}\right)^2 \pi^2 n^2 + \Delta^2}. \tag{3.13}$$

The nonlinearities due to the term $\delta E_K/\delta n_i$, and the need to self-consistently calculate Δ for systems involving BLG imply that the solution of the TFDT equations can only be achieved numerically. We then solve these equations for many (500-1000) disorder realizations to obtain disorder-averaged results. The need to consider many disorder realization to accurately obtain the disorder-averaged values of the quantities characterizing the ground state makes the computational efficiency of the TFDT approach very valuable.

3.4 Results

Figure 3.2 shows the profiles for a single disorder realization of the carrier density and of the screened disorder potential in each layer of a SLG-SLG heterostructure, at the neutrality point. We see that, as for the case of isolated SLG and BLG
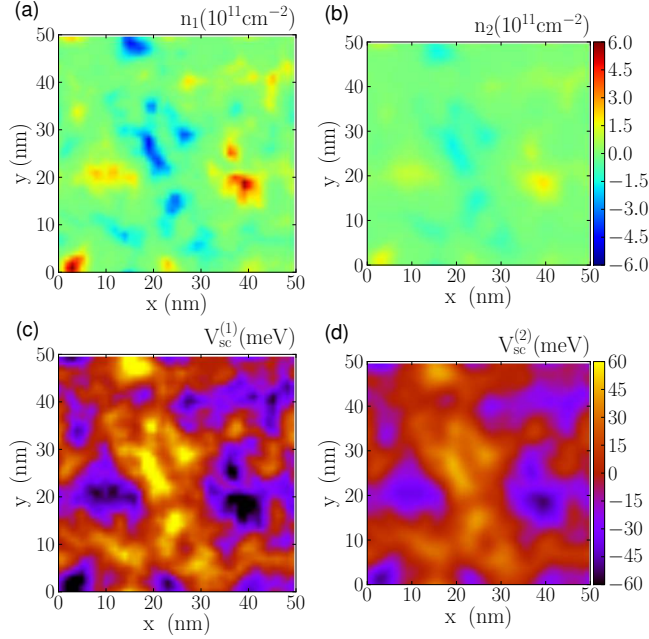
FIG. 3.2: (Color online). Color plots showing (a) $n_1(\mathbf{r})$, (b) $n_2(\mathbf{r})$, (c) $V_{sc}^{(1)}(\mathbf{r})$, and (d) $V_{sc}^{(2)}(\mathbf{r})$ for a SLG-SLG system at the charge neutrality point for a single disorder realization with $n_{imp} = 3 \times 10^{11} cm^{-2}$, $d = 1$ nm, and $d_{12} = 1$ nm.

[29, 39, 99–102], the carrier density profile breaks up in electron-hole puddles. We also notice that the amplitude of the density fluctuations and the strength of the screened disorder potential in the top layer is much smaller than in the bottom layer. This is due mostly to the screening of the charge impurities by the layer closer to the impurities. When the spectrum of SLG is gapped some regions of the samples will be insulating. This is shown by Fig. 3.3 which presents the density and screened disorder profiles for a single disorder realization in a SLG-SLG system in which the band-gap in both graphene layers is set equal to 20 meV. The white areas in Fig. 3.3 (a), (b) are insulating regions, i.e. regions in which the local chemical potential is within the band-gap and therefore contain no carriers. The results shown in Figs. 3.2,3.3 show how the profiles of the density and disorder of the top layer

30
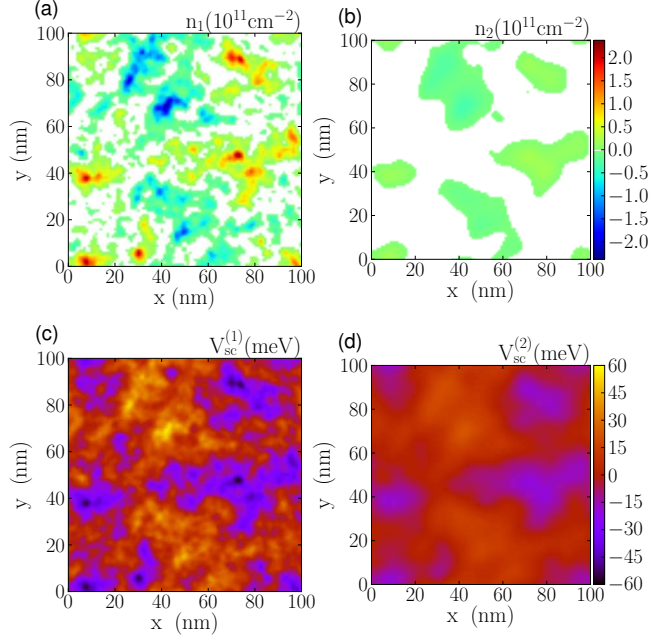
FIG. 3.3: (Color online). Color plots showing (a) $n_1(\mathbf{r})$, (b) $n_2(\mathbf{r})$, (c) $V_{sc}^{(1)}(\mathbf{r})$, and (d) $V_{sc}^{(2)}(\mathbf{r})$ for a SLG-SLG system at the charge neutrality point for a single disorder realization with $n_{imp} = 3 \times 10^{11} cm^{-2}$, $d = 1$ nm, $d_{12} = 1$ nm, and a finite band-gap $\Delta = 20$ meV in both layers.

and the bottom layer are different. The asymmetry between the profiles in the two layers will also be reflected in the transport properties as observed experimentally [8]. In particular, for our configuration in which the disorder is dominated by the charge impurities at the surface of the SiO_2, we see that in the presence of a gap the insulating regions are substantially larger in the top layer than in the bottom layer. We discuss the effect of this asymmetry on the qualitative features of electronic transport in section 3.5.
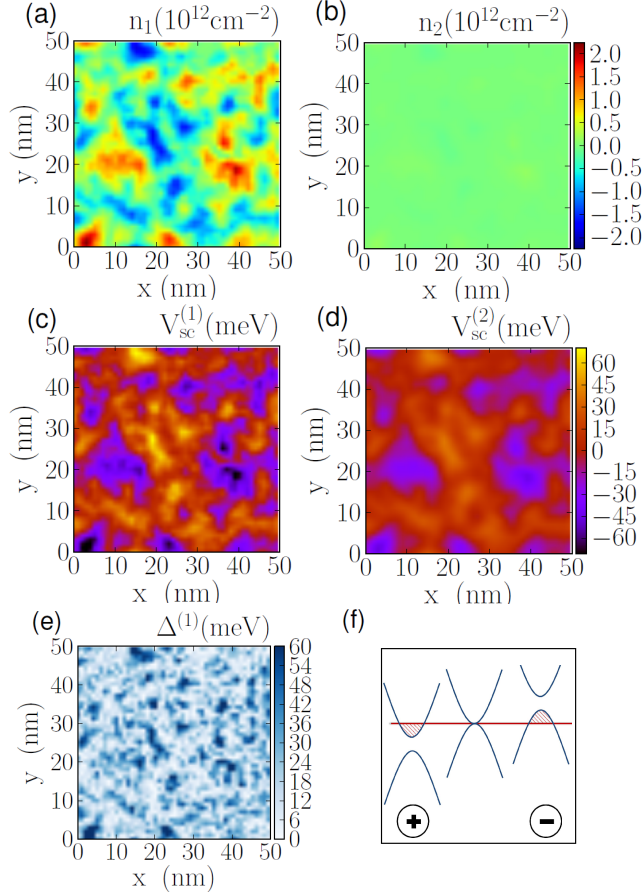
FIG. 3.4: (Color online). Color plots showing (a) $n_1(\mathbf{r})$, (b) $n_2(\mathbf{r})$, (c) $V_{sc}^{(1)}(\mathbf{r})$, (d) $V_{sc}^{(2)}(\mathbf{r})$ and (e) $\Delta^{(1)}$ corresponding to the BLG-SLG hybrid system at charge neutrality point for a single disorder realization, $n_{imp} = 3 \times 10^{11} cm^{-2}$, d = 1 nm, and $d_{12} = 1$ nm. (f) Sketch of the gapped BLG bands in the presence of disorder.

Figure 3.4 shows the profiles for a single disorder realization of the carrier density, panels (a) and (b), and screened disorder potential, panels (c) and (d), in each layer of a hybrid BLG-SLG heterostructure at the charge neutrality point. In comparing Fig. 3.2 (a) and Fig. 3.4 (a), we notice that the carrier density inhomogeneities are much stronger for BLG than SLG (all the rest being the same). This is due to the difference in the low-energy band structure between SLG and BLG. Due to this difference, the price in kinetic energy to create a density fluctuation at low

energies is much higher for SLG than BLG. Figure 3.4 (b) shows that the amplitude of the density fluctuations in the top layer (SLG) is much smaller in BLG-SLG than in the SLG-SLG. This is due to the fact that BLG, as the layer closer to the impurities, is much more efficient than SLG in screening the second layer from the disorder potential due to the charge impurities. This indicates that the mobility of SLG could be increased significantly when placed in a heterostructure in which the layer closest to the charge impurities is BLG. That this is the case is further confirmed by the disorder-averaged results that we present below.

Figure 3.4 (e) shows the profile for single disorder realization of the band-gap in BLG. We see that, due to the presence of the charge impurities, Δ is very inhomogeneous. In addition, we see that locally Δ can be as large as 60 meV. One could then wonder why in correspondence with the regions where Δ is large, the carrier density, Fig. 3.4 (a), locally does not go to zero. This is due to the fact that when the doping is set to zero in both layers the perpendicular electric field responsible for opening the band-gap is due to the charge impurities that we have assumed to be concentrated below the first layer. In these conditions, the regions in which $E_\perp$ is strong correspond to regions where the density of charge impurities is high and the induced carrier density is also high. In other words, for the conditions considered, regions where $\Delta \neq 0$ are also regions where the local value of the chemical potential is outside the gap as shown schematically in Fig. 3.4 (f). The scenario sketched in Fig. 3.4 (f) is not valid when a non-negligible density of charge impurities is also present above the top graphenic layers or between the two graphenic layers. Also, when the doping in one or both the two graphenic layers is not zero there will be a uniform contribution to $E_\perp$ and this can create regions where the chemical potential is within the gap.
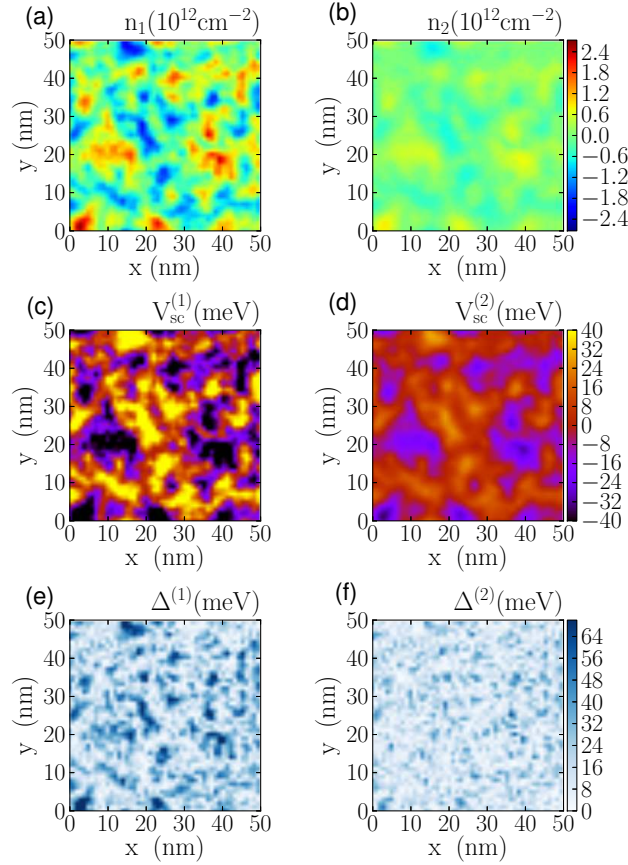
FIG. 3.5: (Color online). Color plots showing (a) $n_1(\mathbf{r})$, (b) $n_2(\mathbf{r})$, (c) $V_{sc}^{(1)}$, (d) $V_{sc}^{(2)}$, (e) $\Delta^{(1)}$, and (f) $\Delta^{(2)}$ corresponding to the BLG-BLG system at charge neutrality point for a single disorder realization, $n_{imp} = 3 \times 10^{11} cm^{-2}$, d = 1 nm, and d_{12} = 1 nm.

Figure 3.5 shows the profiles for single disorder realization of carrier density, screened disorder potential, and gap, in both layers of a BLG-BLG heterostructure, at the neutrality point. As for the other heterostructures, we see that the screening by the first layer considerably reduces the amplitude of the density inhomogeneities in the second layer and of the screened disorder potential. In addition, the band gap in the second layer is quite smaller than that in the first layer as we see in Fig. 3.5 (e), (f).

A quantitative comparison between the theoretical and the experimental results

34

is only possible by obtaining the disorder-averaged values of the quantities that are measured experimentally. In addition, the disorder-averaged characterization of the ground state carrier density distribution is an essential ingredient for the development of the transport theory in the presence of strong, disorder-induced, carrier density inhomogeneities [39].

For BLG-BLG heterostructures in the limit in which the band-gap Δ is zero, we can obtain analytic expressions for the disorder-averaged quantities that characterize the density profile and the screened disorder potential from the TFDT equations. Below we will show that in some situations the results obtained by setting $\Delta = 0$ provide results for for $n_{(rms)}$ and $V_{sc\,(rms)}$ that well approximate the results obtained by calculating Δ self-consistently. By minimizing the functional $E[n_1, n_2]$ of BLG-BLG structures with $\Delta = 0$ with respect to the density profile $n_1(\mathbf{r})$ in the first layer and the density profile $n_2(\mathbf{r})$ in the second layer we find:

$$
\begin{aligned}
n_i(\mathbf{q}) = & \frac{r_{sc}|\mathbf{q}|e^{|\mathbf{q}|d_{12}}}{\pi \left[e^{2|\mathbf{q}|d_{12}} \left(1 + |\mathbf{q}|r_{sc}\right)^2 - 1 \right]} \left[\frac{V_D^{(j)}(\mathbf{q})}{r_{sc}} - \frac{2m^*}{\hbar^2}\mu_j \delta(\mathbf{q}) + \right. \\
& \left. e^{|\mathbf{q}|d_{12}} \left(1 + |\mathbf{q}|r_{sc}\right) \left(\frac{2m^*}{\hbar^2}\mu_i \delta(\mathbf{q}) - \frac{V_D^{(i)}(\mathbf{q})}{r_{sc}} \right) \right]
\end{aligned}
\tag{3.14}
$$

where $n_i(\mathbf{q})$ is the Fourier transform of the carrier density profile in layer $i = 1, 2$, $j = 2$ (1) if $i = 1$ (2), and $r_{sc} = \epsilon\hbar^2/(2e^2m^*) \approx 3.2$ nm is the BLG screening length. Using the statistical properties of the impurity distribution $c(\mathbf{r})$ we can calculate the root mean square of the carrier densities $(n_{i(rms)})$ and the screened disorder potential

$$
V_{sc}^{(i)} = \frac{V_D^{(i)}(\mathbf{r})}{r_{sc}} + \frac{1}{2r_{sc}} \int d\mathbf{r}' \frac{n_j(\mathbf{r}')}{[|\mathbf{r} - \mathbf{r}'|^2 + d_{12}^2]^{1/2}} + \frac{1}{2r_{sc}} \int d\mathbf{r}' \frac{n_i(\mathbf{r}')}{|\mathbf{r} - \mathbf{r}'|}.
\tag{3.15}
$$

35

We find:

$$n_{i(rms)} = \left[\frac{2}{r_{sc}^2 \pi} n_{imp} I_i \left(\frac{d}{r_{sc}}, \frac{d_{12}}{r_{sc}} \right) \right]^{1/2}, \tag{3.16}$$

$$V_{sc(rms)}^{(i)} = \frac{\hbar^2 \pi}{2m^*} n_{i(rms)}, \tag{3.17}$$

$(i = 1, 2)$ where

$$I_1(x, y) = \int_0^\infty dz z e^{-2xz} \frac{[1 - e^{2yz}(1+z)]^2}{[1 - e^{2yz}(1+z)^2]^2}, \tag{3.18}$$

and

$$I_2(x, y) = \int_0^\infty dz \; \frac{z^3 e^{2z(y-x)}}{[1 - e^{2yz}(1+z)^2]^2} . \tag{3.19}$$

Figure 3.6 shows the scaling of $n_{(rms)}$ (and $V_{sc\ (rms)}$) in the two layers as a function of d/r_{sc} and d_{12}/r_{sc}. As d increases the amplitude of the carrier density inhomogeneities decreases rapidly. As d_{12} increases, $n_{1(rms)}$ approaches the value found for a single BLG sheet [129] whereas $n_{2(rms)}$ decreases exponentially to zero.
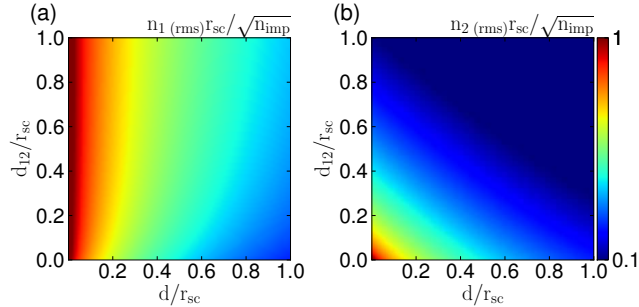
FIG. 3.6: (Color online). Color plots of (a) $n_{1\ (rms)} r_{sc}/\sqrt{n_{imp}}$, and (b) $n_{2\ (rms)} r_{sc}/\sqrt{n_{imp}}$ as a function of d/r_{sc}, and d_{12}/r_{sc} as obtained in equation 3.16.

As discussed in Sec. 3.2 when SLG is one of the constituents of the heterostructure, and/or when the BLG's band-gap cannot be neglected, the TFDT equations can only be solved numerically due to the nonlinearity induced by the kinetic energy term. Below we present our results for the disorder-averaged quantities. Apart

when explicitly indicated, all the results were obtained for 160×160 nm samples with a spatial coarse-graining of 1 nm [131, 132]. For each case we used a number of disorder realizations, N_S, large enough to guarantee that the results would not change if a larger number of disorder realizations were used. For the cases presented below we find that the results do not depend on N_s when N_s is larger than 500.
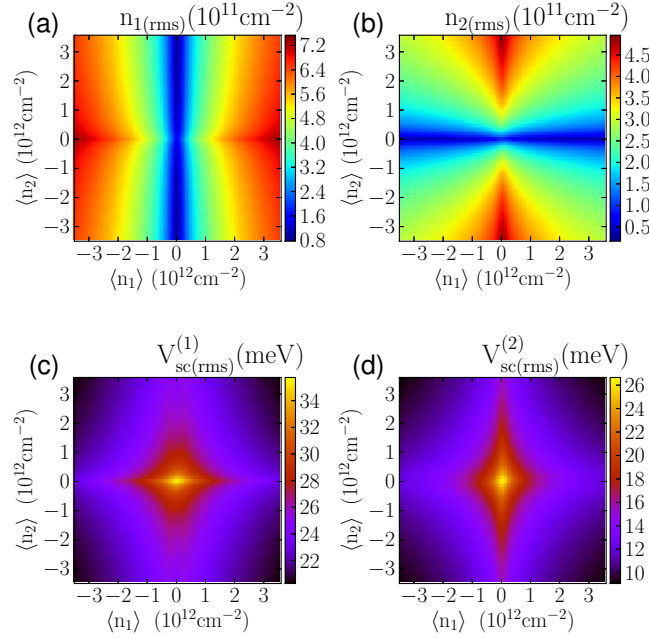
FIG. 3.7: (Color online). Color plots of (a) $n_{1\,(rms)}$, (b) $n_{2\,(rms)}$, (c) $V^{(1)}_{sc\,(rms)}$, and (d) $V^{(2)}_{sc\,(rms)}$ for SLG-SLG system as a function of the average carrier density for $n_{imp} = 3 \times 10^{11} cm^{-2}$, $d = 1$ nm, and $d_{12} = 1$ nm.

Figure 3.7 shows the root mean square of the carrier density and of the screened disorder potential in each layer of a SLG-SLG heterostructure. We see that the amplitude of the carrier density fluctuations in the first layer increases with $\langle n_1 \rangle$ and depends quite weakly on $\langle n_2 \rangle$. Analogously, $n_{(rms)}$ in the second layer increases with $\langle n_2 \rangle$. This is due to the fact that as the doping increases more carriers are available to screen the disorder potential by creating high density electron (hole) puddles in

correspondance of the valleys (peaks) of the bare disorder potential. However, we see that $n_{2(\text{rms})}$ also depends significantly on $\langle n_1 \rangle$. This is due to the fact that the first layer, being the closest to the charge impurities, is most responsible for the screening of the disorder potential and therefore significantly affects the amplitude of the density fluctuations in the second layer. Both $\langle n_1 \rangle$ and $\langle n_2 \rangle$ contribute to a decrease of the screened disorder potential in layer 1 and layer 2, as show by Fig. 3.7 (c) and (d). The results of Fig. 3.7 (b) and (d) confirm the conclusion that we derived from the single disorder realization results: due to the screening effect of the first layer the amplitude of the carrier density inhomogeneities and the strength of the screened disorder potential are weaker in layer 2 than in layer 1.
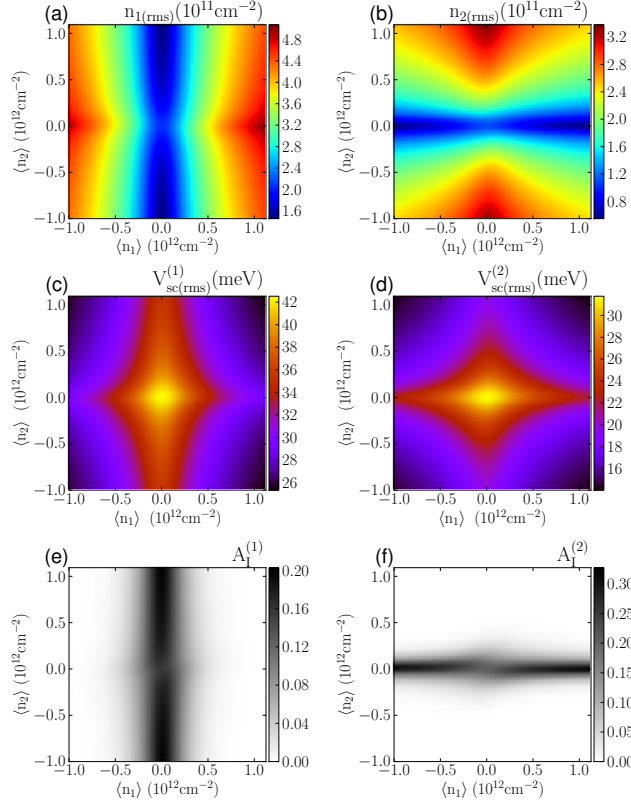
FIG. 3.8: (Color online). Color plots of (a) $n_{1\,(rms)}$, (b) $n_{2\,(rms)}$, (c) $V_{sc\,(rms)}^{(1)}$, (d) $V_{sc\,(rms)}^{(2)}$, (e) fraction of the area of the sample that is insulating in layer 1, $A_I^{(1)}$, and (f) fraction of the area of the sample that is insulating in layer 2, $A_I^{(2)}$, for SLG-SLG system with finite band-gap as a function of the average carrier density for $\Delta = 20$ meV, $n_{imp} = 3 \times 10^{11}$cm^{-2}, d = 1 nm, and d$_{12}$ = 1 nm.

In presence of a band-gap in the graphene spectrum for SLG-SLG systems, the dependence of $n_{(rms)}$ and $V_{sc\,(rms)}$ on $\langle n_1 \rangle$ and $\langle n_2 \rangle$ is qualitatively similar to the gapless cases. In the presence of a gap it is interesting to also look at how the fraction of the area of graphene that is insulating, $A_I^{(1)}$ ($A_I^{(2)}$) for layer 1 (2), depends on the doping in the two layers, see Figs. 3.8 (e), (f). For relatively large impurity densities, such as considered for the results shown in Fig. 3.8 (e), (f), A_I in layer 1 depend only weakly on the doping of layer 2, and vice versa. However, as we show

39

in Fig. 3.15, and as we discuss in section 3.5, this is not the case at low impurity densities. In practice we have that when the screened disorder $V_{sc\ (rms)} \lesssim \Delta$ the effect of layer j on A_I of the other layer can be very significant.
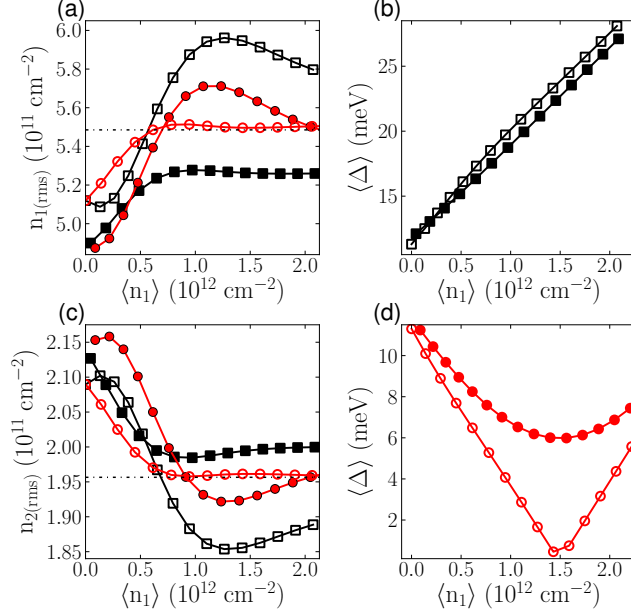
FIG. 3.9: (Color online). Plot of (a) $n_{1(rms)}$ and (c) $n_{2(rms)}$ as a function of $\langle n_1 \rangle$ for $n_{imp} = 2 \times 10^{11} cm^{-2}$, $d_{12} = 1nm$, and d= 1nm. The squares symbols correspond to $\langle n_2 \rangle = 1.5 \times 10^{12} cm^{-2}$, and the circle symbols correspond to $\langle n_2 \rangle = -1.5 \times 10^{12} cm^{-2}$. The curves with open symbols show the results obtained keeping Δ fixed, whereas the curves with solid symbols show the results obtained by calculating Δ self-consistently. $\langle \Delta \rangle$ is shown in subplots (b) and (d) also as a function of $\langle n_1 \rangle$. The dashed lines correspond to the case $\Delta = 0eV$ for both values of $\langle n_2 \rangle$, since the gapless BLG-SLG system is even in $\langle n_2 \rangle$.
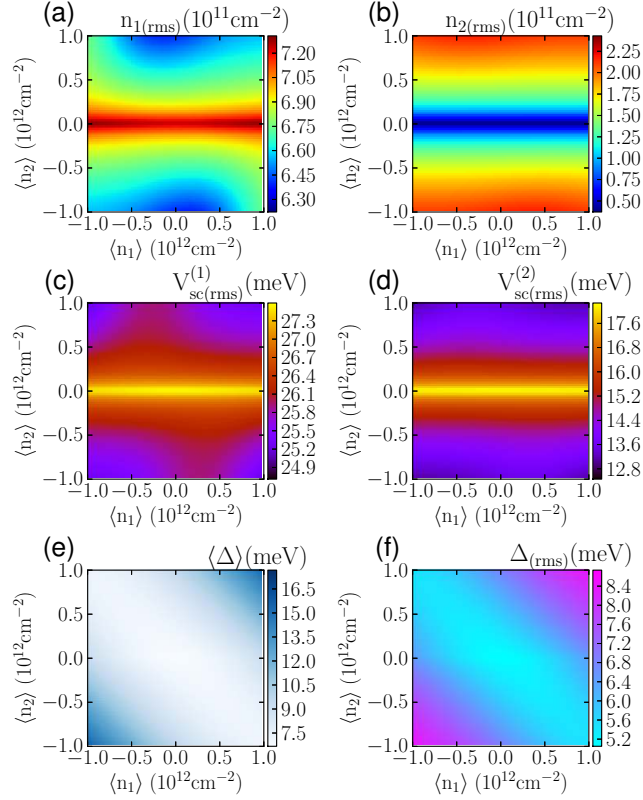
FIG. 3.10: (Color online). Color plots of (a) $n_{1\,(rms)}$, (b) $n_{2\,(rms)}$, (c) $V^{(1)}_{sc\,(rms)}$, (d) $V^{(2)}_{sc\,(rms)}$, (e) $\langle \Delta \rangle$, and (f) Δ_{rms} for BLG-SLG system as a function of the average carrier density for $n_{imp} = 3 \times 10^{11} cm^{-2}$, $d = 1$ nm, and $d_{12} = 1$ nm.

For heterostructures in which BLG is present we need to account for the opening of a band-gap due to the presence of a perpendicular electric field. The calculation of the band-gap has to be done self-consistently due to the fact that the redistribution of the charges in the layer forming the heterostructure modifies the profile of the perpendicular component of the electric field, affecting the profile of the band-gap that itself affects the screening properties of the heterostructure. To test the importance of self-consistently calculating the profile of Δ for a set of cases for BLG-SLG structures, we first performed the calculation setting Δ equal to the value obtained from Eqs. (3.4), (3.6), (3.7) in the limit of homogeneous density profiles in the two

layers, with $n_1 = \langle n_1 \rangle$, and $n_2 = \langle n_2 \rangle$. We then redid the calculation by obtaining $\Delta(\mathbf{r})$ self-consistently. The comparison of the two sets of results is shown in Fig. 3.9 in which $n_{(rms)}$ in the two layers and the average gap ($\langle \Delta \rangle$) are plotted as a function of $\langle n_1 \rangle$ for a fixed, non zero, value of $\langle n_2 \rangle$: the curves with open symbols show the results obtained keeping Δ fixed, whereas the curves with solid symbols show the results obtained by calculating Δ self-consistently. We see that in general the value of $n_{(rms)}$ obtained using the two approaches differ. For the case in which $\langle n_1 \rangle \langle n_2 \rangle > 0$ we have that the value of $\langle \Delta \rangle$ obtained self-consistently is reasonably approximated by the fixed value, Δ_{fixed}, obtained assuming uniform carrier density profiles. However, for $\langle n_1 \rangle \langle n_2 \rangle < 0$ we find that the value of $\langle \Delta \rangle$ is significantly different from Δ_{fixed}, Fig. 3.9 (d). The results of Fig. 3.9 show that the effect of the disorder cannot be captured by a simple average of a spatially homogeneous theory and requires a self-consistent calculation of the parameters defining the local band-structure. All results that we present for heterostructures in which BLG is present were obtained calculating Δ self-consistently.
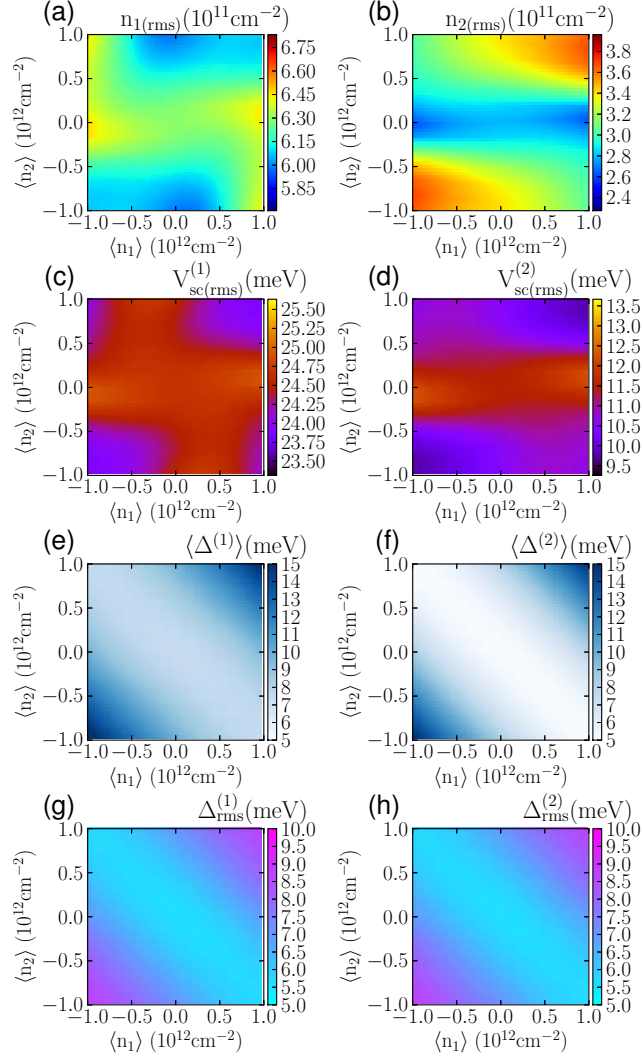
FIG. 3.11: (Color online). Color plots of (a) $n_{1\,(rms)}$, (b) $n_{2\,(rms)}$, (c) $V^{(1)}_{sc\,(rms)}$, (d) $V^{(2)}_{sc\,(rms)}$, (e) $\langle\Delta^{(1)}\rangle$, (f) $\langle\Delta^{(2)}\rangle$, (g) $\Delta^{(1)}_{rms}$, and (h) $\Delta^{(2)}_{rms}$ for BLG-BLG system as a function of the average carrier density for $n_{imp} = 3 \times 10^{11} cm^{-2}$, d = 1 nm, and $d_{12} = 1$ nm.
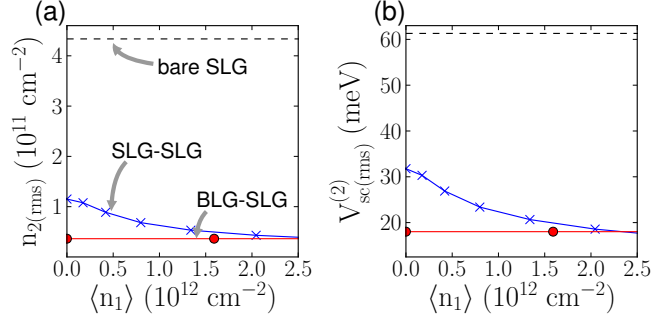
FIG. 3.12: (Color online). Plots of (a) $n_{2 \text{ (rms)}}$ and (b) $V^{(2)}_{\text{sc (rms)}}$ as a function of the carrier density on the graphenic layer closest to the impurities. The blue crosses correspond to the SLG-SLG system, the red circles correspond to the BLG-SLG system, and the black dashed curve correponds to bare SLG.

For a fixed n_{imp}, d, d_{12}, Fig. 3.10 shows the dependence of the disorder averaged quantities characterizing the ground state of a BLG-SLG structure on the $\langle n_1 \rangle$ and $\langle n_2 \rangle$. We see that amplitude of the density fluctuations and the strength of the screened disorder potential at low dopings depend almost exclusively on $\langle n_2 \rangle$, the average carrier density in SLG, and only very weakly on $\langle n_1 \rangle$, the average carrier density in BLG. This is due to the fact that at low dopings the band gap in BLG is quite small and so the density of states (DOS) of BLG is to good approximation constant, independent of $\langle n_1 \rangle$. On the other hand, in SLG, due to the linear band dispersion, the DOS depends linearly on the doping $\langle n_2 \rangle$. As a consequence at low dopings a change of $|\langle n_1 \rangle|$ has a negligible effect on the screening properties of the system whereas an increase (decrease) of $|\langle n_2 \rangle|$ increases (decreases) the screening due to the second layer, SLG. At high dopings the situation is complicated by the effect that a high average density on each layer has on the size of the gap in BLG, as shown in Fig. 3.10 (e). As a consequence the DOS in BLG is no longer almost independent of $\langle n_1 \rangle$. This causes dependence of $n_{\text{(rms)}}$ and $V_{\text{sc (rms)}}$ on the value of $\langle n_1 \rangle$. In particular, the asymmetry of $n_{\text{(rms)}}$ and $V_{\text{sc (rms)}}$ with respect to $\langle n_1 \rangle$, for

44

large values of $\langle n_2 \rangle$, is due to the asymmetric dependence of Δ on $\langle n_1 \rangle$, Fig. 3.10 (e). Figure 3.10 (f) shows the root mean square of Δ, $\langle \Delta_{rms} \rangle$. We see the $\langle \Delta_{rms} \rangle$ is in general of the same order of Δ, indicating the inhomogeneities of the band-gap in BLG are quite strong and cannot be treated perturbatively. In addition, we see that, qualitatively, $\langle \Delta_{rms} \rangle$ depends on $\langle n_1 \rangle$ and $\langle n_2 \rangle$ in a similar way to $\langle \Delta \rangle$. Another important feature of the results of Fig. 3.10 to notice is that when both $|\langle n_1 \rangle|$ and $|\langle n_2 \rangle|$ are large the size of the gap in BLG is comparable to the strength of the screened disorder potential. In these conditions we expect that the transport properties might be significantly affected by the presence of the band-gap and that BLG might behave as a bad-metal [129].

We now consider the BLG-BLG heterostructure. In this case both the top layer and the bottom layer can have a gapped band structure. Due to the fact that the band gap in both layers depends asymmetrically on $\langle n_1 \rangle$ and $\langle n_2 \rangle$, Fig. 3.11 (e), (f), we find that $n_{(rms)}$ and $V_{sc\,(rms)}$, in both layers, depend asymmetrically on the average carrier density of each layer, as shown in Fig. 3.11 (a)-(d). We also find that in both layers the r.m.s. of the band gap is of the same order as $\langle \Delta \rangle$ and that it scales with $\langle n_1 \rangle$ and $\langle n_2 \rangle$ qualitatively as $\langle \Delta \rangle$. We notice that for the bottom layer the average band-gap is never larger than the r.m.s of screened disorder potential. On the other hand, for the top layer we have that at large $|\langle n_1 \rangle|$ and $|\langle n_2 \rangle|$ the average gap is larger than $V_{sc(rms)}^{(2)}$. As a consequence we expect that when $|\langle n_1 \rangle|$ and $|\langle n_2 \rangle|$ are large the bottom layer will behave as a bad metal and the top layer as a bad insulator [129].

By comparing the results of Fig. 3.7, 3.10, and 3.11, we see that the three heterostructures, SLG-SLG, BLG-SLG, BLG-BLG, exhibit disorder-induced density fluctuations of comparable magnitude, and comparable strengths of the screened disorder potential. These results suggest that the effect of disorder on the estab-

lishment of collective ground states that has been proposed for SLG-SLG [93–98] BLG-SLG [98], and BLG-BLG [133] should be comparable.

It is interesting to compare the amplitude of $n_{(rms)}$ and of $V_{sc\ (rms)}$ for SLG when isolated and when part, as top layer, of one of the heterostructures considered. Figure 3.12 presents such a comparison. As we had anticipated above we see that $n_{(rms)}$ and $V_{sc\ (rms)}$ in SLG are much lower when part of a heterostructure, due to the screening of the disorder by the bottom layer, than when isolated. From the results of Fig. 3.12 we see that when the doping in the bottom layer is $\sim 10^{12}\text{cm}^{-2}$ $n_{(rms)}$ can be reduced by an order of magnitude thanks to the screening of the disorder by the bottom layer. Figure 3.12 (b) shows that the strength of the screened disorder potential in SLG is reduced by a factor 3 by the presence of the graphenic bottom layer. In addition, Fig. 3.12 shows that BLG, as a bottom layer, for $\langle n_1 \rangle \lesssim 2.5 \times 10^{12}\text{cm}^{-2}$, is more efficient than SLG to screen the top SLG layer. For $\langle n_1 \rangle \gtrsim 2.5 \times 10^{12}\text{cm}^{-2}$, SLG and BLG, as bottom layers, have the same effect on screening the disorder for the top layer given that their band structures are very similar for dopings of this order or larger.

The results of Fig. 3.12 suggest that, assuming that charge impurities are the dominant source of disorder, a very effective way to reduce the effects of disorder in SLG and BLG would be to considerably reduce the thickness of the insulating layer between the graphene sheet and the back gate. Given the modern techniques to realize graphene devices, this is something that we think could be done using the currently available experimental capabilities.
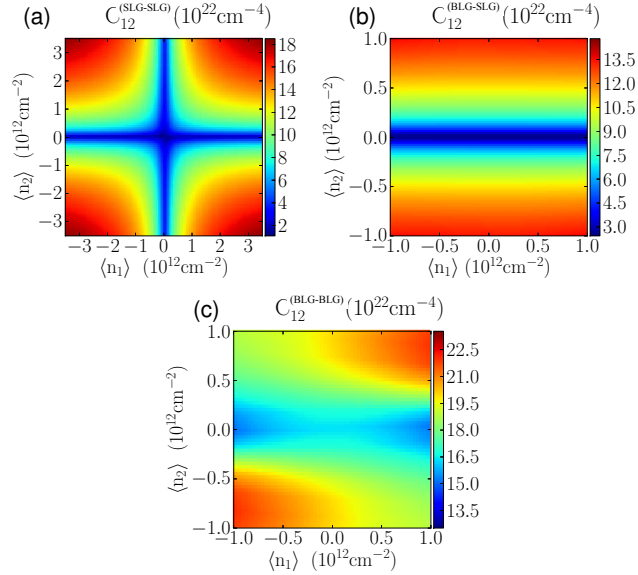
FIG. 3.13: (Color online). Color plots of the density correlation $C_{12} = \langle n_1 n_2 \rangle - \langle n_1 \rangle \langle n_2 \rangle$ as a function of the average carrier density for (a) SLG-SLG, (b) BLG-SLG and (c) BLG-BLG systems for d= 1 nm, $n_{imp} = 3 \times 10^{11} cm^{-2}$, and $d_{12} = 1$ nm.

To understand the physics of graphene heterostructures in the presence of disorder a very important property is the correlation, $C_{12} = \langle n_1(\mathbf{r}) n_2(\mathbf{r}) \rangle - \langle n_1 \rangle \langle n_2 \rangle$, between the density profiles in the two layers. The knowledge of C_{12} is important to estimate the effect of disorder on the establishment of correlated ground states. Moreover, knowledge of the nature of the correlations in the presence of disorder between $n_1(\mathbf{r})$ and $n_2(\mathbf{r})$ might be essential to understanding recent drag resistance measurements [11] on SLG-SLG heterostructures.

One possible explanation of these measurements relies on the presence of correlated electron hole puddles in the two layers [107, 108] close to the double charge neutrality point (i.e. when both $\langle n_1 \rangle$ and $\langle n_2 \rangle$ are equal to zero). Our results for C_{12}, Fig. 3.13, show that, for all three heterostructures considered, C_{12} is always positive, indicating that each electron (hole) puddle in the bottom layer corresponds an electron (hole) puddle in the top layer. This is due to the fact that the formation of

47

the electron hole puddles is mainly due to the presence of charge impurities below the bottom layer. Assuming that the energy transfer mechanism presented in Ref. [107, 108] is the main mechanism for the strong peak of the drag resistivity observed in Ref. [11] at the double charge neutrality point, our results therefore strongly suggest that in the SLG-SLG double layer structure used in Ref. [11], charge impurities below the bottom layer are the dominant source of disorder and the main reason for the formation of the electron-hole puddles at low dopings.

If the density of charge impurities between the two graphene sheets, or above the top sheet, is comparable to the density of charge impurities located below the bottom sheet the results for the correlation C_{12} would be modified. The amount of change would depend on the details of the device: ratio between the inter-sheet impurity density, the impurity density above the top layer, and the impurity density below the bottom sheet; average distance of the impurity distributions to each of the sheets; doping level in each layer,... In general, we would expect that, as the impurity density between the sheets and above the top sheet become less negligible, the carrier density fluctuations in the two sheets would become less correlated.
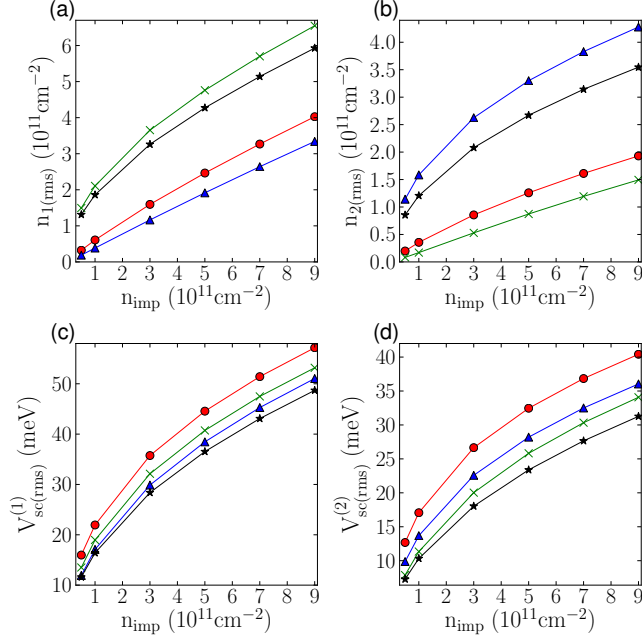
FIG. 3.14: (Color online). Plots of (a) $n_{1\,(rms)}$, (b) $n_{2\,(rms)}$, (c) $V^{(1)}_{sc\,(rms)}$, and (d) $V^{(2)}_{sc\,(rms)}$ as a function of the impurity strength n_{imp} for the SLG-SLG system, d= 1 nm, $d_{12} = 1$ nm, and for four different carrier density averages. The circle symbols correspond to $\langle n_1 \rangle = 0$ cm^{-2} and $\langle n_2 \rangle = 0$ cm^{-2}, the cross symbols to $\langle n_1 \rangle = 5 \times 10^{11}$ cm^{-2} and $\langle n_2 \rangle = 0$ cm^{-2}, the triangle symbols to $\langle n_1 \rangle = 0$ cm^{-2} and $\langle n_2 \rangle = 5 \times 10^{11}$ cm^{-2}, and the star symbols correspond to $\langle n_1 \rangle = 5 \times 10^{11}$ cm^{-2} and $\langle n_2 \rangle = 5 \times 10^{11}$ cm^{-2}.
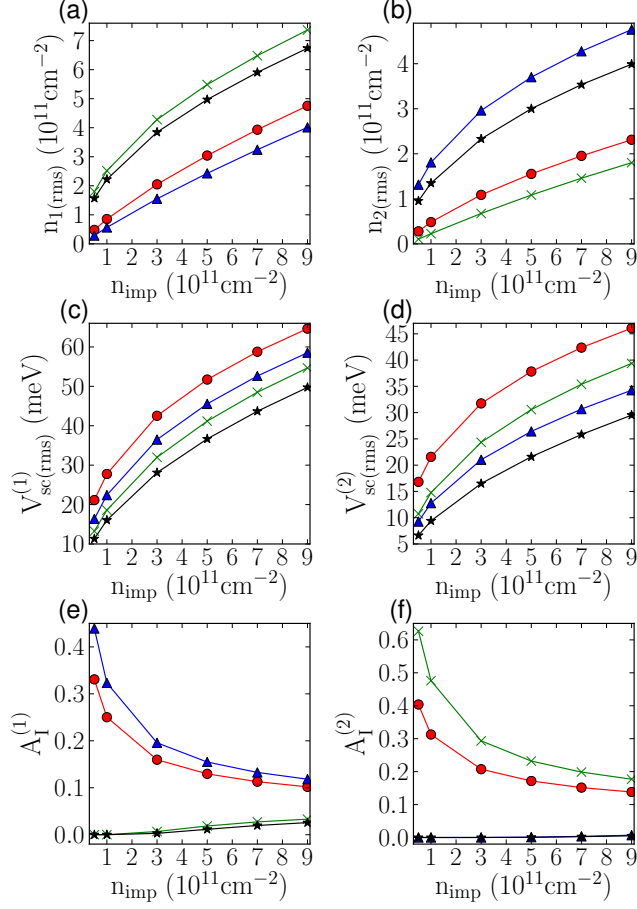
FIG. 3.15: (Color online). Plots of (a) $n_{1\,(rms)}$, (b) $n_{2\,(rms)}$, (c) $V^{(1)}_{sc\,(rms)}$, (d) $V^{(2)}_{sc\,(rms)}$, (e) fraction of the area of the sample that is insulating in layer 1, $A_I^{(1)}$, and (f) fraction of the area of the sample that is insulating in layer 2, $A_I^{(2)}$, as a function of the impurity strength n_{imp} for a SLG-SLG system with gapped graphene: $\Delta = 20$ meV, $d = 1$ nm, $d_{12} = 1$ nm, and for four different carrier density averages. The circle symbols correspond to $\langle n_1 \rangle = 0$ cm^{-2} and $\langle n_2 \rangle = 0$ cm^{-2}, the cross symbols to $\langle n_1 \rangle = 5 \times 10^{11}$ cm^{-2} and $\langle n_2 \rangle = 0$ cm^{-2}, the triangle symbols to $\langle n_1 \rangle = 0$ cm^{-2} and $\langle n_2 \rangle = 5 \times 10^{11}$ cm^{-2}, and the star symbols correspond to $\langle n_1 \rangle = 5 \times 10^{11}$ cm^{-2} and $\langle n_2 \rangle = 5 \times 10^{11}$ cm^{-2}.

FIG. 3.16: (Color online). Plots of (a) $n_{1\text{ (rms)}}$, (b) $n_{2\text{ (rms)}}$, (c) $V^{(1)}_{\text{sc (rms)}}$, (d) $V^{(2)}_{\text{sc (rms)}}$, (e) $\langle\Delta\rangle$, and (f) $\Delta_{\text{(rms)}}$ as a function of the impurity strength n_{imp} for the BLG-SLG system, d= 1 nm, $d_{12} = 1$ nm, and for four different carrier density averages. The circle symbols correspond to $\langle n_1 \rangle = 0$ cm^{-2} and $\langle n_2 \rangle = 0$ cm^{-2}, the cross symbols to $\langle n_1 \rangle = 5 \times 10^{11}$ cm^{-2} and $\langle n_2 \rangle = 0$ cm^{-2}, the triangle symbols to $\langle n_1 \rangle = 0$ cm^{-2} and $\langle n_2 \rangle = 5 \times 10^{11}$ cm^{-2}, and the star symbols correspond to $\langle n_1 \rangle = 5 \times 10^{11}$ cm^{-2} and $\langle n_2 \rangle = 5 \times 10^{11}$ cm^{-2}.

FIG. 3.17: (Color online). Plots of (a) $n_{1\,(\text{rms})}$, (b) $n_{2\,(\text{rms})}$, (c) $V^{(1)}_{\text{sc}\,(\text{rms})}$, (d) $V^{(2)}_{\text{sc}\,(\text{rms})}$, (e) $\langle\Delta^{(1)}\rangle$, (f) $\langle\Delta^{(2)}\rangle$, (g) $\Delta^{(1)}_{(\text{rms})}$, and $\Delta^{(2)}_{(\text{rms})}$ as a function of the impurity strength n_{imp} for the BLG-BLG system, d= 1 nm, $d_{12} = 1$ nm, and for four different carrier density averages. The circle symbols correspond to $\langle n_1 \rangle = 0$ cm^{-2} and $\langle n_2 \rangle = 0$ cm^{-2}, the cross symbols to $\langle n_1 \rangle = 5 \times 10^{11}$ cm^{-2} and $\langle n_2 \rangle = 0$ cm^{-2}, the triangle symbols to $\langle n_1 \rangle = 0$ cm^{-2} and $\langle n_2 \rangle = 5 \times 10^{11}$ cm^{-2}, and the star symbols correspond to $\langle n_1 \rangle = 5 \times 10^{11}$ cm^{-2} and $\langle n_2 \rangle = 5 \times 10^{11}$ cm^{-2}.

Figures 3.14-3.17 show the dependence on the impurity density of the statistical quantities characterizing the disordered the ground state, for SLG-SLG, BLG-SLG, and BLG-BLG respectively. To obtain these results we considered four different combination of average densities in the two layers: $(\langle n_1 \rangle, \langle n_2 \rangle) = (0,0); (5 \times 10^{11} \text{cm}^{-2}, 0), (0, 5 \times 10^{11} \text{cm}^{-2}, 0)(5 \times 10^{11} \text{cm}^{-2}, 5 \times 10^{11} \text{cm}^{-2})$.

For SLG-SLG, Fig. 3.14, we have that the scaling with n_{imp} is qualitatively similar for all four pairs of $(\langle n_1 \rangle, \langle n_2 \rangle)$ considered. The main feature is that, as is the case also for isolated SLG, $n_{(\text{rms})}$ is lower for $\langle n \rangle \approx 0$ than for $\langle n \rangle$ away from the charge neutrality point. When the band structure of SLG is gapped we have that the scaling $n_{(\text{rms})}$ and $V_{\text{sc (rms)}}$ with n_{imp}, Figs. 3.15 (a)-(d), is qualitatively similar to the one obtained for the gapless case. For low values of $\langle n_1 \rangle$ $(\langle n_2 \rangle)$ the fraction of the insulating area in layer 1 (2) depends quit strongly on n_{imp}, as shown in Figs. 3.15 (e), (f). In addition we see that at low doping in layer 1 (2), and low impurity densities, $A_I^{(1)}$ $(A_I^{(2)})$ depends quite strongly on $\langle n_1 \rangle$ $(\langle n_2 \rangle)$, i.e. on the doping of the other graphenic layer. For BLG-SLG heterostructures, Fig. 3.16, we find that $n_{(\text{rms})}$ and $V_{\text{sc (rms)}}$ depend very weakly on the $\langle n_1 \rangle$, consistent with the results shown in Fig. 3.10. The results of Fig. 3.16 (c) and (e) also show that the ratio between the screened disorder potential and the average band gap increases with n_{imp}. We therefore expect that the effects on the transport properties due to the presence of a band gap [114, 129, 134–136] will be stronger for cleaner samples.
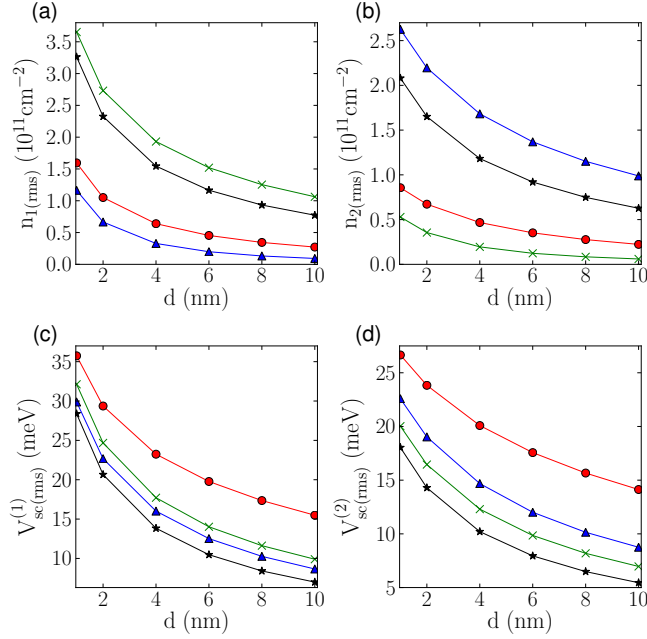
FIG. 3.18: (Color online). Plots of (a) $n_{1\ (rms)}$, (b) $n_{2\ (rms)}$, (c) $V^{(1)}_{sc\ (rms)}$, and (d) $V^{(2)}_{sc\ (rms)}$ as a function of the distance between the impurities and the lower graphenic layer d for the SLG-SLG system, $d_{12} = 1$ nm, and $n_{imp} = 3 \times 10^{11}$ cm^{-2}. The circle symbols correspond to $\langle n_1 \rangle = 0$ cm^{-2} and $\langle n_2 \rangle = 0$ cm^{-2}, the cross symbols to $\langle n_1 \rangle = 5 \times 10^{11}$ cm^{-2} and $\langle n_2 \rangle = 0$ cm^{-2}, the triangle symbols to $\langle n_1 \rangle = 0$ cm^{-2} and $\langle n_2 \rangle = 5 \times 10^{11}$ cm^{-2}, and the star symbols correspond to $\langle n_1 \rangle = 5 \times 10^{11}$ cm^{-2} and $\langle n_2 \rangle = 5 \times 10^{11}$ cm^{-2}.

Consistently with the results of Fig. 3.11 we find that for BLG-BLG systems the dependence of $n_{(rms)}$ and $V_{sc\ (rms)}$ on n_{imp} is only weakly affected by the values of $\langle n_1 \rangle$ and $\langle n_2 \rangle$, Fig. 3.17. In Fig. 3.17 (a)-(d) the dashed line shows the results obtained equations (3.16) (3.17) obtained assuming $\Delta = 0$. We see that, *for the purpose of estimating* $n_{(rms)}$ *and* $V_{sc\ (rms)}$, in BLG-BLG heterostructures neglecting the presence of a band-gap returns results that are in good agreement with the results obtained taking into account the fact that $\Delta \neq 0$. As in BLG-SLG systems we observe that also in BLG-BLG heterostructures the ratio $V_{sc\ (rms)}/\langle \Delta \rangle$ increases with n_{imp}. However, we notice that for the top BLG layer there is a large range of

values of n_{imp}, and dopings, for which $\langle \Delta \rangle$ is larger than $V_{sc\,(rms)}$ and for which we therefore expect the top layer to behave as an insulator.
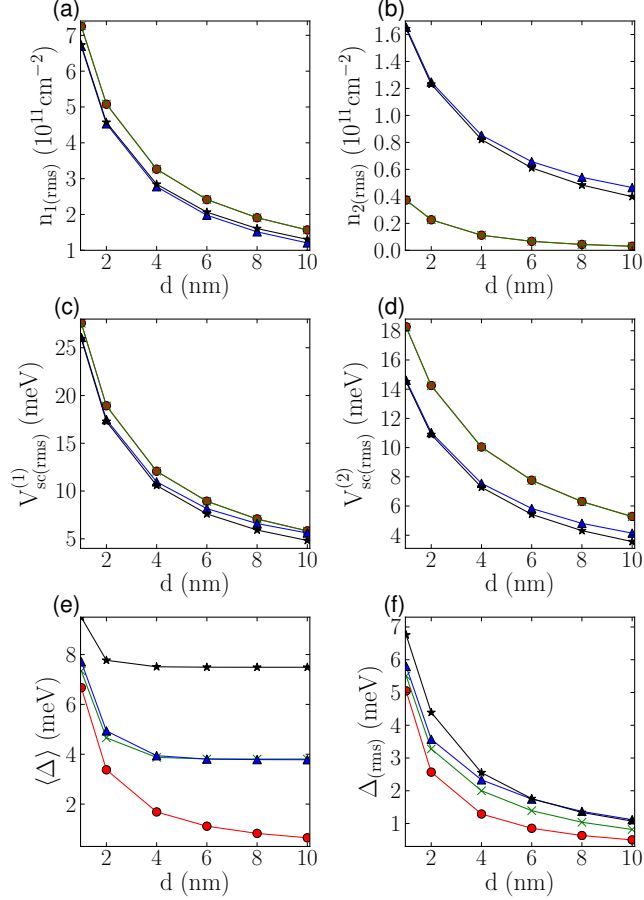
FIG. 3.19: (Color online). Plots of (a) $n_{1\,(rms)}$, (b) $n_{2\,(rms)}$, (c) $V^{(1)}_{sc\,(rms)}$, (d) $V^{(2)}_{sc\,(rms)}$, (e) $\langle \Delta \rangle$, and (f) $\Delta_{(rms)}$ as a function of d for the BLG-SLG system, $d_{12} = 1$ nm, $n_{imp} = 3 \times 10^{11}$ cm^{-2}, and for four different carrier density averages. The circle symbols correspond to $\langle n_1 \rangle = 0$ cm^{-2} and $\langle n_2 \rangle = 0$ cm^{-2}, the cross symbols to $\langle n_1 \rangle = 5 \times 10^{11}$ cm^{-2} and $\langle n_2 \rangle = 0$ cm^{-2}, the triangle symbols to $\langle n_1 \rangle = 0$ cm^{-2} and $\langle n_2 \rangle = 5 \times 10^{11}$ cm^{-2}, and the star symbols correspond to $\langle n_1 \rangle = 5 \times 10^{11}$ cm^{-2} and $\langle n_2 \rangle = 5 \times 10^{11}$ cm^{-2}.

As the distance d of the charge impurities from the bottom layer is increased, the amplitude of the carrier density inhomogeneities and of the r.m.s. of the screened disorder decrease rapidly for all the three heterostructures considered. This is shown

in Figs. 3.18-3.20. In particular, panel (d) of these figures shows that for $d \gtrsim 10$ nm, $V_{sc\ (rms)}$ in the top layer is extremely small, smaller than 5 meV for the realistic parameter considered. These results suggest that the combination of first screening layer (graphenic or metallic) and a clean buffer layer of a high quality dielectric, such as hexagonal boron nitride (hBN), 10 nm thick or more would reduce the effects of the disorder due to charge impurities to almost negligible levels.
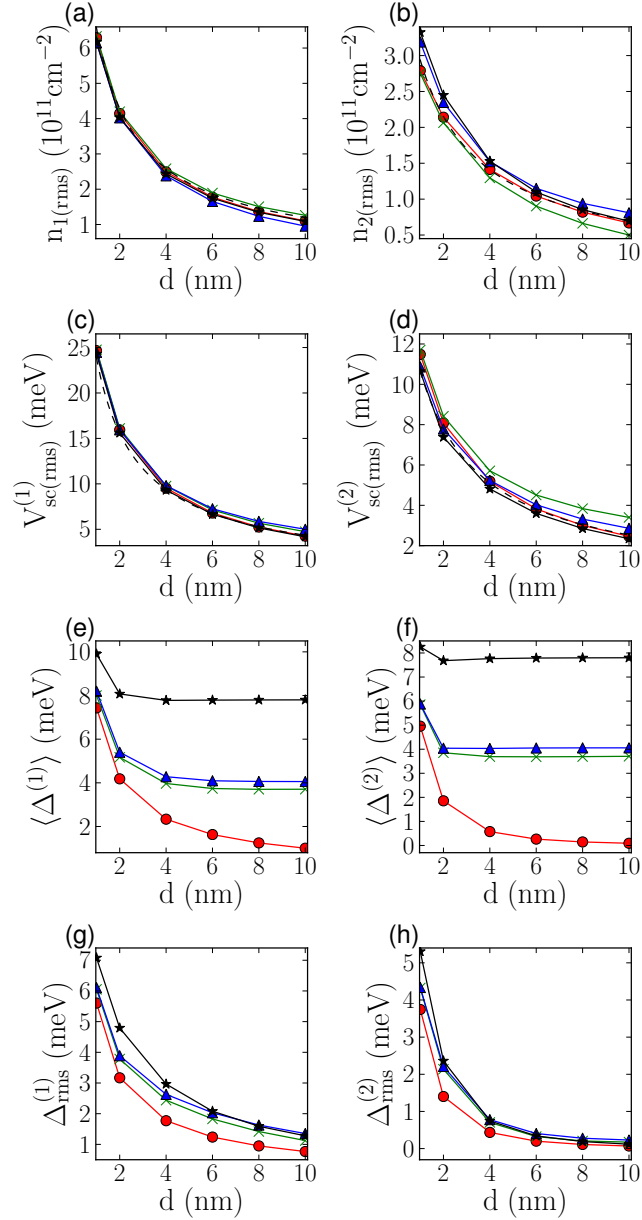
FIG. 3.20: (Color online). Plots of (a) $n_{1\ (rms)}$, (b) $n_{2\ (rms)}$, (c) $V^{(1)}_{sc\ (rms)}$, (d) $V^{(2)}_{sc\ (rms)}$, (e) $\langle\Delta^{(1)}\rangle$, (f) $\langle\Delta^{(2)}\rangle$, (g) $\Delta^{(1)}_{(rms)}$, and $\Delta^{(2)}_{(rms)}$ as a function d for the BLG-BLG system, $d_{12} = 1$ nm, $n_{imp} = 3 \times 10^{11}$ cm^{-2}, and for four different carrier density averages. The circle symbols correspond to $\langle n_1 \rangle = 0$ cm^{-2} and $\langle n_2 \rangle = 0$ cm^{-2}, the cross symbols to $\langle n_1 \rangle = 5 \times 10^{11}$ cm^{-2} and $\langle n_2 \rangle = 0$ cm^{-2}, the triangle symbols to $\langle n_1 \rangle = 0$ cm^{-2} and $\langle n_2 \rangle = 5 \times 10^{11}$ cm^{-2}, and the star symbols correspond to $\langle n_1 \rangle = 5 \times 10^{11}$ cm^{-2} and $\langle n_2 \rangle = 5 \times 10^{11}$ cm^{-2}.

For BLG-BLG systems we find that the scaling of $n_{(rms)}$ and $V_{sc\ (rms)}$ with d, analogously as for the scaling with n_{imp}, is very well approximated by equations (3.16), (3.17) derived in the limit $\Delta = 0$. Also, we find that for $d \gtrsim 3$ nm $\langle\Delta\rangle$ dependence on d is very weak, and that the ratio $\langle\Delta_{rms}\rangle/\langle\Delta\rangle$ is quite small. This is due to the fact that as d increases the disorder potential provides a decreasing contribution to the perpendicular electric field and therefore to the band-gap of BLG. For very large d and $\langle n_1\rangle$ (and/or $\langle n_2\rangle$) not zero the finite value of the band-gap is due to the almost uniform charge distributions in the graphenic layers and metal gates.
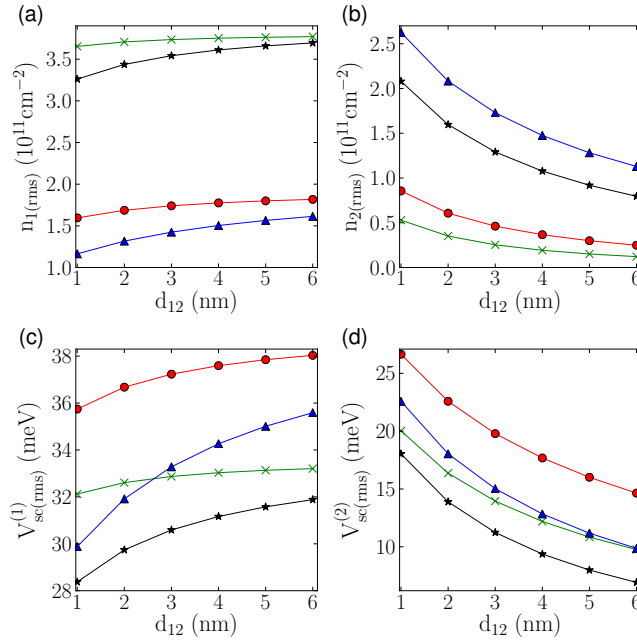
FIG. 3.21: (Color online). Plots of (a) $n_{1\ (rms)}$, (b) $n_{2\ (rms)}$, (c) $V^{(1)}_{sc\ (rms)}$, and (d) $V^{(2)}_{sc\ (rms)}$ as a function of the distance between graphenic layers d_{12} for the SLG-SLG system, $d= 1$ nm, and $n_{imp} = 3 \times 10^{11}$ cm^{-2}. The circle symbols correspond to $\langle n_1\rangle = 0$ cm^{-2} and $\langle n_2\rangle = 0$ cm^{-2}, the cross symbols to $\langle n_1\rangle = 5 \times 10^{11}$ cm^{-2} and $\langle n_2\rangle = 0$ cm^{-2}, the triangle symbols to $\langle n_1\rangle = 0$ cm^{-2} and $\langle n_2\rangle = 5 \times 10^{11}$ cm^{-2}, and the star symbols correspond to $\langle n_1\rangle = 5 \times 10^{11}$ cm^{-2} and $\langle n_2\rangle = 5 \times 10^{11}$ cm^{-2}.
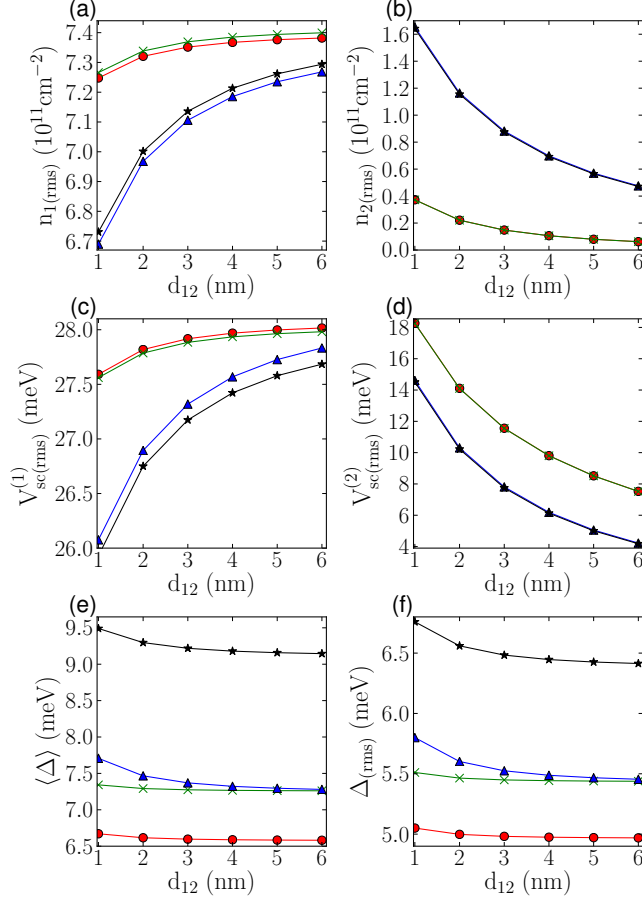
FIG. 3.22: (Color online). Plots of (a) $n_{1 \text{ (rms)}}$, (b) $n_{2 \text{ (rms)}}$, (c) $V^{(1)}_{\text{sc (rms)}}$, (d) $V^{(2)}_{\text{sc (rms)}}$, (e) $\langle \Delta \rangle$, and (f) $\Delta_{\text{(rms)}}$ as a function of d_{12} for the BLG-SLG system, d= 1 nm, $n_{\text{imp}} = 3 \times 10^{11}$ cm^{-2}, and for four different carrier density averages. The circle symbols correspond to $\langle n_1 \rangle = 0$ cm^{-2} and $\langle n_2 \rangle = 0$ cm^{-2}, the cross symbols to $\langle n_1 \rangle = 5 \times 10^{11}$ cm^{-2} and $\langle n_2 \rangle = 0$ cm^{-2}, the triangle symbols to $\langle n_1 \rangle = 0$ cm^{-2} and $\langle n_2 \rangle = 5 \times 10^{11}$ cm^{-2}, and the star symbols correspond to $\langle n_1 \rangle = 5 \times 10^{11}$ cm^{-2} and $\langle n_2 \rangle = 5 \times 10^{11}$ cm^{-2}.

Figures 3.21-3.23 show the dependence of $n_{\text{(rms)}}$, $V_{\text{sc (rms)}}$ and Δ on the distance, d_{12}, between the two layers forming the heterostructure. For the SLG-SLG heterostructure, Fig. 3.21, the scaling on d_{12} of $n_{\text{(rms)}}$ and $V_{\text{sc (rms)}}$ in layer 1 (layer 2) depends strongly on the average carrier density in layer 2 (layer 1). This is due to the fact that the ability of layer 1 (layer 2) to screen layer 2 (layer 1) from the

disorder potential depends strongly on its average carrier density. For example, when $\langle n_2 \rangle = 0$ layer 2 does not provide a significant contribution to the screening of the disorder potential in layer 1 and therefore moving it away from layer 1, i.e. increasing d_{12}, has only a very minor effect on the value of $n_{1(\text{rms})}$ and $V_{\text{sc(rms)}}^{(1)}$, as shown in Fig. 3.21 (a), (b) respectively.

For BLG-SLG heterostructures, Fig. 3.22, the dependence of $n_{(\text{rms})}$ and $V_{\text{sc (rms)}}$ on d_{12} it is almost independent of the average density in BLG, layer 1, a fact that is consistent with the other results that we have presented above for BLG-SLG systems. This reflects the fact that the density of states in BLG at low dopings depends only very weakly on the value of $\langle n \rangle$. As d_{12} increases, the values of $n_{1(\text{rms})}$ and $V_{\text{sc(rms)}}^{(1)}$ approach asymptotically the values for isolated BLG. Moreover, we observe that, as d_{12} increases, the value of $\langle \Delta \rangle$ and $\langle \Delta_{\text{rms}} \rangle$ approach a constant value, independent of d_{12}, but dependent on $\langle n_2 \rangle$, Figs. 3.22 (e), (f).
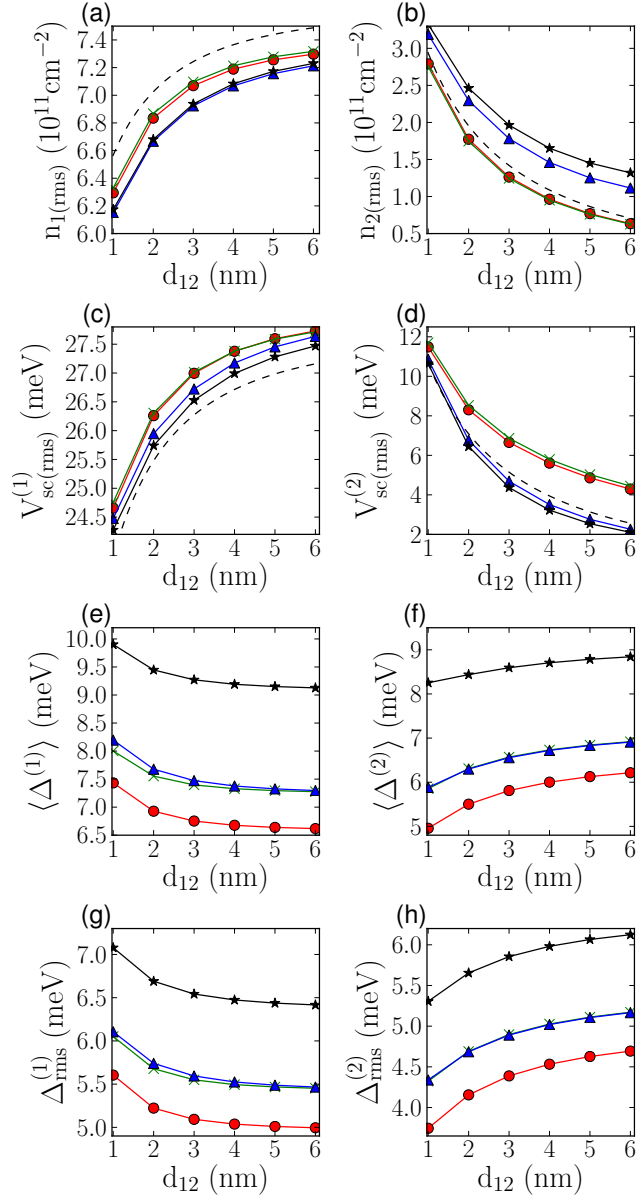
FIG. 3.23: (Color online). Plots of (a) $n_{1\,(rms)}$, (b) $n_{2\,(rms)}$, (c) $V^{(1)}_{sc\,(rms)}$, (d) $V^{(2)}_{sc\,(rms)}$, (e) $\langle \Delta^{(1)} \rangle$, (f) $\langle \Delta^{(2)} \rangle$, (g) $\Delta^{(1)}_{(rms)}$, and $\Delta^{(2)}_{(rms)}$ as a function d_{12} for the BLG-BLG system, $d= 1$ nm, $n_{imp} = 3 \times 10^{11}$ cm^{-2}, and for four different carrier density averages. The circle symbols correspond to $\langle n_1 \rangle = 0$ cm^{-2} and $\langle n_2 \rangle = 0$ cm^{-2}, the cross symbols to $\langle n_1 \rangle = 5 \times 10^{11}$ cm^{-2} and $\langle n_2 \rangle = 0$ cm^{-2}, the triangle symbols to $\langle n_1 \rangle = 0$ cm^{-2} and $\langle n_2 \rangle = 5 \times 10^{11}$ cm^{-2}, and the star symbols correspond to $\langle n_1 \rangle = 5 \times 10^{11}$ cm^{-2} and $\langle n_2 \rangle = 5 \times 10^{11}$ cm^{-2}.

61

This is due to the fact that as d_{12} increases the screening effects of the top layer on the bottom layer decrease, as mentioned above, and the perpendicular electric field reaches a value that is almost independent of d_{12}, but still dependent on $\langle n_2 \rangle$. In these conditions, Δ in layer 1 depends on layer 2 only via $\langle n_2 \rangle$. Also, as d_{12} increases, $\langle \Delta_{\text{rms}} \rangle$ in layer 1 approaches a constant value corresponding to the value of $\langle \Delta_{\text{rms}} \rangle$ for an isolated BLG sheet with average band-gap $\langle \Delta \rangle$.

The effect of a change in d_{12} in BLG-BLG systems is shown in Fig. 3.23. In figures 3.23 (a)-(d) the dashed lines show the results obtained using equations (3.16), (3.17) obtained by setting $\Delta = 0$ in both layers. We see that for the dependence of $n_{\text{(rms)}}$ and $V_{\text{sc (rms)}}$ on d_{12}, as for the dependence on n_{imp} and d, the results obtained by setting $\Delta = 0$ are in good quantitative agreement with the results obtained by calculating Δ self-consistently. For the same reason mentioned for the case of BLG-SLG heterostructure, we find that $\langle \Delta \rangle$ and $\langle \Delta_{\text{rms}} \rangle$ in the bottom layer decrease with d_{12} and approach a constant value for large d_{12}. As for BLG-SLG we see that as d_{12} increases $\langle \Delta_{\text{rms}} \rangle$ takes values that very close to the values of $\langle \Delta \rangle$.
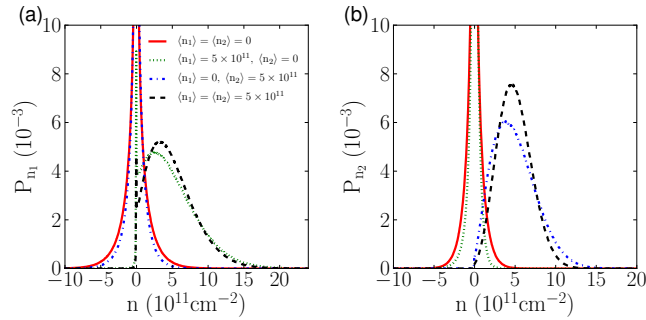
FIG. 3.24: (Color online). Plots of the carrier density probability distribution (a) P_{n_1}, and (b) P_{n_2}, for the SLG-SLG system, d= 1 nm, and $n_{\text{imp}} = 3 \times 10^{11}$ cm^{-2}. The solid line corresponds to $\langle n_1 \rangle = 0$ cm^{-2} and $\langle n_2 \rangle = 0$ cm^{-2}, the dotted line corresponds to $\langle n_1 \rangle = 5 \times 10^{11}$ cm^{-2} and $\langle n_2 \rangle = 0$ cm^{-2}, the line-dotted curve corresponds to $\langle n_1 \rangle = 0$ cm^{-2} and $\langle n_2 \rangle = 5 \times 10^{11}$ cm^{-2}, and the dashed line corresponds to $\langle n_1 \rangle = 5 \times 10^{11}$ cm^{-2} and $\langle n_2 \rangle = 5 \times 10^{11}$ cm^{-2}.
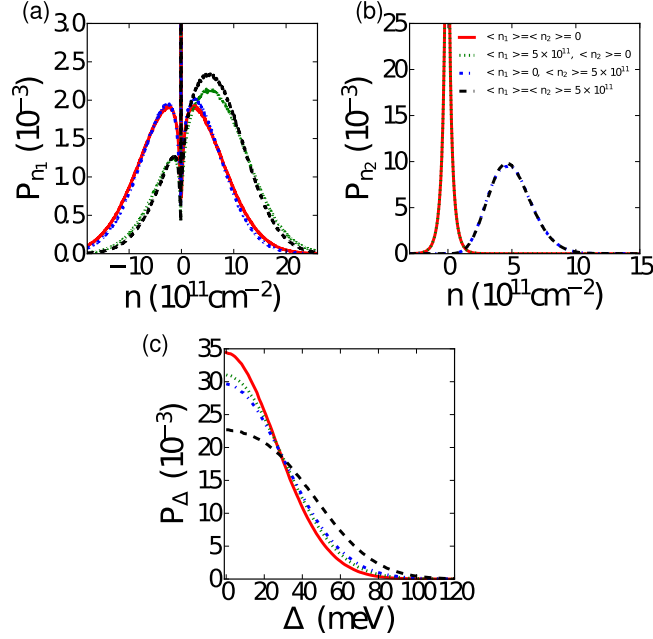
FIG. 3.25: (Color online). Plots of the carrier density probability distribution (a) P_{n_1}, and (b) P_{n_2}, and plot of the gap probability distribution (c) P_Δ for the BLG-SLG system, d= 1 nm, and $n_{imp} = 3 \times 10^{11}$ cm^{-2}. The solid line corresponds to $\langle n_1 \rangle = 0$ cm^{-2} and $\langle n_2 \rangle = 0$ cm^{-2}, the dotted line corresponds to $\langle n_1 \rangle = 5 \times 10^{11}$ cm^{-2} and $\langle n_2 \rangle = 0$ cm^{-2}, the line-dotted curve corresponds to $\langle n_1 \rangle = 0$ cm^{-2} and $\langle n_2 \rangle = 5 \times 10^{11}$ cm^{-2}, and the dashed line corresponds to $\langle n_1 \rangle = 5 \times 10^{11}$ cm^{-2} and $\langle n_2 \rangle = 5 \times 10^{11}$ cm^{-2}.

In figure 3.24 we show the probability distribution (P_{n_i}) for the carrier density in the two layers of a SLG-SLG heterostructure for different values of the average doping $\langle n_1 \rangle$ and $\langle n_2 \rangle$. For $\langle n_1 \rangle = 0$ $(\langle n_2 \rangle = 0)$ we see that P_{n_1} (P_{n_2}) is very strongly peaked around the charge neutrality point: for $n_i \to 0$ P_{n_1} reaches values that are orders of magnitude outside the scale of the figures. In this situation P_{n_i} is not Gaussian. As $\langle n_1 \rangle$ $(\langle n_2 \rangle)$ increases P_{n_1} (P_{n_2}) becomes bimodal: it exhibits a very strong and narrow peak at $n_1 = 0$ $(n_2 = 0)$ and a much broader peak around $n_1 = \langle n_1 \rangle$ $(n_2 = \langle n_2 \rangle)$. Only for quite large values of $\langle n \rangle$ P_n is well approximated by a simple Gaussian centered around $\langle n \rangle$. The properties of P_n for SLG-SLG
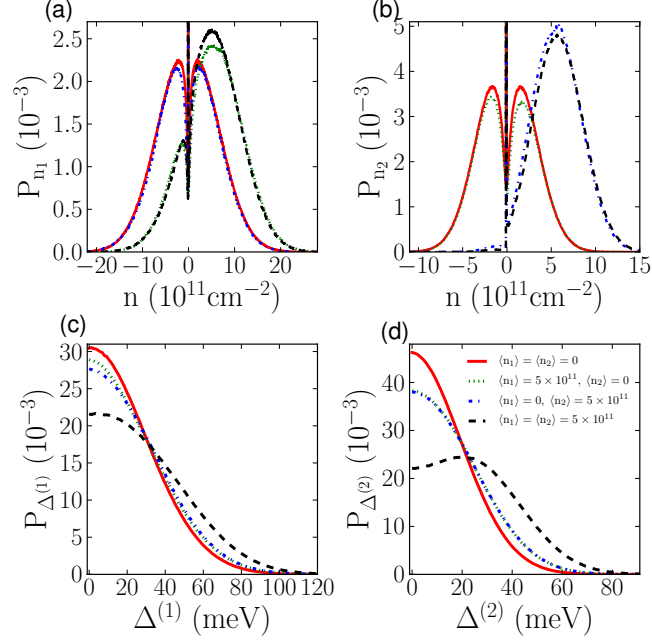
FIG. 3.26: (Color online). Plots of the carrier density probability distribution (a) P_{n_1}, and (b) P_{n_2}, and plots of the gap probability distributions (c) $P_{\Delta^{(1)}}$, and (d) $P_{\Delta^{(2)}}$ for the BLG-BLG system, d= 1 nm, and $n_{imp} = 3 \times 10^{11}$ cm^{-2}. The solid line corresponds to $\langle n_1 \rangle = 0$ cm^{-2} and $\langle n_2 \rangle = 0$ cm^{-2}, the dotted line corresponds to $\langle n_1 \rangle = 5 \times 10^{11}$ cm^{-2} and $\langle n_2 \rangle = 0$ cm^{-2}, the line-dotted curve corresponds to $\langle n_1 \rangle = 0$ cm^{-2} and $\langle n_2 \rangle = 5 \times 10^{11}$ cm^{-2}, and the dashed line corresponds to $\langle n_1 \rangle = 5 \times 10^{11}$ cm^{-2} and $\langle n_2 \rangle = 5 \times 10^{11}$ cm^{-2}.

heterostructures, and its dependence on $\langle n \rangle$, are very similar to the ones of an isolated layer of graphene [29]. The only difference is that, for the same strength of the disorder, the peaks of P_n in the second layer are narrower than in the first layer and than in an isolated graphene layer, because of the screening of the disorder by the first layer. In addition we find that because of the screening effect of the first layer, the value of $\langle n_2 \rangle$ above which P_{n_2} has a simple Gaussian peak centered around $\langle n_2 \rangle$ is lower than for the first layer (and than for isolated graphene).

Figure 3.25 (a), (b) show the results for P_{n_i} for the case of BLG-SLG. The presence of a perpendicular electric field induces the opening of a band-gap in BLG.

This causes the presence of small gapped regions with zero carrier density. As a consequence P_{n_1} exhibits an extremely narrow peak for $n_1 = 0$ surrounded by two large shoulders, Fig. 3.25 (a). As $\langle n_1 \rangle$ increases the narrow peak at $n_1 = 0$ decreases and the two-shoulders structure becomes asymmetric evolving toward a single, broad, Gaussian peak centered around $\langle n_1 \rangle$. P_n in the top layer, the SLG layer, is qualitatively very similar to the P_n of the top layer in SLG-SLG structures, just much narrower due to the fact that the BLG, as a bottom layer, is much more efficient to screen the disorder potential.

Figure 3.25 (c) shows the profile of the probability distribution (P_Δ) of the band gap in BLG. We see that P_Δ has a Gaussian-like shape, approximately centered at zero (of course limited to positive values). For the values of $\langle n_1 \rangle$ and $\langle n_2 \rangle$ considered in Fig. 3.25 (c) the profiles of P_Δ are qualitatively very similar indicating that, for the cases shown, the main contribution to Δ is due to the disorder potential. Only the profile for $\langle n_1 \rangle = \langle n_2 \rangle = 5 \times 10^{11}$ cm^{-2} shows a significant difference from the profiles for the other cases. This is due to the fact that for $\langle n_1 \rangle = \langle n_2 \rangle = 5 \times 10^{11}$ cm^{-2} a uniform Δ, independent of the disorder, is present that causes a shift of the average value of P_Δ.

Figures 3.26 (a), (b) show the results for P_{n_i} for the case of BLG-BLG. The results are qualitatively similar to the results shown in Fig. 3.25 (a) for the BLG layer of a BLG-SLG structure, and the explanation of the main qualitative features of P_n presented for that case apply also here. Figures 3.26 (c), (d) show P_Δ in the bottom and top layer respectively. In this case, for $\langle n_1 \rangle = \langle n_2 \rangle = 5 \times 10^{11}$ cm^{-2}, especially for the top layer, (black dashed line in Fig. 3.25 (d), it is clear that the average of P_Δ is shifted to the right due to the fact that when $\langle n_1 \rangle \neq 0$ and/or $\langle n_2 \rangle \neq 0$ a uniform band-gap is present.

3.5 Metal-insulator transition in double-layer graphene heterostructures

The experiments of Ref. [8] have shown that in SLG-SLG structures a density-tuned metal-insulator transition (MIT) can be induced in one of the SLG layers by tuning the doping in the other layer. The fact that the MIT in one layer is tuned by the doping in the other layer strongly suggests that long-range disorder, and in particular the electron-hole puddles that such disorder induces, play a dominant role in the physics of the MIT in SLG-SLG systems.

In Ref. [8] it was proposed that the insulating behavior of a graphene layer in a SLG-SLG heterostructure is due to strong Anderson localization made possible in the system perhaps due to strong inter-valley scattering. The "control" graphene layer provides additional screening of the disorder induced by charge impurities and therefore a reduction of the amplitude of the electron-hole puddles in the studied layer. In the scenario proposed in Ref. [8] the increase of the doping in the control layer can reduce the strength of the carrier density inhomogeneities in the studied layer, increasing the resistivity [39] to allow the manifestation of the strong Anderson localization. In Ref. [137] the tunability of localization effects in the studied layer via the doping of the control layer is attributed to the dependence of the scattering rate due to charge impurities and the dephasing time in the studied layer on the doping in the control layer.

Ref. [138] proposed a completely different scenario to interpret the results of Ref. [8]. In this scenario the dramatic increase of the resistivity, close to the CNP, in the studied layer, as a function of doping in the control layer is not due to Anderson localization, but to the fact that, as the amplitude of the disorder-induced electron-

hole puddles decreases, the resistivity at the CNP diverges since in SLG the density of states vanishes at the CNP. One of the key observations of Ref. [138] is that, contrary to metals, in systems like graphene, at low dopings, higher mobility samples exhibit higher resistivity. This agrees with the experimental results of Ref. [8] that show that of the two graphene layers forming the heterostructure, the one with the higher mobility is the one exhibiting the highest resistivity at low dopings.

We note that the contrasting interpretations offered in Ref. [8] and Ref. [138] for the experimental observations in Ref. [8] both depend crucially on the screening properties of the double-SLG system, in particular, the suppression of the impurity-induced puddles in the studied layer due to the screening induced by the control layer, as noted already in Ref. [137] using a perturbative analytical approach of double-SLG screening. Since our current work is precisely on the non-perturbative screening properties of double-layer graphene system, we are in a good position to shed light on the experimental situation studied in Ref. [8]. Our results show
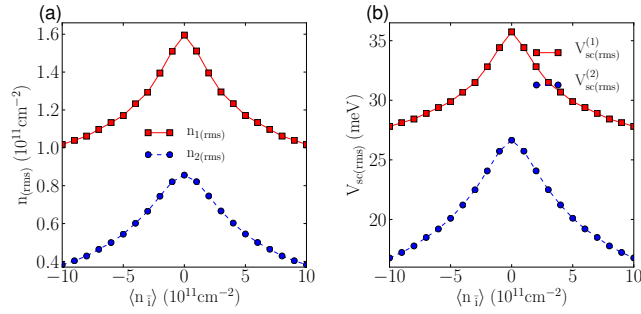
FIG. 3.27: (Color online). Plots of (a) $n_{(rms)}$ and, (b) $V_{sc\ (rms)}$ at the CNP in layer "i" as a function of the doping in the other layer $\langle n_{\bar{i}} \rangle$, for d= 1nm, $d_{12} = 1$nm, and $n_{imp} = 3 \times 10^{11}$ cm^{-2}, for the gapless SLG-SLG heterostructure. The squares correspond to the bottom SLG layer and the circles correspond to the top SLG layer.

that the two graphene layers forming the SLG-SLG heterostructure have in general very different disordered ground states. This is exemplified by Figs. 3.27 and 3.28.

Fig. 3.27 shows $n_{(rms)}$ and $V_{sc\ (rms)}$ at the CNP in layer "i" as a function of the doping in the other layer, layer $\bar{i}$. We see that the effect of the doping in the control layer is very different if the studied layer is the top (2) or the bottom (1). In other words, the screening properties of the double-SLG heterostructure are highly asymmetric, as already noted in Ref. [137] using a simple analysis, with the screening of the bottom layer by the top layer being very different quantitatively from the screening of the top layer by the bottom layer. This is due to the fact that the charge impurities are not distributed symmetrically, in particular we assumed that most of the charge impurities are closed to the surface of the SiO_2 since hBN is much cleaner than SiO_2 in terms of impurity disorder (see Fig. 3.1). The main qualitative feature that we want to emphasize is that the higher the disorder potential, $V_{sc\ (rms)}$, the higher is $n_{(rms)}$ and therefore the lower is the resistivity, in contrast to normal metals for which an increase of disorder corresponds to a resistivity increase. The results of Fig. 3.27 support the scenario presented in Ref. [138] provided our model for the gapless asymmetric double-SLG heterostructure applies to the experimental situation.

Fig. 3.28 shows $n_{(rms)}$ and $V_{sc\ (rms)}$ in the bottom (top) layer at the CNP as function of the doping in the top (bottom) layer for the case in which the graphene spectrum has a gap equal to 20 meV arising from the explicit presence of hBN substrate which might break the SLG sublattice symmetry as discussed in section II and as described by Eq. 3.2. Qualitatively the results are similar to the ones shown in Fig. 3.27: the layer with strongest disorder has the highest $n_{(rms)}$ and therefore is expected to be more metallic than the cleaner layer.

For SLG-SLG heterostructures for which the graphene spectrum has gap Δ it is interesting to consider impurity densities such that $V_{sc\ (rms)} \lesssim \Delta$. In this situation we can have ground state configurations for which the majority of the studied layer is covered by insulating regions. Under these conditions the layer is
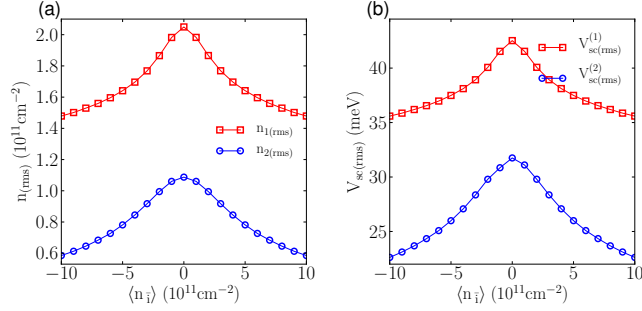
FIG. 3.28: (Color online). Plots of (a) $n_{(rms)}$ and, (b) $V_{sc\ (rms)}$ at the CN in layer "i" as a function of the doping in the other layer $\langle n_{\bar{i}} \rangle$, for d= 1nm, d_{12} = 1nm and $n_{imp} = 3 \times 10^{11}$ cm^{-2}, for the gapped SLG-SLG heterostructure. The graphene spectrum has a gap equal to 20 meV. The squares correspond to the bottom SLG layer and the circles correspond to the top SLG layer.

expected to behave as a (bad) insulator [129]. It is therefore interesting to see how the fraction of the sample, A_I, covered by insulating region in the studied layer at the CNP depends on the doping in the control layer for impurity densities such that $V_{sc\ (rms)} \sim \Delta$. This is shown in Fig. 3.29. As the doping in the control layer increases the screened disorder in the studied layer decreases, Figs. 3.29 (c), (d). As a consequence $n_{(rms)}$, i.e. the amplitude of the carrier density inhomogeneities also decreases, Figs. 3.29 (a), (b), so that in more regions of the studied layer the effective local Fermi level falls within the band-gap. We then see that, Figs. 3.29 (e), (f), as the doping in the control layer increases, A_I increases and, above a threshold, reaches 50%. For dopings in the control layer higher than this threshold value there will not be a percolating path and the studied layer is expected to exhibit an insulating behavior. The results of Fig. 3.29 therefore suggest a third plausible scenario to explain the experimental results of Ref. [8]: in the presence of a band-gap in the graphene spectrum [82, 122] the doping in the control layer, by reducing the strength of the disorder in the studied layer, can drive it into a ground state in

which more than half of the area is insulating and therefore into an insulating state. This scenario can be considered a generalization to the case when a finite band-gap is present of the scenario presented in Ref. [138]. In this scenario, where the interplay between the SLG band-gap introduced by hBN and the disorder screening by the double-SLG structure dominates transport properties in the system, there is a density-tuned an effective metal-insulator transition from a gapped insulator to an effective metal due to the percolation transition. This is akin to the situation in gapped BLG [129] where the opening of the single-particle gap has a different physical origin.

One important aspect of the results of Fig. 3.29 is that, as in the experiment, for the layer with the lower effective disorder (higher mobility), in our case the top layer, the threshold value of the doping in the control layer that drives it to be insulating is lower than for the more disordered layer (lower mobility). The values of n_{imp} and d used to obtain the results of Fig. 3.29 using the effective medium theory valid for inhomogeneous graphene ground states [111] give values of the mobility that are of the same order, 10^5 cm^2/V · s, as observed in Ref. [8]. It is therefore interesting to notice that for these values of n_{imp} we find threshold values for the doping in the control layer that are very close to the ones ($\sim 3 \times 10^{11}$cm^{-2}) observed in Ref. [8]. Thus, it appears that the presence of an SLG gap coupled with the effective screening of the disorder in the studied layer by the tuning of the density in the control layer may very well be the physics dominating the observations in Ref. [8] although more experimental work will be necessary to clarify the situation.

The main difference between our results and the results of Ref. [8] is that in [8] the top layer has a higher effective disorder, lower mobility, than the bottom layer whereas our results show that the top layer always has a lower effective disorder than the bottom layer, a consequence of the fact that we assumed the charge impurities to

be concentrated on the surface of SiO_2 , below the bottom layer. In our scenario for the MIT, this discrepancy would be resolved by assuming that in the experiment of Ref. [8] the number of charge impurities closer to the top layer is higher than in the bottom layer, perhaps due to the fabrication process or to impurities adsorbed by the open surface of the top layer. Future experimental work with better control over the spatial location and magnitude of the impurity disorder should be able to resolve this issue completely and differentiate among the three distinct interpretations (i.e. Anderson localization, intrinsic thermal transport in clean graphene near the Dirac point, and a gap-induced metal-to-insulator transition as proposed in Refs. [8], [138], and in the current work, respectively) of the experimental observations in Ref. [8].
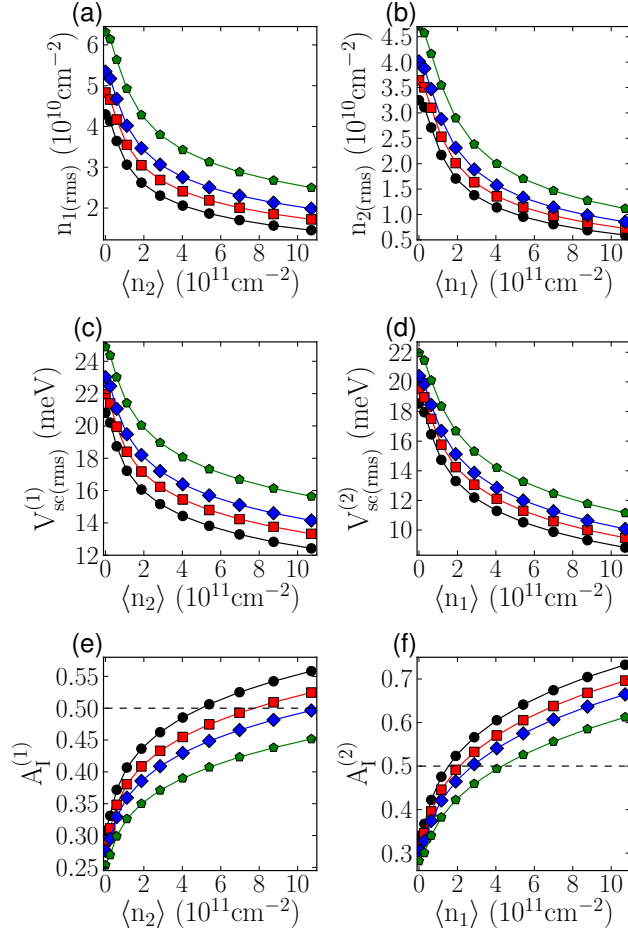
FIG. 3.29: (Color online). Plots of (a) $n_{1(\text{rms})}$, (c) $V_{\text{sc(rms)}}^{(1)}$, and (e) $A_I^{(1)}$ as a function of $\langle n_2 \rangle$, at CN in the bottom layer, and plots of (b) $n_{2(\text{rms})}$, (d) $V_{\text{sc(rms)}}^{(2)}$, and (f) $A_I^{(2)}$ as a function of $\langle n_1 \rangle$ at CN in the top layer, all for d= 5 nm, $d_{12} = 1$ nm, and for different impurity strengths. The circles correspond to $n_{\text{imp}} = 1.5 \times 10^{11}$ cm^{-2}, the squares correspond to $n_{\text{imp}} = 1.75 \times 10^{11}$ cm^{-2}, the diamonds to $n_{\text{imp}} = 2 \times 10^{11}$ cm^{-2}, and the pentagons to $n_{\text{imp}} = 2.5 \times 10^{11}$ cm^{-2},

3.6   Discussion and conclusions

In this work we have studied the effect of long-range disorder on the carrier distribution density in graphene-based heterostructures. In particular, we have considered the case in which the main source of long-range disorder are charge impu-

rities located closed to the surface of the substrate. We have considered in detail three graphene-based heterostructures: (i) SLG-SLG heterostructures formed by two sheets of single layer graphene separated by a dielectric film; (ii) BLG-SLG heterostructures formed by one sheet of bilayer graphene and one sheet of single layer graphene separated by a dielectric film; (iii) BLG-BLG heterostructures formed by two sheets of bilayer graphene separated by a dielectric film.

Our results show that, as for isolated graphenic layers, the presence of a long-range disorder potential created by charge impurities induces long-range carrier density inhomogeneities, and in particular, these inhomogeneities break up the carrier density landscape into electron-hole puddles at the charge neutrality point. However, we find that the strength of these inhomogeneities, and of the screened disorder potential, is in general much lower in the top layer due to the screening of the disorder by the bottom layer, the one closer to the charge impurities. This is expected, but our results are the first to quantify such an effect for a large range of experimentally relevant conditions. In particular, our results show that in BLG-SLG heterostructures the strength of the screened disorder in the SLG sheet is much lower than in the top SLG sheet of a SLG-SLG heterostructure. This is due to the fact that at low energies, for most experimentally relevant conditions, BLG has a higher density of states than SLG and therefore is much more efficient in screening the top layer from the disorder. This also suggests that a very effective way to reduce the effect of charge impurities in SLG, or BLG, would be to reduce the thickness of the dielectric between the graphenic layer and the metallic back gate.

One difficulty to obtain an accurate characterization, in the presence of charge impurities, of the carrier density profile of heterostructures comprising BLG is the fact that the impurities, and the carriers in the nearby graphenic layers and metal gates, create an electric field with a component perpendicular to BLG that induces

the opening of band-gap (Δ) in BLG. As a consequence, for heterostructures in which BLG is present, the carrier density profiles and the BLG band-gap have to be calculated self-consistently. Our results show that in general the average band gap Δ is not negligible. For the set of parameters that we have used we find that the local value of Δ can be of the order of 50 meV, the average $\langle\Delta\rangle$ is of the order of 10-15 meV, and that for most of the cases the root mean square of Δ, $\langle\Delta_{\mathrm{rms}}\rangle$, is of the order of $\langle\Delta\rangle$, indicating that the inhomogeneities in the profile of $\Delta(\mathbf{r})$ are very strong. We expect these results to be very important to interpret transport measurements in BLG-based heterostructures.

We have also calculated the correlation (C_{12}) between the density profile in the bottom layer and the one in the top layer. We find that for all the heterostructures and conditions considered the two inhomogeneous density profiles are correlated, meaning that C_{12} is positive and different from zero. This is due to the fact that we assumed that the dominant source of long-range disorder are charge impurities placed close to the bottom layer of the heterostructure. Our results are important because provide a critical element for the interpration of the recent results on the drag resistivity in SLG-SLG heterostructures [11, 107, 108].

Our results are also directly relevant to the recently observed metal insulator transition in graphene layers forming a SLG-SLG heterostructure. In particular our results show that the transition from metallic to insulating in the studied graphene layer of the SLG-SLG heterostructure, as a function of the doping in the control layer, can be explained as a percolation-like transition driven by the reduction of the amplitude and size of the electron-hole puddles induced by the additional screening of the impurity charges in the control layer of the disorder potential.

In particular, we show that the possible presence of an SLG gap, caused by the hBN substrate, could easily lead to the observed metal-insulator transition in the

system as the charged disorder in the studied layer in suppressed due to screening induced by the control layer through density tuning.

The results presented are directly relevant to imaging experiments, like scanning tunneling microscopy experiments, and for the interpretion of transport measurements. In particular, the results for systems formed by BLG, by providing both the strength of the band-gap induced by the perpendicular electric field generated self-consistently by the distribution of charges in the heterostructure, and the strength of the screened disorder potential, allow to identify the parameter regimes where the BLG sheet is expected to behave as a bad metal or as a bad insulator [129]. Our results are also important to better understand the conditions necessary for the establishment of collective ground states that have been theoretically predicted for SLG-SLG [94, 139], BLG-SLG [98], and BLG-BLG [133] heterostructures.

3.7 Competing orders in bilayer graphene

Bilayer graphene (BLG) is obtained by stacking two graphene layers on top of each other. Among all the possible stacking configurations, the AB stacking (also known as Bernal stacking) is the most energetically favorable, where one of the layers is rotated 60 degrees relative to the other. In this situation, the original SLG linear bands change into quadratic bands which touch at the corners of the Brillouin zone [40]. In contrast with SLG where the density of states (DOS) vanishes at the linear band crossing point, the BLG DOS is constant at charge neutrality, enhancing the possibility for electron-electron interactions to drive phase transitions.

In general, electron-electron interactions can lead to two possible broken symmetry ground state families whose members differ in spin and valley structures. The first family corresponds to gapped phases. In this work, we will focus on the pseudospin ferromagnet phase. The second family is referred to as nematic. In this phase, the interactions lead to the splitting of the quadratic band crossing point into two linear band crossing points and is characterized by the breaking of the continuous rotational symmetry in momentum space.

Several experiments have been performed to try to determine the nature of the ground state in BLG at low energies [15–23]. In Ref. [15] Landau level spectroscopy (LLS) revealed the existence of a gapped state with a gap $\Delta \sim 0.1$ meV, which is larger than the gap expected from Zeeman splitting. In Ref. [18], measurements of the density of states at the Fermi level combined with conductivity measurements, points to a nematic transition which was confirmed by LLS with an order parameter $\Delta \sim 6$ meV. It is worth noting that among all the experiments here mentioned, this one uses the cleanest sample. In Ref. [19] conductivity measurements at charge neutrality indicate the existence of a gap in the spectrum. Although these experiments

predict different phases, they agree on the fact that an interaction-driven broken symmetry ground state is present.

Method. Figure (3.30) shows a sketch of the system, where BLG is located in the vicinity of charged impurities. The low-energy mean-field Hamiltonian for BLG
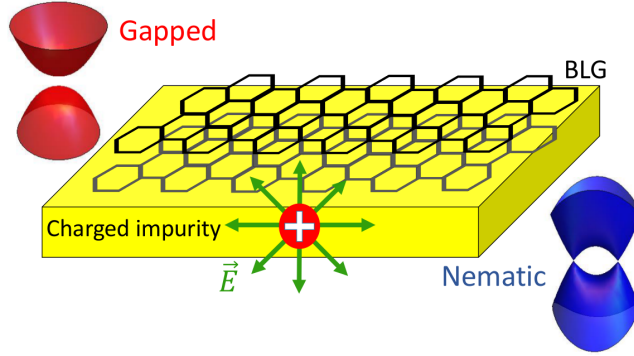
FIG. 3.30: Schematic of bilayer graphene in the presence of random charged impurities.

in a broken symmetry state, for a single spin species, around the K point, in the clean limit, can be written as $\hat{H} = \hat{H}_0 + \hat{\Delta}$, where

$$
\hat{H}_0 = \begin{bmatrix} 0 & \frac{\hbar^2 k^2}{2m^*} e^{-2i\theta_{\mathbf{k}}} \\ \frac{\hbar^2 k^2}{2m^*} e^{2i\theta_{\mathbf{k}}} & 0 \end{bmatrix} , \tag{3.20}
$$

$\theta_{\mathbf{k}} = \arctan(k_y/k_x)$, $\hat{\Delta} = \Delta_{\mathrm{g}}\sigma_z$ for the gapped state, and $\hat{\Delta} = \Delta_{\mathrm{n}}\sigma_x$ for the nematic state, where the Pauli matrices σ_j act in the pseudospin space. The self-consistent equations for the nematic and gapped phase order parameters, assuming short-range exchange interactions, are given by

$$
\Delta_{\mathrm{n}} = \frac{e^2 \mathrm{V}_{\mathrm{n}}}{2(2\pi)^2 \epsilon} \int d\mathbf{k} \left[f_{\mathrm{n},\mathbf{k}}^{(-)} - f_{\mathrm{n},\mathbf{k}}^{(+)} \right] \frac{\Delta_{\mathrm{n}} + \frac{\hbar^2}{2m^*} k^2 \cos 2\theta_{\mathbf{k}}}{E_{\mathbf{k}}^{(\mathrm{n})}} , \tag{3.21}
$$

$$\Delta_{\mathrm{g}} = \frac{e^2 V_{\mathrm{g}}}{2(2\pi)^2 \epsilon} \int d\mathbf{k} \left[f_{\mathrm{g},\mathbf{k}}^{(-)} - f_{\mathrm{g},\mathbf{k}}^{(+)} \right] \frac{\Delta_{\mathrm{g}}}{E_{\mathbf{k}}^{(\mathrm{g})}} , \qquad (3.22)$$

where V_{g} (V_{n}) is the strength of the intralayer (interlayer) short range Coulomb interaction. The carrier density dependent Fermi functions are given by $f_{i,\mathbf{k}}^{(\pm)} = (1 + e^{(\pm E_{\mathbf{k}}^{(i)} - \mu_L^{(i)})/k_B T})^{-1}$, where $i =$ n,g. The energy for states in the nematic phases is $E_{\mathbf{k}}^{(\mathrm{n})} = \sqrt{(\xi_{\mathbf{k}} + \Delta_{\mathrm{n}})(\xi_{\mathbf{k}}^* + \Delta_{\mathrm{n}})}$, and in the gapped phase is $E_{\mathbf{k}}^{(\mathrm{g})} = \sqrt{\Delta_{\mathrm{g}}^2 + |\xi_{\mathbf{k}}|^2}$, where $\xi_{\mathbf{k}} = \frac{\hbar^2 |\mathbf{k}|^2}{2m^*} e^{-2i\theta_{\mathbf{k}}}$, and $\mu_L^{(i)} = \mu_L^{(i)}(n)$ corresponds to the local chemical potential.
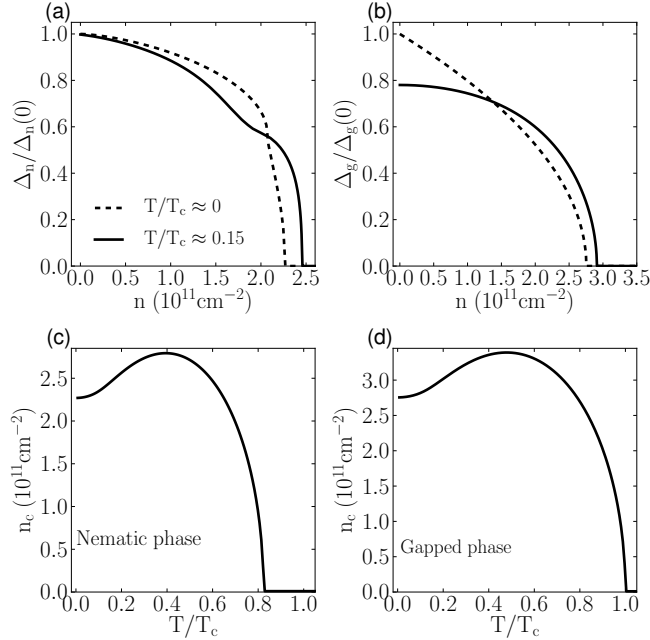
FIG. 3.31: (a) ((b)) Plot of the nematic (gapped) phase order parameter Δ_{n} (Δ_{g}) for $T/T_c = 0$ (dashed line), and $T/T_c > 0$ (solid line). Panels (c) and (d) show plots of the critical density n_c as a function of the temperature for the nematic and the gapped phases, respectively.

Figs. (3.31a) and (3.31b) show the order parameters Δ_{n} and Δ_{g} as a function of the carrier density n normalized to the order parameter strength at charge neutrality (CN). We assume that at CN both phases have the same strength, this is $\Delta_{\mathrm{n}}(n = 0) = \Delta_{\mathrm{g}}(n = 0)$. The dashed lines correspond to the order parameter at zero

temperature while the solid lines correspond to the order parameter for $T/T_c \sim 0.15$, where the critical temperature T_c was chosen to be the critical temperature for the gapped phase. The nematic phase at zero temperature has a critical carrier density $n_c \approx 2.5 \times 10^{11}\text{cm}^{-2}$, while the gapped phase presents a slightly larger value $n_c \approx 2.7 \times 10^{11}\text{cm}^{-2}$. The finite temperature result shows that thermal fluctuations have a larger impact in the gapped phase than o the nematic phase. In fact, close to CN, the results suggest that the nematic phase is not suppressed. Also, we observe an increase in the critical density n_c at finite temperature. In this regime, thermal fluctuations assist electron-electron pairing due to the particle-hole asymmetry away from the charge neutrality point. Larger values of T/T_c will eventually destroy the pairing as can be seen in Figs. (3.31c) and (3.31d). In order to characterize the ground state in the presence of long-range disorder we use the Thomas-Fermi-Dirac (TFD) theory as has been explained in detail in previous sections. The TFD energy functional in this situation is given by

$$E^{(i)}[\text{n}(\mathbf{r})] = E_{\text{K}}^{(i)}[\text{n}(\mathbf{r}), \Delta_i] + \frac{e^2}{2\epsilon} \int d^2\mathbf{r}d^2\mathbf{r}' \frac{\text{n}(\mathbf{r})\text{n}(\mathbf{r}')}{|\mathbf{r} - \mathbf{r}'|} + \frac{e^2}{\epsilon} \int d^2\mathbf{r}V_{\text{D}}(\mathbf{r})\text{n}(\mathbf{r}) - \mu_{\text{g}} \int d^2\mathbf{r}\text{n}(\mathbf{r}) \,,$$

$$(3.23)$$

where $i =$ g,n for the gapped and nematic phases, ϵ is the medium dielectric constant, and e is the electron electric charge. The disorder potential is given by

$$V_{\text{D}}(\mathbf{r}) = \int d\mathbf{r}' \frac{c(\mathbf{r}')}{[|\mathbf{r} - \mathbf{r}'|^2 + d^2]^{1/2}} \qquad (3.24)$$

where $c(\mathbf{r})$ is a random, two-dimensional distribution of charge impurities located an effective distance d from BLG such that $\langle c(\mathbf{r}) \rangle = 0$ and $\langle c(\mathbf{r})^2 \rangle = n_{\text{imp}}$. The first term in Eq. (3.23) includes the kinetic energy and the exchange part of the Coulomb

interaction, the second term is the Hartree part of the Coulomb interaction, while the third term accounts for the contribution from disorder. The ground state of the carrier density is found by requiring that the variation of the energy functional with respect to the carrier density vanishes, $\delta E_i[n]/\delta n = 0$. This requirement leads the relation

$$\frac{\delta}{\delta \text{n}} E_{\text{K}}^{(i)}[\text{n}(\mathbf{r}), \Delta_i] + \frac{e^2}{2\epsilon} \int d^2\mathbf{r}' \frac{\text{n}(\mathbf{r}')}{|\mathbf{r} - \mathbf{r}'|} + \frac{e^2}{\epsilon} V_{\text{D}}(\mathbf{r}) - \frac{2\text{m}^*\mu_{\text{g}}}{\hbar^2} = 0 \,, \qquad (3.25)$$

where the variation of the kinetic term for the gapped phase is

$$\frac{\delta}{\delta \text{n}} E_{\text{K}}^{(g)}[\text{n}(\mathbf{r}), \Delta_g] = \sqrt{(\pi \text{n})^2 + \Delta_{\text{g}}^2} \,, \qquad (3.26)$$

and the corresponding term for the nematic phase, $\frac{\delta}{\delta \text{n}} E_{\text{K}}^{(n)}[\text{n}(\mathbf{r}), \Delta_n] \equiv \nu^n$, is defined implicitly by the relation

$$\text{n} = \frac{2m^*\nu^n}{2\pi^2\hbar^2} \mathcal{I}\left(\frac{\Delta_{\text{n}}}{\nu^n}\right) \,, \qquad (3.27)$$

where

$$\mathcal{I}(x) = \int_0^{2\pi} d\phi f(x, \phi) \,, \qquad (3.28)$$

$$f(x, \phi) = \begin{cases} \sqrt{1 - x\sin^2(2\phi)} & , 1 - x\sin^2(2\phi) > 0 \\ 0 & , 1 - x\sin^2(2\phi) \leq 0 \,. \end{cases}$$

We solve Eqs. (3.21), (3.22), and (3.25) for the carrier density $\text{n} = \text{n}(\Delta_{\text{i}})$ and the order parameter $\Delta_i = \Delta_i(\text{n})$ self-consistently. Notice that if the system is not in a broken symmetry state, we can solve (3.25) analytically [129]. In the ordered phases however, the presence of the order parameters introduces non-linearities in Eq. (3.25), and no analytic solution is available. The problem is then solved numerically for 100×100 nm BLG samples and a single realization.

Fig. (3.32) show maps for the carrier density and the local order parameter. (a) shows a map of the carrier density for BLG in the gapped phase. We observe that we obtain regions where the carrier density vanishes, shown in white. In (b) it is shown that the insulating regions correspond to regions where the gapped phase order parameter reaches its maximum value. Also, regions where the carrier density presents large fluctuations (blue corresponds to holes, and red to electrons) are out of the ordered phase (black regions in the order parameter map). In contrast, the carrier density map for the nematic phase in (c) shows no insulating regions. However, the map for the order parameter Δ_n in (d) shows finite values corresponding to regions where the carrier density fluctuations are smaller than the critical density $n_c \approx 2.4 \times 10^{11} \text{cm}^{-2}$.
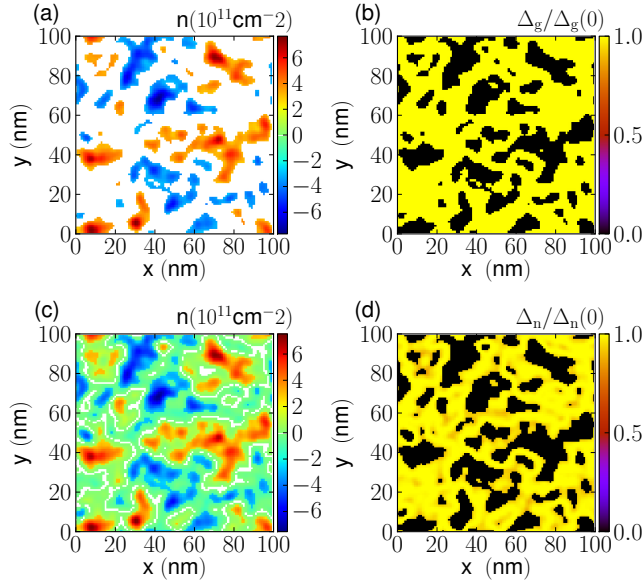
FIG. 3.32: Panels (a), and (b) show color plots of the carrier density n(**r**), and the gapped phase order parameter $\Delta_g/\Delta_g(0)$. Panels (c), (d) show color plots of n(**r**) and the nematic phase order parameter $\Delta_n/\Delta_n(0)$. This maps are at CN, for d= 3nm, impurity density $n_{imp} = 1 \times 10^{11}$, and $T/T_c = 0$. White areas in (a) represent insulating regions.

Now we consider disorder averaged results obtained using 160×160 nm BLG samples. In Fig. (3.33) we show the zero-temperature probability distribution for the carrier density n and the order parameters in the gapped (solid lines) and nematic (dashed lines) phases for $d = 3$ nm, and $n_{imp} = 10^{11} cm^{-2}$. The main difference between the distributions is observed around CN, where the gapped phase has zero carrier density probability, while the nematic phase has a finite carrier density probability. This result is directly connected to transport measurements. The order-parameter-probability distributions are approximate bi-modal for both the nematic and gapped phases, where either Δ_n and Δ_g vanish, or they take their maximum value.
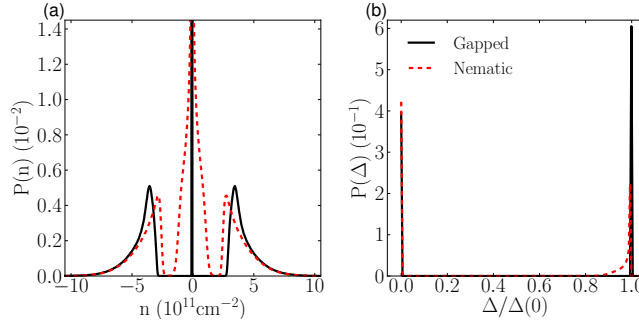
FIG. 3.33: Plots of (a) the carrier density probability distribution P(n), and (b) the order parameter probability distributions P(Δ) for the gapped (solid line) and nematic phases (dashed line) at the CNP, for d= 3nm, $n_{imp} = 1 \times 10^{11}$ cm^{-2}, and $T/T_c = 0$.

In order to determine whether a particular sample is in an ordered phase or not, let us define the fraction area A_i, corresponding to the area of the sample that is in the ordered phase. If $A_i > 0.5$ we say that the sample is in an ordered phase. Figs. (3.34a) and (3.34c) show the fraction area A_i, as a function of temperature T/T_c and the impurity density n_{imp}. The black solid lines indicates the contour $A_i = 0.5$, which corresponds to the boundary separating an ordered sample, from a disordered

one. Panels (3.34b) and (3.34d) show the disorder-averaged order parameter as a function of T/T_c and n_{imp} for the nematic and gapped phases respectively. In order
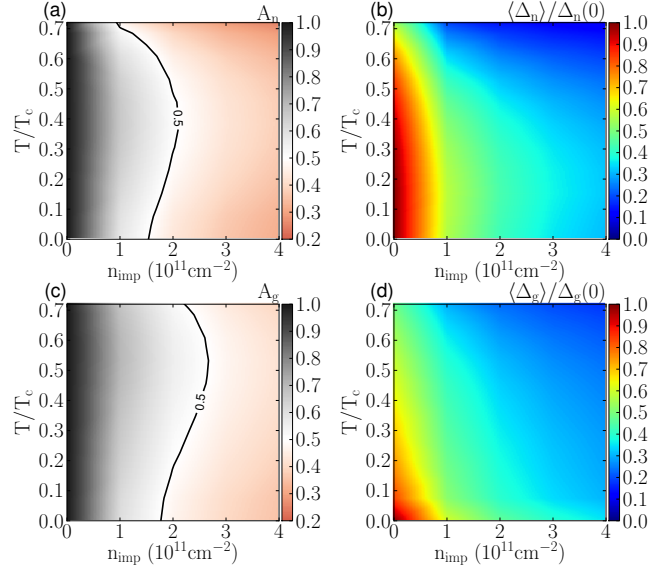
FIG. 3.34: Panels (a) and (c) show plots of the fraction area A_i as a function of T/T_c and n_{imp}. Panels (b) and (d) show plots of the average nematic and gapped order parameters $\langle \Delta_i \rangle / \Delta(0)_i$. T_c corresponds to the critical temperature for the gapped phase.

to directly compare the effect of the disorder and temperature in both phases, in Fig. (3.35a) we plot the ratio of the order parameters $\langle \Delta_n \rangle / \langle \Delta_g \rangle$, as a function of the impurity density n_{imp} for three different temperatures. The purple squares correspond to zero temperature.

For all the values of the disorder impurity considered Δ_g is larger than Δ_n. The green circles correspond to $T/T_c = 0.15$, the nematic phase present a larger order parameter than the gapped phase. Finally, the black triangles correspond to $T/T_c = 0.53$. At this temperature, a crossover is observed as a function of the impurity density. The dashed line is a reference that indicates when the ratio becomes one. Figure (3.35 b) presents the full T/T_c-n_{imp} phase-diagram. Green

regions correspond to regions where the nematic phase is larger than the gapped phase. In the purple regions the gapped phase is larger. In the range of impurity strengths and temperatures considered we observe two boundaries separating the phases.
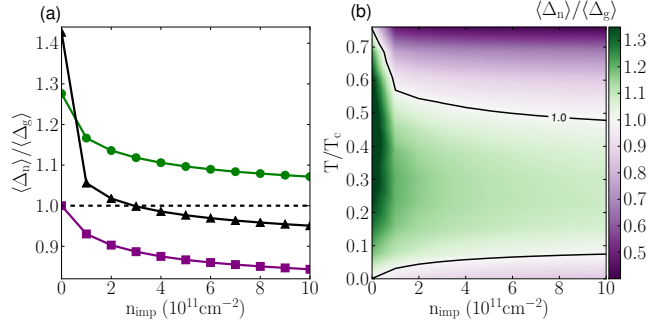
FIG. 3.35: (a) Plots of $\langle \Delta_n \rangle / \langle \Delta_g \rangle$ at CNP as a function of n_{imp} for d= 3nm, and three values of T/T_c. The squares correspond to $T/T_c = 0$, the circles to $T/T_c = 0.15$, and the triangles to $T/T_c = 0.53$. (b) Temperature-n_{imp} phase diagram. The black lines indicate the boundary between the phases.

Conclusions and Outlook. In conclusion, we have studied the effect of long-range disorder on the broken symmetry ground states in BLG. We determined self-consistently the local order parameter, and the carrier density for the gapped and nematic phases and we obtained a disorder-temperature phase diagram. We found that low temperatures favor the gapped phase for all the impurity densities considered while in the range $0.1 \lesssim T/T_c \lesssim 0.6$ the nematic phase presents a larger order parameter strength compared with the gapped phase.

It is important to notice that in the work presented in this section we have ignored two effects that are important in the determination of the ground state. Both of these effects are related to the presence of a random electric field generated by the charged impurities. The first effect corresponds to the breaking of the layer (pseudospin) symmetry that induces the opening of a band gap in the BLG energy

spectrum. This additional gap adds to the interaction-induced gap and must be taken into account in order to correctly determine the self-consistent ground state. The second effect that we are not considering is the order parameter phase coherence.

Because of this, further work to find the nature of the broken symmetry ground state in BLG in the presence of long-range disorder induced by charged impurities is required.

3.8 Local, Global and Nonlinear Screening in Twisted Double Layer Graphene

In this section, we discuss some experimental results regarding the characterization of the screening properties of double-layer graphene heterostructures performed by Chihpin Liu *et.al.* in Ref. [13]. The goal of this experiments is the characterization of the potential fluctuations in SLG-SLG heterostructures and the comparison with the potential fluctuations on SLG. To this end, scanning tunneling microscopy (STM), spectroscopy (STS), Landau-level (LL) spectroscopy, and numerical simulations are used.

It is experimentally demonstrated that the presence of a layer of graphene in between the insulating substrate and the 2D system under study (which in our case is also graphene) reduces the interference of the substrate with the sample, while preserving the electronic properties of the original system, provided there is a large twist angle between the layer to prevent hybridization. The role of the graphene layer is to screen the random potential fluctuations induced by charged impurities located in the substrate. In Fig. (3.36) we show the experimental setup, where a graphene layer is placed on top of SiO_2 , with another graphene layer directly on top of it. The sample then has two distinct regions. The distance between the layers in the z-directions is measured to be $d_{12} = 0.7$ nm.

Measurements of the dI/dV spectra, related to the sample density of states, as a function of the bias voltage (V_b) for different gate voltages (V_g) (charge carrier density) allow to locate the position of the Dirac point as a function of V_g. The relation between the Dirac point energy, and V_g is given by [36]

$$E_D = \hbar v_F \sqrt{\frac{1}{2}\pi\alpha|V_g - V_0|} \, , \tag{3.29}$$

86
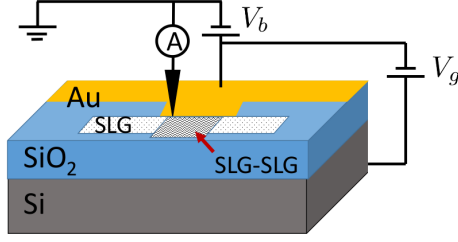
FIG. 3.36: Sketch of the setup for STM measurements.

where $\alpha = 7 \times 10^{10} \text{cm}^{-2} V^{-1}$ is the charging capacitance per layer. Then, a fit of the data to Eq. (3.29) allows us to obtain the Fermi velocity $v_F = (1.02 \pm 0.04) \times 10^6$ m/s. The shift $V_0 = 22.5 \pm$ V corresponds to an unintentional hole doping of $\langle n \rangle = 8 \times 10^{11} \text{cm}^{-2}$. Experimental maps of the spectra dI/dV for SLG and SLG-SLG reveal the electron-hole puddles induced by charge impurities [13], as it has been reported previously [99]. Figs. (3.37a), and Fig. (3.37b) show numerical simulations of the Fermi energy fluctuations for SLG, and SLG-SLG respectively. In the simulation we used an impurity density $n_{imp} = 5 \times 10^{11} \text{cm}^{-2}$, average carrier density $\langle n \rangle = 10^{12} \text{cm}^{-2}$ per layer corresponding to the measured unintentional doping, average distance to the impurities $d = 1.5$ nm, and interlayer separation $d_{12} = 0.7$ nm as measured. In the experimental observations and the numerical simulations we find a reduction of the potential fluctuations upon the inclusion of a second graphene layer.

To better understand the screening properties, we consider disorder averaged results in the numerical simulations. Fig. (3.38a) shows the screened disorder potential fluctuations for SLG and SLG-SLG as a function of the average distance to the charge impurities. The black, dashed straight line corresponds to the SLG-SLG system for $d = 1.5$ nm, $d_{12} = 0.7$ nm, and $\langle n \rangle = 10^{12} \text{cm}^{-2}$. The blue circles corre-
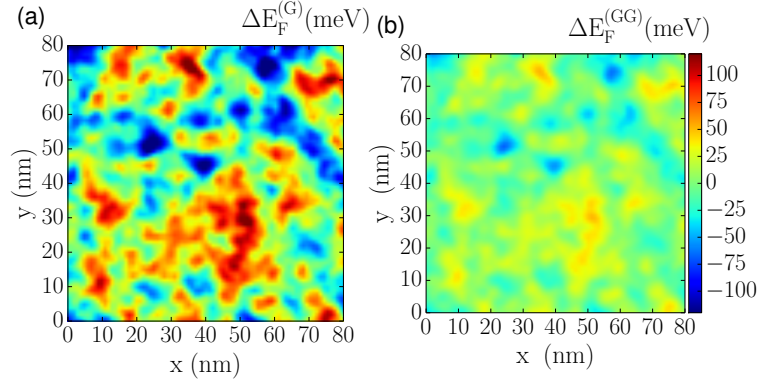
FIG. 3.37: Simulated map for SLG, and SLG-SLG obtained with a single disorder realization assuming $n_{imp} = 5 \times 10^{11} \text{cm}^{-2}$, carrier density $\langle n \rangle = 10^{12} \text{cm}^{-2}$, average distance to the impurities $d = 1.5$ nm, and interlayer separation $d_{12} = 0.7$ nm.

spond to SLG with $\langle n \rangle = 10^{12} \text{cm}^{-2}$, and the red squares corresponds to SLG with $\langle n \rangle = 2 \times 10^{12} \text{cm}^{-2}$. For comparison, we also show the potential fluctuations for bilayer graphene (BLG). In the presence of an electric field, a gap develops in the BLG energy spectrum due to layer symmetry breaking. The green solid line corresponds to the analytic result obtained when the effect of the random electric field generated by the charged impurities is ignored. The empty triangles correspond to the case where the gap generation is taken into account self-consistently. In order to obtain with SLG the same suppression of the potential fluctuations achieved with SLG-SLG, we need to double the carrier density and increase the average separation with the charged impurities. Fig. (3.38b) shows the potential fluctuations at charge neutrality. Note that for low doping, the fluctuations in BLG are independent of the carrier density. Figs. (3.38c) and (3.38d) show the carrier density fluctuations for cases (a), and (b) respectively. Note that even at charge neutrality, for $d < 1.4$ nm in SLG-SLG the graphene buffer reduces better the potential fluctuations than BLG.
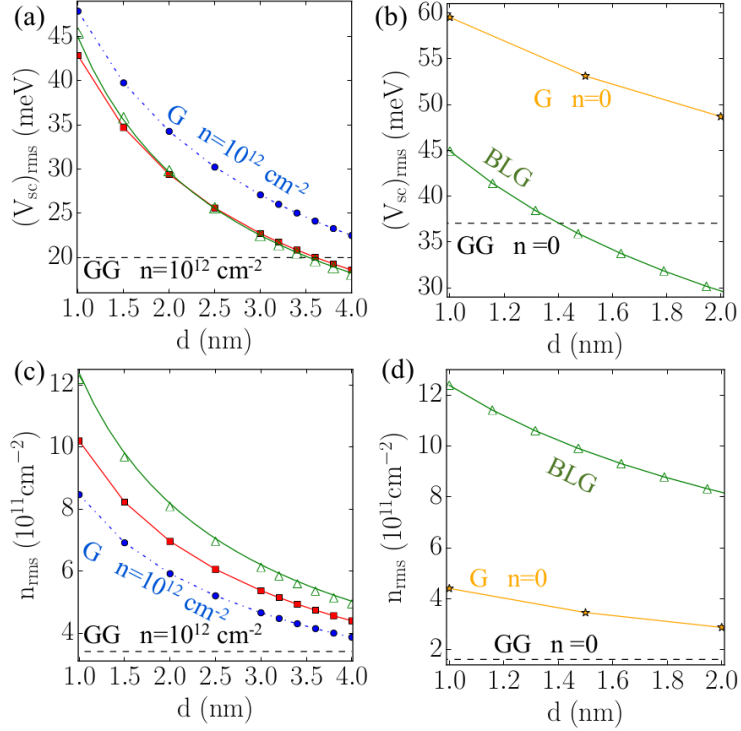
FIG. 3.38: Comparison of the potential fluctuations in SLG, BLG and SLG-SLG using TFD theory. In each panel, the black dashed line shows the value for SLG-SLG obtained with $d = 1.5$ nm, $\langle n \rangle = 10^{12}$cm^{-2}, and $n_{imp} = 5 \times 10^{11}$cm^{-2}. In (a) we show the screened disorder potential fluctuations as a function of the average distance d between the bottom graphene layer and the impurities. The blue dashed line corresponds to $\langle n \rangle = 10^{12}$cm^{-2} while the red solid line corresponds to SLG with $\langle n \rangle = 2 \times 10^{12}$cm^{-2}. The solid green line corresponds to the result for BLG with no random electric field effects while the empty triangles correspond to the case with the random electric field effects from the charged impurities. (b) Shows disorder average results at the charge neutrality point. (c) and (d) show the corresponding rms of the charge density fluctuations corresponding to (a) and (b) respectively.

89

Experimentally, the screening properties of SLG and SLG-SLG can be quantified through the single particle lifetime, which is obtained with Landau-level spectroscopy [149]. The graphene LL sequance is given by

$$E_n = E_D + \text{sgn}(n)\sqrt{2e\hbar v_F^2 |n|B} \ , \qquad (3.30)$$

where $n = 0, \pm 1, \pm 2, \ldots$ The square root dependence on B, and n is a signature of Dirac particles [36]. The LLs become visible when their energy scale $v_F\sqrt{2e\hbar B}$ is larger than the potential fluctuations ΔE_D. With this, we can define a critical field $B_0 \sim (\Delta E_D/v_F)^2/(2e\hbar)$, where the LLs become visible. For $B < B_0$, the system is governed by scattering with the impurities. $B > B_0$ implies $v_F\tau > l_B = \sqrt{\hbar/(eB)}$, where τ is the transport time. Measurements of the LL spectra as a function of the bias voltage and magnetic field strength on SLG and SLG-SLG confirm the expected square root dependence of E_n on B, and n. From these measurements we can extract the Fermi velocities $v_F = (1.10\pm0.02)\times10^6$ m/s for SLG and $v_F = (1.12\pm0.01)\times10^6$ m/s for SLG-SLG fitting Eq. (3.30). From Gaussian fits of the $n = 0$ LL, we can extract the potential fluctuations $\Delta E = 42$ meV, and $\Delta E = 18$ meV for SLG and SLG-SLG respectively. Fig. (3.39) shows the theoretical LL spectra as a function of the Fermi energy for two magnetic field strengths with a spectral broadening of 18 meV as measured for the case of SLG-SLG.

	SLG	SLG-SLG
LL spectroscopy	42 meV	18 meV
Numerical simulation	40 meV	20 meV

TABLE 3.1: Random potential fluctuations.
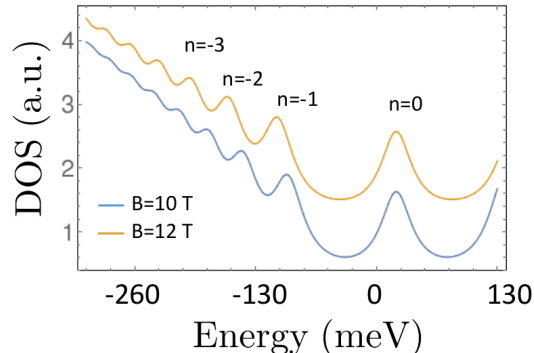
FIG. 3.39: Theoretical Landau-level spectra with a spectral broadening of 18 meV, as for the SLG-SLG heterostructure. The blue and yellow curves correspond to magnetic field strengths of 10 T and 20 T respectively. The curves are offset vertically for clarity. The LL index are indicated $n = 0, \pm 1, \pm 2, \cdots$.

From disorder averaged results using the same disorder parameters as shown in Fig. (3.37), we can extract the potential fluctuations and we obtain $\Delta E = 40$, and 20 meV for SLG and SLG-SLG respectively. These results are summarized in Table (3.1).

The evolution of LL spectra is now studied as a function of the gate voltage (average carrier density), which provides access to the maximum strength of the global disorder induced potential fluctuations across the sample. For clean samples, a stair-like LL spectrum is expected as a function of the carrier density [150]. This is because LL spectrum consists of peaks on the density of state (DOS), followed by regions where the DOS is very small. As the carrier density is increased, the LL are being filled, leading to a constant region in the LL spectrum. When the LL is

completely filled, there is a jump in the LL spectrum corresponding to the rapidly filled region in between LLs. This stair-like structure is smeared out in the presence of disorder. The presence of the random potential causes E_D to fluctuate across the sample. The gate voltage V_g deposits charges across the entire sample, not only close to the tip, as the bias voltage does. Then, as V_g is varied, the first electron will occupy a global minimum while the last injected electron will be close to the global maximum. As the Fermi energy increases, the spectrum measured by the STM tip shifts down in energy, tracing the random potential fluctuations. For the case of SLG, experiments show that the stair-like structure is completely smeared out at 10 T $\sim$ 115 meV which means that the potential fluctuations are larger than the LL spacing. For SLG-SLG, the stair structure can be distinguished. From the plateau slope, we find $\Delta E \sim 50$ meV.

In conclusion, it was demonstrated that the inclusion of a graphene layer as a buffer in between an insulating substrate and a 2D system reduces the random potential fluctuations both on local and global scales.

CHAPTER 4

Inter-layer excitonic superfluidity in double layer graphene

4.1 Introduction

This chapter is based in the work that can be found in Ref. [26]. In the context of bilayer systems, excitons are Coulomb-interaction-induced bound states composed of an electron locate on one layer, and a hole on the opposite layer, as shown schematically in Fig. (4.1). Bilayer exciton condensates are characterized by the spontaneous establishment of quantum coherence that supports counterflowing superfluids and were first predicted in semiconductor bilayers in the late sixties [151]. The possibility for room temperature superfluidity was first predicted in systems with quadratic band dispersion in Ref. [152]. The discovery of graphene has opened up a new playground for the investigation of exciton condensates due to its two-dimensional nature, its Dirac-like band structure, and vanishing semiconducting gap. The possibility to construct graphene heterostructures has opened up a new
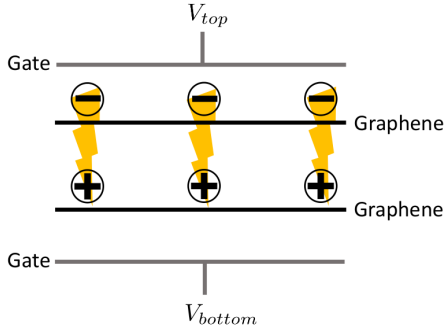
FIG. 4.1: Sketch of the exciton condensate in a graphene bilayer system where electron and holes are induced by independent external gates.

Coulomb interacting regime, where graphene layers can be placed close to each other yet the layers are electrically isolated. Previous works have predicted that interlayer Coulomb interactions might allow for the formation of a room-temperature exciton condensate at zero magnetic fields in double-single layer graphene [24, 25] (SLG-SLG), double bilayer graphene [133] (BLG-BLG), and hybrid SLG-BLG graphene systems [153]. Nevertheless, regardless experimental efforts, the condensate has not been observed at zero magnetic field [11, 154]. There are two possible explanations of this: (i) The excitonic gap is too small, such that the condensate is destroyed by thermal fluctuations, (ii) Disorder effects suppresses the gap beyond the experimental detection regime. In this Chapter, we focus on the effects of disorder induced by charged impurities trapped in the substrate of the system. As we studied in detail in Chapter 3, charged impurities induce spatial charge fluctuations that can be understood as differences in the chemical potential between the two layers that affects the perfect Fermi surface nesting required for the establishment of the condensate and therefore potentially suppress the critical temperature T_c.

In the clean limit, it is well known that the size of the gap depends on the assumption made for the screening of the interlayer Coulomb interaction [155–158]. In the unscreened Coulomb interaction approximation, it is found that SLG-SLG

heterostructures with hBN or SiO$_2$ separating the layers can support an exciton condensate at room temperature $T_c^{max} \approx 0.1 E_F$ [24, 25]. However, in the static screening approximation, it is found that the critical temperature is suppressed to immeasurable values $T_c^{max} \approx 10^{-7} E_F$. In between these two limiting cases, we have the dynamic screening approximation [157], which gives a gap that also lies in between the values found for the unscreened, and static screening approximations. The effect of vertex corrections [158], and inter-band transitions [157, 159] has also been reported before, and it has been shown that both effects enhance the critical temperature. The effect of the disorder has also been studied. In [160] it is shown that the exciton condensate survives the momentum scattering induced by short-range impurities in the strong interaction regime $k_F d < 1$. However, long-range disorder plays a key role, because the induced carrier density inhomogeneities lead to mismatches of the chemical potential that destroy the Fermi surface nesting necessary for the establishment of the condensate [126]. In the rest of this Chapter, we determine the experimental conditions under which the formation of the exciton condensate is expected. To do this we proceed in a three step program: (i) First, ignoring for the moment the spatial inhomogeities, we develop the theory for a homogeneous imbalanced system and determine the effect of the disruption of the Fermi surface nesting. The critical temperature T_c is determined for the cases of unscreened interlayer Coulomb interaction, and for static screening as a function of the total chemical potential ($\bar{\mu}$), and the mismatch ($\delta\mu$), given that these approximations represent the limiting cases of a vanishing gap and finite temperature superfluidity in SLG-SLG heterostructures. (ii) Then, as it was done in Chapter 3, we characterize the carrier density inhomogeneities for the parameters relevant for experiments using Thomas-Fermi-Dirac theory [29] to estimate $\delta\mu$. (iii) Lastly, we interpret the variance of the carrier density fluctuations as the typical Fermi surface

mismatch in the two layers.

4.2 Double single layer graphene

4.2.1 T_c for asymmetrically doped layers

In this section we study how a chemical potential imbalance affects T_c in SLG-SLG systems, assuming unscreened and statically screened interlayer Coulomb interactions. These two approximations over- and under-estimate the strength of the interactions respectively. Then, the calculation here presented is not intended as a quantitative estimation of T_c, but as the study of the impact of charge inhomogeneities for the most optimistic, and pessimistic scenarios. In what follows, we show that when $\delta\mu > 0$ is smaller than the excitonic gap (Δ), T_c remains finite. If $\delta\mu \sim \Delta$, then T_c is completely suppressed.

The Hamiltonian for single layer graphene in layer $\lambda = u, l$ and band $\nu = -, +$ is given by

$$H_{\lambda\nu} = \sum_{\mathbf{k}} (\nu\hbar v_F k - \nu\mu_\lambda) c^\dagger_{\mathbf{k}\lambda\nu} c_{\mathbf{k}\lambda\nu} , \qquad (4.1)$$

where v_F is SLG Fermi velocity. Let us assume that the upper layer is doped with electrons, and the lower layer with holes. Given that exciton condensation is dominated by processes around the Fermi surface, the empty upper valence and lower conduction bands are going to be disregarded. Then, the Hamiltonian for the full heterostructure can be written as

$$H = H_{u+} + H_{l-} + V_{up} , \qquad (4.2)$$

where V_{up} corresponds to the interlayer Coulomb interaction. The intralayer Coulomb

interaction only amounts to a renormalization of the Fermi velocity and it is there-
fore neglected [161]. With the particle-hole transformation $a_{\mathbf{k}} = c_{\mathbf{k}u+}$, and $b_{\mathbf{k}} = c_{\mathbf{k}l-}^{\dagger}$
the interlayer interaction can be written as

$$V_{up} = \sum_{\mathbf{k}\mathbf{q}} V(\mathbf{q}) f(\mathbf{k}+\mathbf{q}, \mathbf{k}) a_{-\mathbf{k}-\mathbf{q}}^{\dagger} b_{\mathbf{k}+\mathbf{q}}^{\dagger} b_{\mathbf{k}} a_{-\mathbf{k}} , \qquad (4.3)$$

where $V(\mathbf{q}) = V(\mathbf{q}, \omega = 0)$ is the Fourier transform of the static limit of the random
phase approximation (RPA) for the interlayer potential, and $f(\mathbf{k}, \mathbf{k}') = [1 + \cos(\theta_k -$
$\theta_{k'})]/2$ comes from the overlap of the Bloch states with momentum $\mathbf{k}$, and $\mathbf{k}'$. The
system is then characterized by the average chemical potential $\bar{\mu} = (\mu_u + \mu_l)/2$ and
difference $\delta\mu = \mu_u - \mu_l$. In other works relating to the excitonic condensate in
SLG-SLG, it was assumed that $\mu_u = \mu_l$ giving perfect nesting of the Fermi surfaces
in the two layers. [24, 25, 133, 152, 155–160, 162]. Within the mean-field theory and
the BCS approximation, the temperature-dependent gap function in the excitonic
channel $\Delta_{\mathbf{k}} = \langle b_{\mathbf{k}} a_{-\mathbf{k}} \rangle$ is given by[126]

$$\Delta_{\mathbf{k}}(T) = \sum_{\mathbf{k}'} V(\mathbf{k}' - \mathbf{k}) \frac{\Delta_{\mathbf{k}'}(T) f(\mathbf{k}, \mathbf{k}') N(\mathbf{k}', T)}{E_{\mathbf{k}'}} , \qquad (4.4)$$

where $N(\mathbf{k}', T) = n_\beta(\mathbf{k}', T) - n_\alpha(\mathbf{k}', T)$ is the finite temperature occupation factor
of the excitonic bands labeled by α and β, with $n_\alpha(\mathbf{k}, T) = \Theta(-\delta\mu/2 - \alpha E_{\mathbf{k}'})$ in
the $T = 0$ limit and $E_{\mathbf{k}'} = \left[(v_F k' - \bar{\mu})^2 + \Delta_{\mathbf{k}'}^2\right]^{1/2}$. The excitonic gap Δ is identified
as the peak value of this function, which, in the BCS limit, is found at $k = k_F$.
We define T_c as the lowest value of T for which the gap function is zero for all
k. We find this condition numerically, and it gives a value which is of the same
order of the standard BCS prediction $\Delta = 1.76 T_c$ for a constant gap approximation.
Our value for T_c is a little smaller due to the non-constant gap function and full

momentum-dependent interaction, which we retain in the calculation. We note as an aside that in the presence of the Fermi surface mismatch in the two layers (i.e., a chemical potential or density imbalance between the layers), there can, in principle, be inhomogeneous FFLO type solutions for the ground-state superfluidity in the system, but our general calculations allowing for the possibility of such inhomogeneous FFLO states fail to find any FFLO solutions and we consistently find either purely homogeneous superfluid condensate or no condensate. The interlayer screened interaction potential is calculated within the RPA, which is justified for double layer graphene because the fermion number $N = 8$ is large, as

$$V(\mathbf{q}, \omega) = \frac{v_q e^{-qd}}{1 + 2v_q \left(\Pi_u + \Pi_l\right) + v_q^2 \Pi_u \Pi_l (1 - e^{-2qd})}, \tag{4.5}$$

where $v_q = 2\pi e^2/(\epsilon q)$, Π_u and Π_l are the polarization functions for the upper and lower layers, respectively, and are functions of $\mathbf{q}$ and ω. They are given by [163]

$$\Pi(\mathbf{q}) = \frac{4}{A^2} \sum_{\mathbf{k}\alpha\beta} \frac{n_\alpha(\mathbf{k}, T) - n_\beta(\mathbf{k} + \mathbf{q}, T)}{\epsilon_{\alpha\mathbf{k}} - \epsilon_{\beta\mathbf{k}+\mathbf{q}} + i0^+} f(\mathbf{k}, \mathbf{k} + \mathbf{q}) . \tag{4.6}$$

To gain some insight in the approximation of the interlayer interaction potential, we analyze the potential in Eq. (4.5). Fig. (4.2a) shows the statically screened interlayer interaction potential divided by the unscreened interaction $V_q = 2\pi^2 e^{-qd}/(\epsilon q)$ for SLG-SLG with $\epsilon = 3.9$ as a function of momentum q. We show curves for the cases $k_F d = 0$ (strongest interaction limit), $k_F d \ll 1$ (low-density limit), and $k_F d > 1$ (hight density limit). For high carrier densities, the static screening potential becomes weaker due to the larger density of states that allows a more efficient screening of the impurities. The observed flattening of the three curves for $q > 2k_F$ is because up to $q = 2k_F$, the polarizability is constant, increasing after that [163].

Notice that for $q < k_F$, the screened potential is one order of magnitude smaller that the unscreened potential. Since the dynamically screened potential has also been considered by other authors, in Fig. (4.2b) we show the dynamically screened potential normalized by the unscreened potential V_q as a function of wave vector for various frequencies and $k_F d = 0$. In this limit, the interaction is a universal function of q/k_F. For $q/k_F < \omega/\bar{\mu}$, the polarization functions are negative [163] and therefore it is possible for the finite frequency potential to have a divergence corresponding to the plasmon wave vector k_p. The potential also is negative [1] for $k_p/k_F < q/k_F < \omega/\bar{\mu}$ indicating an overall repulsive interaction which could reduce the gap size. In contrast, we note that for $q < k_p$, the interaction is enhanced over the unscreened case. This is the well-known anti-screening effect of dynamic screening, which should to some extent compensate for the sign change of the interaction in some regime of the phase space. For $q/k_F > \omega/\bar{\mu}$, the potential is very similar to the statically screened case. The most relevant frequency range is $\omega \approx \Delta$, which is in general rather small compared to $\bar{\mu}$ and hence the range of wave vectors where the potential deviates substantially from the statically screened case is small, indicating that T_c with dynamic screening will be closer to that predicted by the static screening calculation than the unscreened one. This analysis also shows that a system with a large bare gap will be more robust against dynamic screening effects since the relevant frequency will be higher, implying that within the range of q that contributes strongly to the integrand in Eq. (4.4), we have $V(q, \omega)/V_q > 1$.

We start studying the optimistic case corresponding to the unscreened Coulomb interaction with a small layer separation of $d = 1$ nm and hBN substrate ($\epsilon = 3.9$). As it is shown in Fig. (4.3a), we obtain a critical temperature of the order of 100 K

---

[1]Note that the overall negative sign for an attractive interaction is absorbed into the definition of the gap function in Eq. (4.4).
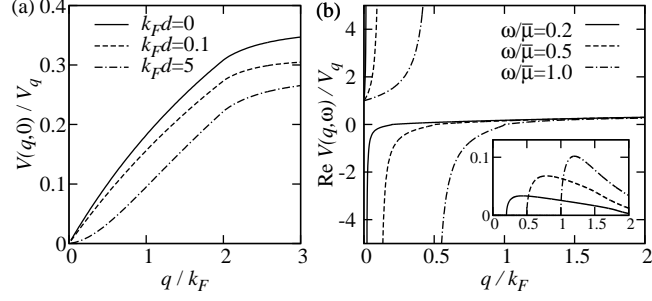
FIG. 4.2: Comparison of (a) the statically screened and (b) the real part of the dynamically screened interlayer interaction potentials to the unscreened interaction $V_q = 2\pi^2 e^{-qd}/(\epsilon q)$ for SLG-SLG with $\epsilon = 3.9$. The inset to (b) shows the imaginary part of the interaction.

for realistic doping and moderate imbalance. Figs. (4.3c) and (4.3d) show cuts of T_c as a function $\bar{\mu}$, and $\delta\mu$ respectively. T_c monotonically increases with $\bar{\mu}$ given that we have more quasiparticles available for pairing while an increase on the imbalance $\delta\mu$ suppresses T_c. If the graphene layers are as close as $d = 1$ nm, tunneling events that favor the pairing might take place [159]. In our work, we ignore this effect. Fig. (4.3b) shows T_c for the case $d = 5$ nm, where tunneling events are negligible. In this regime, we obtain $T_c \approx 50$ K. The same calculation was performed for the case of static screening, but given that the interlayer interaction is too small, the numerical procedure failed to find a non-zero solution with accepted error. In order to obtain a finite numerical result for Δ, we assume that it is momentum independent [155]. With this approximation, we obtain Fig. (4.4). In Fig. (4.4a) we show T_c as a function of the average chemical potential. We find that T_c presents a maximum value that depends on the interlayer separation. Fig. (4.4b) we show T_c as a function of the Fermi surface imbalance. We observe that variations of the order of nano eV are enough to destroy the condensate.

100
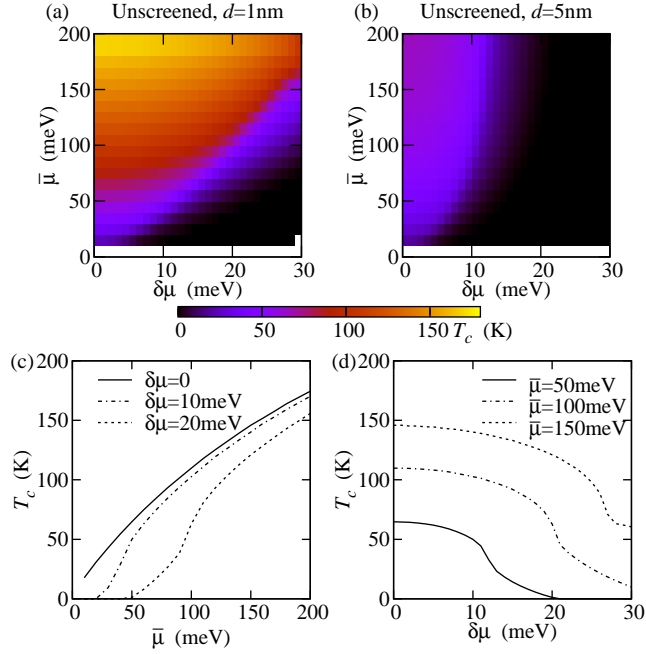
FIG. 4.3: (Color online.) T_c for the unscreened interaction in dielectric environment $\epsilon = 3.9$. (a) and (b) show color plots as a function of $\bar{\mu}$ and $\delta\mu$ for $d = 1$nm and $d = 5$nm, respectively. (c) T_c as a function of $\bar{\mu}$ for various $\delta\mu$ and $d = 1$nm. (d) T_c as a function of $\delta\mu$ for various $\bar{\mu}$ and $d = 1$nm.

4.2.2 Charge inhomogeneity in SLG-SLG

In any experimental sample, some degree of extrinsic disorder-induced charge inhomogeneity will exist, as has been demonstrated by many surface measurements in SLG. [90, 99, 164] In a double-layer device, the inhomogeneities in the charge landscape will not be identical in both layers, and therefore there will be spatial variation in the asymmetry of the chemical potentials. In this situation, the local difference in chemical potential has two contributions. There is a nominally homogeneous part which is induced by gating and is, in principle, controllable. This contribution was the subject of the previous section and we ignore it here. Then there is a contribution from charged impurities and other disorder that is inhomogeneous and not controllable. A full analytical description of the inhomogenous system
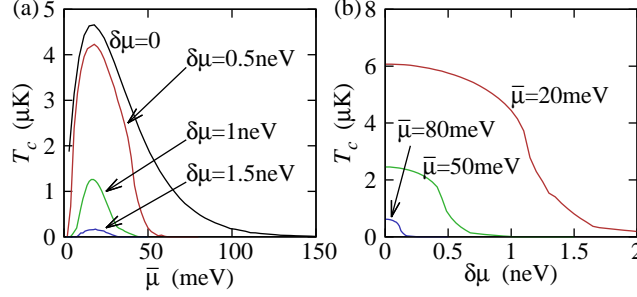
FIG. 4.4: (Color online.) Static interlayer screening for SLG-SLG with $\Delta_{\mathbf{k}} = \Delta_{k_F}$. (a) For various $\delta\mu$ as a function of $\bar{\mu}$, and (b) for various $\bar{\mu}$ as a function of $\delta\mu$. Note that the scale on the vertical axis is micro-Kelvin.

is clearly intractable so we employ an accurate numerical method to compute the charge density of the system when charged impurities explicitly break translational symmetry. From this charge landscape, we can assign the local chemical potential $\mu_u(\mathbf{r})$ and $\mu_l(\mathbf{r})$ in each layer, and characterize the spatial fluctuations by their root-mean square (rms) value, which is a measure of the typical fluctuation. Using this measure of the disorder in the charge landscape, we can discuss the stability of the condensate against the density and chemical potential inhomogeneity induced by the charged impurities. In principle, it is possible that some correlation will exist between charged impurities, although the nature of these correlations will depend on details of the system. We wish to avoid introducing extra parameters to describe this, so we assume uncorrelated disorder for the purposes of this work. If correlations are shown to be important, then they can be included within the theory we are about to describe in the same way as Ref. [118]. To calculate the charge landscape in each layer taking into account the presence of long-range disorder due to the charged impurities and nonlinear screening effects we use the TFDT. [12, 29] The TFDT is a generalization to Dirac materials of the Thomas-Fermi theory. A detailed description of the method can be found in Chapter 3 of this dissertation. As we have seen, the ground-state density distributions $n_u(\mathbf{r})$ and $n_l(\mathbf{r})$ are obtained

by minimizing the energy functional $E[n_u, n_l]$ (see Eq. (3.8)) numerically enforcing the self-consistency of the distribution in the two layers due to the interlayer interaction. Then, the local difference in chemical potential between the two layers $\delta\mu_{\mathrm{loc}} = \mu_u(\mathbf{r}) - \mu_l(\mathbf{r})$ can be extracted for each point in the system and by performing the minimization for many (~ 600) disorder realizations and we obtain statistics for the distribution function of $\delta\mu_{\mathrm{loc}}$. In Fig. 4.5 we show the spatial distribution of $\delta\mu_{\mathrm{loc}}$
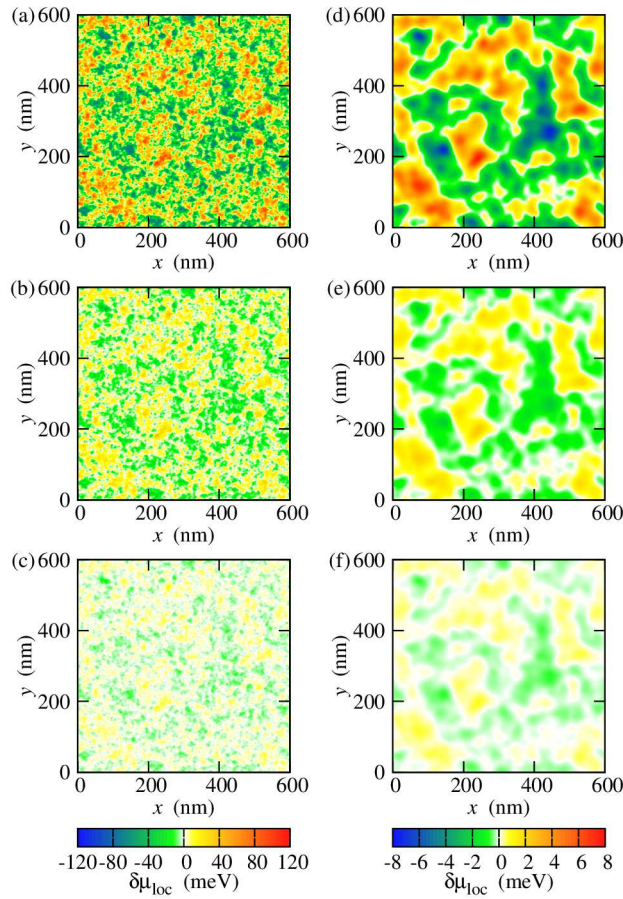
FIG. 4.5: (Color online.) Spatial plots of $\delta\mu$ calculated via the TFDT. The left column is for $d = 1$nm, $d_{12} = 1$nm, and $\bar{\mu} = 50$meV. The right column is for $d = 5$nm, $d_{12} = 20$nm, and $\bar{\mu} = 200$meV. The color bar at the bottom of each column applies to all three plots in each column. The first row is for $n_{imp} = 10^{11}$cm^{-2}, the second row is $n_{imp} = 10^{10}$cm^{-2}, the third row is $n_{imp} = 10^{9}$cm^{-2}.

for three different impurity densities and in two experimentally relevant geometries.

103

In the left column, we show data where the lower graphene layer is placed directly onto an SiO_2 substrate and the interlayer separation is $d = 1$nm. In this case, the charged impurities at the oxide interface are at an effective distance $d_{12} = 1$nm away from the bottom graphene layer. This situation is relevant for the configuration used in the experiments in Ref. [165]. For concreteness, we set $\bar{\mu} = 50$meV, corresponding to an easily achievable carrier density regime. The results shown in the right column are relevant for the the experiments in Ref. [11], where the lower graphene layer is seperated from the SiO_2 substrate by a 20nm layer of hBN. In this case, we take $d_{12} = 20$nm, and we also set $\bar{\mu} = 200$meV corresponding to the high carrier density regime where we expect the screening of the external impurities to be the most efficient, resulting in the lowest amount of charge inhomogeneity. In both situations we assume that the gate-induced (homogeneous, controllable) part of the layer asymmetry to be zero. Therefore we assume that any layer imbalance is completely defined by the charged impurities. The rows of Fig. 4.5 show the data for, from top to bottom, $n_{imp} = 10^{11}$cm^{-2}, 10^{10}cm^{-2}, and 10^9cm^{-2}. (We note that the higher value of n_{imp} is more typical, and $n_{imp} = 10^9$cm^{-2} is unlikely to be achieved in laboratory graphene samples on any substrate. Typically, one can get an estimate of n_{imp} in a particular sample by looking at the carrier density regime over which the graphene minimum conductivity "plateau" exists around the Dirac point. [39]). All six plots share some similar qualitative features. In particular, they all show regions where $\delta\mu$ is positive and regions where it is negative with narrow strips in between where $\delta\mu$ is small. The lengthscale of the fluctuations is not affected by the impurity density, but the magnitude of the fluctuations is. By comparing the data in the two columns we see that the distance of the impurities from the SLG-SLG makes a substantial difference in the length scale of the fluctuations in $\delta\mu_{\mathrm{loc}}$, and in reducing the magnitude of the fluctuations. The density of impurities also has

a strong effect on the magnitude of the fluctuations in $\delta\mu_{\mathrm{loc}}$ with the fluctuations reducing by approximately a factor of three with each order of magnitude decrease in n_{imp}. In the most dirty case (it should be noted that graphene on SiO_2 can have an impurity density of up to $5 \times 10^{12}\mathrm{cm}^{-2}$ as measured by transport measurements [39]), shown in Fig. 4.5(a) then the fluctuations in $\delta\mu_{\mathrm{loc}}$ may be of the order of $\bar{\mu}$, indicating that the condensate has no opportunity to form in this case. For the cleanest situation shown in Fig. 4.5(f), the potential imbalance is on the scale of 1meV and there is a significant chance that excitons with a gap of the size predicted by dynamic screening calculations [157] will persist in spite of the disorder if an impurity density as low as $10^9\mathrm{cm}^{-2}$ can be achieved in double layer graphene samples. Now we take many disorder realizations (~ 600) for each impurity density and
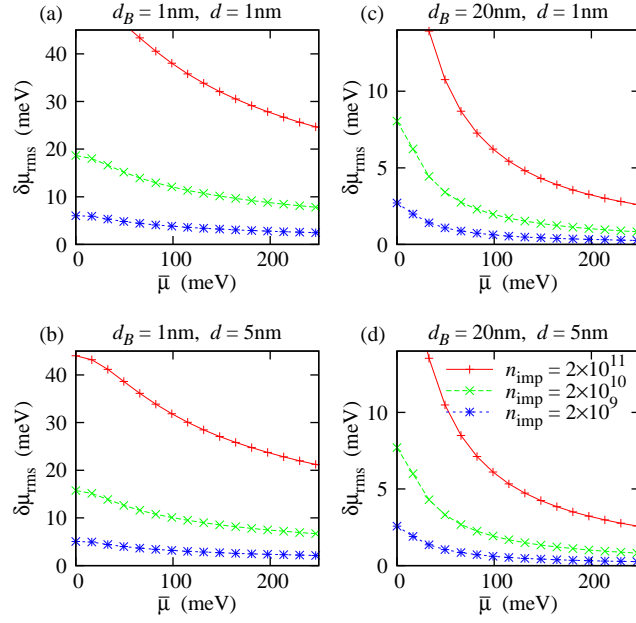
FIG. 4.6: (Color online.) Root-mean-square of the distribution of the local $\delta\mu$ as a function of the global chemical potential for two experimentally relevant geometries. (a),(b) $d_{12} = 1$nm, $\epsilon = 3.9$ corresponding to double layer graphene placed straight onto a SiO_2 substrate. (c),(d) $d_{12} = 20$nm, $\epsilon = 3.9$ corresponding to double layer graphene placed onto a 20nm slab of hBN.

collect ensemble-averaged statistics for the distribution of $\delta\mu_{\mathrm{loc}}$. We characterize this distribution by its root-mean-square value, which we label $\delta\mu_{\mathrm{rms}}$. In Fig. 4.6 we plot $\delta\mu_{\mathrm{rms}}$ for the two experimental geometries discussed above and for different interlayer spacing d. This is shown in Figs. 4.6(a) and 4.6(b) for $d = 1$nm and $d = 5$nm, respectively, for three impurity densities covering three orders of magnitude. The fluctuations are strongest at low carrier density, where the screening of the impurity potential is weakest, and it decreases monotonically with increasing $\bar{\mu}$. The trend suggested by the spatial plots is confirmed here, that is, decreasing the impurity density by a factor of ten generates approximately a factor of three reduction in the fluctuations. If the impurities are moved away from the SLG-SLG by a spacer layer as in Figs. 4.6(c) and 4.6(d) we find that the fluctuations in $\delta\mu$ are reduced to the order of 1meV. This degree of fluctuation may be small enough to allow the condensate to be detected at a reasonable temperature scale. For the $d_{12} = 1$nm case, a system dimension of 160 unit cells was chosen. For $d_{12} = 20$nm we increased that to 320 unit cells to ensure that the system was large enough to accurately capture the size of the typical fluctuations.

4.3 Conclusion

In conclusion, in this chapter we have presented an analysis of the effects of carrier density inhomogeneities induced by charged impurities on the critical temperature for the exciton condensate in double layer graphene systems. It was found that the presence of charge inhomogeneities, which alter the perfect Fermi surface nesting required for the exciton condensate formation is likely to be a limiting factor for the experimental observation of the condensate. For the screening properties of the system we considered the cases of unscreened, and statically screened interlayer

Coulomb interactions which correspond to the most optimistic, and more pessimistic scenarios, respectively.

The electronic density ground state was characterized for parameters relevant to experiments, and we found that in the case of statically screened interlayer Coulomb interaction chemical potential imbalances of the order of nano electronvolts are enough to destroy the condensate. Given the typical carrier density fluctuation found in double layer graphene systems, the observation of a exciton condensate is very unlikely. However, for the most optimistic case of the unscreened interlayer Coulomb interaction, the exciton condensate is robust against chemical potential imbalances up to the order of 10 meV with a critical temperature $T_c \approx 100$ K. These results leave room for experimental observation only in the cleanest double layer graphene systems.

CHAPTER 5

Topological insulator-graphene heterostructures: Transport and spin density accumulation.

5.1 Introduction

In this chapter, we move on to heterostructures with spin-orbit coupling (SOC), and to their application for spintronic devices. One of the main goals of the subfield of spintronics is the use of the spin degree of freedom in electronic systems, rather than the charge, to manipulate and store information. The main advantage in using the spin resides in the fact that spin currents are not necessarily dissipative [166].

One of the most challenging problems on the field consists in finding an efficient way to control the magnetization of nanoscale ferromagnetic devices using electric currents [167]. Many different mechanisms have been proposed to this end, for example, the use of the spin Hall effect in heavy metals [53, 168], or the Rashba-Edelstein

effect in ferromagnets [169, 170]. However, the recent discovery of topological insulators (TI) [69, 74] opened up a new possibility to obtain optimal spin control using electric currents. As was described in the introduction, TIs are new states of matter that are insulating in the bulk and host Dirac conducting states at the surface, protected by time reversal symmetry [46]. Given that the chirality operator commutes with the TI Hamiltonian, the spin direction is locked with the momentum direction. This property allows for the creation of a non-equilibrium current-induced spin density accumulation on the TI surface when a forward-backward carrier imbalance is produced. Such a mechanism is known as the inverse spin-galvanic effect [171, 172] and such a spin density could act as an effective magnetic field that could be used to manipulate the magnetization direction of a ferromagnet placed on top of the TI. Several theoretical works have extensively studied the inverse spin-galvanic effect in TI systems [173–176]. Recently, strong spin torques have been measured in TI-metallic ferromagnet bilayers [177] consistent with the contribution expected from the TI surface states. Unfortunately, the mobility of quasiparticles on the TI surface is rather low compared with other Dirac materials, such as graphene [178]. In this work, we propose the use of a layered heterostructure composed of a graphenic layer (single layer graphene (SLG) or bilayer graphene (BLG)) placed on top of a TI (TI|SLG system or TI|BLG system) in order to increase the mobility of quasiparticles and therefore the efficiency of the spin accumulation creation. In order to detect the spin density accumulation, an insulating ferromagnet is placed on top of the graphene layer. The TI|G system combines the high mobility of graphene with the strong SOC of the TI.

There is compelling evidence that in Dirac materials, the dominant source of disorder is most likely charged impurities trapped in the bulk of the material or in the substrate [179]. In the low doping regime, these long-range impurities shift the

Fermi energy away from the TI Dirac point inducing the formation of electron-hole puddles [29, 31]. A detailed description of the effect of electron-hole puddles on the transport properties in Dirac materials is beyond the scope of this chapter. For our current purposes, the disorder is modeled as a uniform two-dimensional impurity density distribution located an effective distance d away from the surface of the 3DTI. In order to build some intuition, and for the sake of comparison, the case of short-range disorder will also be considered. In general, the Hamiltonian for the family of systems that we are interested in can be written as

$$H = \sum_{\mathbf{k}} c_{\mathbf{k}}^{\dagger} H_{\mathbf{k}} c_{\mathbf{k}} + \int d\mathbf{r} d\mathbf{r}' c^{\dagger}(\mathbf{r}) V_{dis}(\mathbf{r}, \mathbf{r}') c(\mathbf{r}') \ , \tag{5.1}$$

where $H_{\mathbf{k}}$ corresponds to the clean Hamiltonian in momentum space, and $V_{dis}(\mathbf{r}, \mathbf{r}')$ corresponds to the disorder potential. When modeling these heterostructures, we have to consider the possible ways in which the graphene layer couples to the TI layer. In the most optimistic case, we can achieve coherent tunneling between the layers. In the most pessimistic case, the layers are decoupled we fall in a regime where neither momentum nor spin is conserved by tunneling events.

5.2 Coherent tunneling regime

In this section, we focus on the case in which graphene and the TI hybridize and coherent tunneling between them is obtained. Let us assume a commensurate stacking between the graphene hexagonal lattice and the TI triangular lattice, as

110
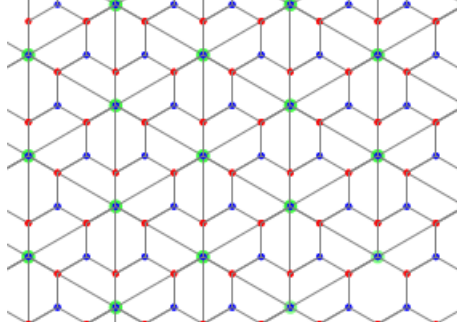
FIG. 5.1: Schematic of the $\sqrt{3} \times \sqrt{3}$ stacked graphene (red and blue sites) and TI (green sites) real space lattices.

shown in Fig. (5.1). The Hamiltonian for such a system is given by [180]

$$
H_{\mathbf{k}} = \begin{pmatrix} \hat{H}_{\mathbf{k}}^{G,K} & 0 & \hat{T}^{\dagger} \\ 0 & \hat{H}_{\mathbf{k}}^{G,K'} & \hat{T}^{\dagger} \\ \hat{T} & \hat{T} & \hat{H}_{\mathbf{k}}^{TI} \end{pmatrix} + \hat{H}_{\text{ex}}, \tag{5.2}
$$

where $\hat{H}_{\mathbf{k}}^{G,K}$ corresponds to the low energy Hamiltonian for the graphenic layer around the K point, and $\hat{H}_{\mathbf{k}}^{G,K'} = \left(\hat{H}_{\mathbf{k}}^{G,K}\right)^*$ corresponds to the Hamiltonian around the K' point. For the case of BLG, the Hamiltonian is given by

$$
\hat{H}_{\mathbf{k}}^{BLG,K} = \hbar^2 k^2/(2m^*)\sigma_0 \otimes [\cos(2\phi_{\mathbf{k}})\tau_x + \sin(2\phi_{\mathbf{k}})\tau_y] - \mu_g \sigma_0 \otimes \tau_0 , \tag{5.3}
$$

where σ_i corresponds to the Pauli matrices in spin space, τ_i corresponds to the Pauli matrices in pseudospin space, and the coefficient m^* corresponds to the effective mass of the quasiparticles. For the case of SLG we have

$$
\hat{H}_{\mathbf{k}}^{SLG,K} = \hbar v_g k \sigma_0 \otimes [\cos(\phi_{\mathbf{k}})\tau_x + \sin(\phi_{\mathbf{k}})\tau_y] - \mu_g \sigma_0 \otimes \tau_0 , \tag{5.4}
$$

111
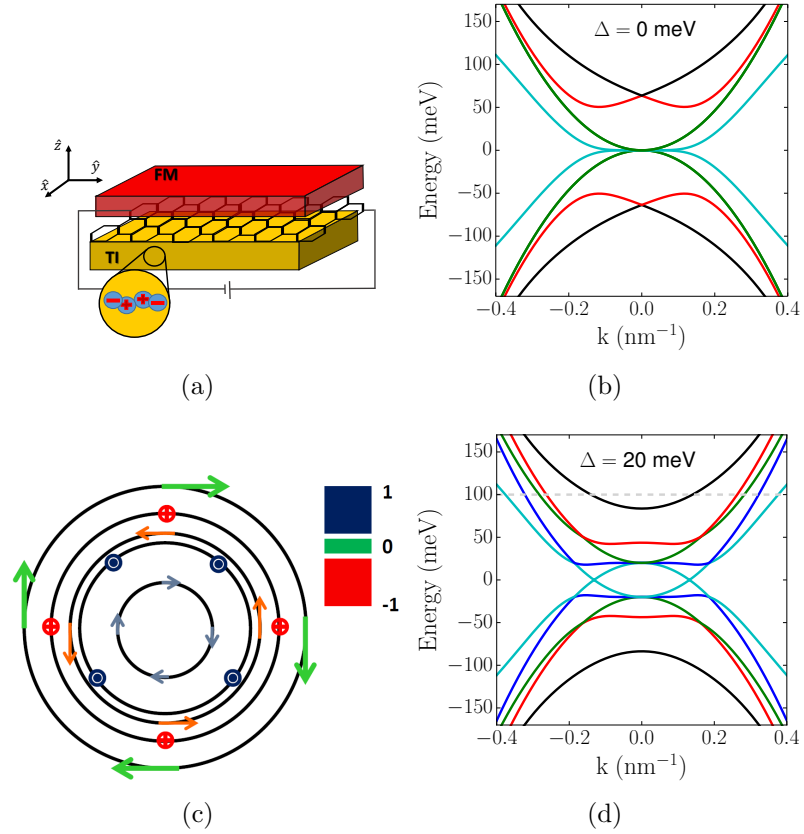
FIG. 5.2: (a) Sketch of the most general heterostructure considered in this work. The system consists on a graphene sheet placed between a 3D topological insulator, and an insulating ferromagnet which acts as the active layer. (b) Band structure for a TI|BLG system. (c) Spin texture, and (d) band structure of a TI|BLG|FM heterostructure with an exchange field $\Delta = 20$ meV.

where v_g is the Fermi velocity. The TI surface states are described by the Hamiltonian

$$\hat{H}_{\mathbf{k}}^{TI} = \hbar v_{TI} \left(k_y \sigma_x - k_x \sigma_y \right) - \mu_{\mathrm{TI}} \sigma_0 \ . \tag{5.5}$$

The momentum- and spin-conserving tunneling matrix connecting the graphene and TI states is assumed to have the form

$$\hat{T}_{\mathbf{k}} = \begin{pmatrix} t & 0 & 0 & 0 \\ 0 & 0 & t & 0 \end{pmatrix} \ . \tag{5.6}$$

Lastly, $\hat{H}_{ex} = \vec{\Delta} \cdot \vec{S}$ corresponds to the exchange Hamiltonian, that couples locally the TI surface states and the graphene states to the FM. The operator $\vec{S} = (S_x, S_y, S_z)$ corresponds to the heterostructure spin operator, given by

$$\hat{S}^x = \frac{1}{2} \begin{pmatrix} \sigma_x \otimes \tau_0 & & \\ & \sigma_x \otimes \tau_0 & \\ & & \sigma_x \end{pmatrix} \tag{5.7}$$

$$\hat{S}^y = \frac{1}{2} \begin{pmatrix} \sigma_y \otimes \tau_0 & & \\ & \sigma_y \otimes \tau_0 & \\ & & \sigma_y \end{pmatrix} \tag{5.8}$$

$$\hat{S}^z = \frac{1}{2} \begin{pmatrix} \sigma_z \otimes \tau_0 & & \\ & \sigma_z \otimes \tau_0 & \\ & & \sigma_z \end{pmatrix} \ . \tag{5.9}$$

The renormalized band structure is obtained by direct diagonalization of the Hamiltonian of the system Eq. (5.2). In Fig. (5.2b) the bands of a TI|BLG heterostructure are plotted for a tunneling amplitude $t = 45$ meV and no band-crossing point mis-
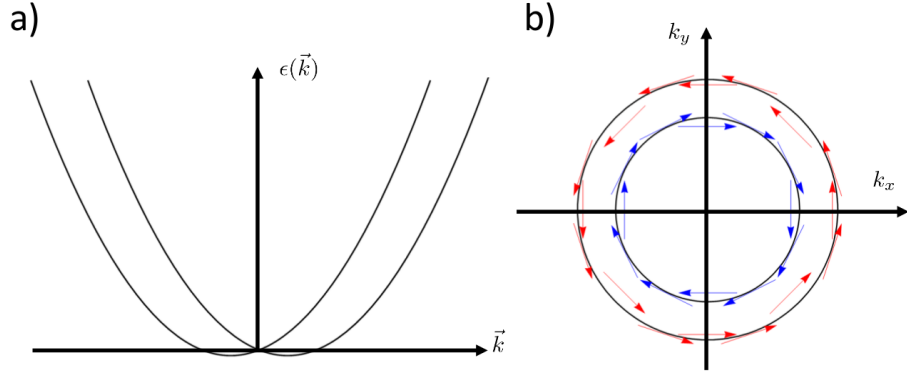
FIG. 5.3: (a) Rashba-split 2DEG energy bands. (b) Rashba spin texture.

match, $\delta\mu \equiv \mu_{TI} - \mu_g = 0$ meV. The strong spin-orbit coupling of the TI surface states induces the development of Rashba-split type bands in graphene, which correspond to the bands with the highest energy for fixed momentum.

In the context of quantum wells and 2D electron gases (2DEG), a phenomenological Rashba SOC term in the Hamiltonian is allowed when inversion symmetry is broken. This term was first introduced to understand resonance experiments in GaAs|Al$_x$Ga$_{1-x}$As heterostructures [181]. The Rashba term has the form $H_R = \alpha_R/\hbar \, (\hat{n} \times \vec{p}) \cdot \vec{\sigma}$, where α_R is the Rashba coupling constant, and $\hat{n}$ is the direction perpendicular to the heterostructure. In quantum wells, this term is allowed due to the presence of an electric field $\vec{E} = E\hat{n}$ generated by charge transfer at the interface of the two layers conforming the heterostructure. Fig. (5.3a) shows the band structure for a 2DEG with Rashba SOC. The Rashba term induces a band splitting. In Fig.(5.3b) we plot the spin orientation $\langle\vec{\sigma}\rangle$ of the Bloch states for the Rashba-split 2DEG. We refer to the spin orientation as spin texture. Compare with the spin texture for the TI|BLG heterostructure shown in Fig. (5.2c).

The band structure for a system with a FM with out-of-plane magnetization and exchange field strength $\Delta = 20$ meV is shown in Fig. (5.2d). Zeeman splitting in the higher energy bands is now obtained. In Fig.(5.2c) shows the spin texture for

TI|BLG. The circles show the spin texture along constant energy contours. The spin winds around the $\mathbf{k} = 0$ point either clockwise or counter-clockwise depending on the band. The spins also exhibit either aligning or anti-aligning with the exchange field, depending on the band considered.

Experiments have reported the presence of a Rashba spin-split two-dimensional electron gas in TIs [182] created close to the surface due to band bending, which could give an important contribution to the net spin density accumulation. However, spin-transfer torque measurements [177] in TI|FM systems suggest that the spin accumulation is consistent with what is expected from the TI surface states. For this reason, we ignore possible contributions coming from the Rashba spin split two-dimensional electron gas. Another possible contribution to the spin accumulation could come from TI bulk states because impurities usually locate the TI Fermi energy close to the bulk bands. However, experiments have shown the possibility to tune the location of the Fermi energy by doping [183–185], applying stress to the sample [186], and reducing the defects when growing the films [187]. Also, transport measurements performed in TI thin films have shown results consistent with contributions coming mostly from the surface states [188]. Hence, only the TI surface states are considered in our model.

The current-induced non-equilibrium spin density δs^i, using the Kubo formalism [49, 189] in the linear response regime, is given by $\delta s^i = \chi^{ij} E_j$, where χ^{ij} corresponds to the non-equilibrium current-induced spin density response function. Due to the rotational symmetry of the clean system along the axis perpendicular to the sample, the response function tensor components satisfy $\chi^{xy} = -\chi^{yx}$ and $\chi^{xx} = \chi^{yy}$. Given these symmetry properties, without loss of generality, we will consider an electric field applied along the y-direction.

The case of a TI|FM heterostructure in the presence of short-range disorder

has been extensively studied in the literature. One of the earliest works can be found in Ref. [173], where it was shown that a non-zero spin accumulation in the y-direction is present. This accumulation is dissipationless for $E_F < \Delta$ and is related to the anomalous Hall effect. In Ref. [174], the magnetization dynamics was investigated via the derivation of the Landau-Lifshitz-Gilbert (LLG) equation, and the doped case was studied. More recently, in Ref. [175] spin torques in the presence of transverse fluctuation in the magnetization were calculated. The existing results are for the case of short range, spin- and momentum-independent disorder, and are as follows. In the limit $|E_F|(2\tau_0/\hbar) \gg 1$, and for $|E_F| > |\Delta|$, the non-zero components of the response function are $\chi^{xy} = \frac{e\hbar^2 v_{TI}}{2\pi u_0}(1 - (\Delta/E_F)^2)(1 + (\Delta/E_F)^2)^{-1}$, and $\chi^{yy} = +e(\pi v_{TI})^{-1}E_F\Delta(E_F^2 + \Delta^2)(E_F^2 + 3\Delta^2)^{-2}$. For $|E_F| < |\Delta|$ the only non-zero component is $\chi^{yy} = e(8\pi v_{TI})^{-1}$. Candidate materials to realize this system include Bi_2Se_3, Bi_2Te_3, and Sb_2Te_3 for the TI, and Europium Oxide (EuO) for the insulating FM. MnSe, an antiferromagnet (AFM), whose magnetic moments in each (111) plane are aligned has also been considered. In Ref. [190], first principles calculations were performed using different magnetic materials with lattice structures compatible with bismuth-based topological insulators. It was found that $Bi_2Se_3|MnSe$ is the best combination of all considered materials since it possesses strong exchange coupling ($\Delta \approx 50\,\mathrm{meV}$) and surface state bands. Now we turn our attention to the calculation of the response of the heterostructures. We first evaluate the response function at $T = 0$ K in the DC limit, as shown diagrammatically in (5.4b). Written in the eigenbasis $\{|a\mathbf{k}\rangle\}$ of the clean Hamiltonian $H_\mathbf{k}$ (5.2), the spin density response
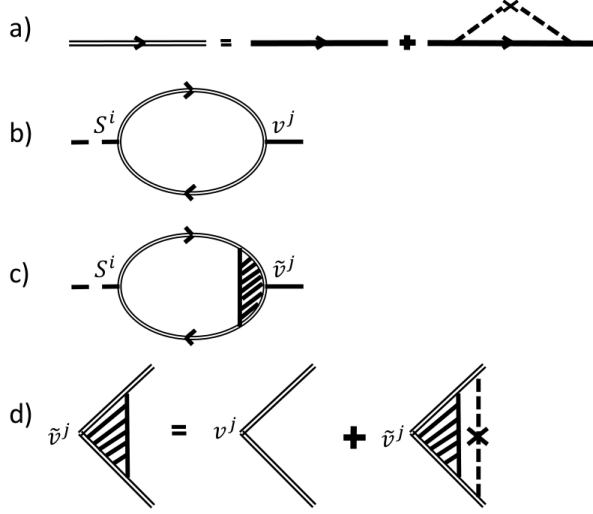
FIG. 5.4: Feynman diagrams for (a) the disorder averaged Green's function, (b) the current-induced spin density response with bare velocity operator, (c) the current-induced spin density response with the dressed velocity operator, and (d) the Bethe-Salpether equation for the dressed velocity operator.

function is given by

$$
\chi^{ij} = \frac{\hbar e}{2\pi V} \operatorname{Re} \sum_{\mathbf{k},a,b} s_{ab}^i(\mathbf{k}) v_{ba}^j(\mathbf{k}) \left(G_{\mathbf{k}a}^A G_{\mathbf{k}b}^R - G_{\mathbf{k}a}^R G_{\mathbf{k}b}^R \right) - \frac{\hbar e}{\pi V} \sum_{\mathbf{k},a,b} \operatorname{Im}\{ s_{ab}^i(\mathbf{k}) v_{ba}^j(\mathbf{k}) \}
$$
$$
\times \int_{-\infty}^{E_F} dx \, \operatorname{Im} \left\{ \left(\frac{\partial}{\partial x} G_{\mathbf{k}a}^R(x) \right) G_{\mathbf{k}b}^R(x) \right\} , \tag{5.10}
$$

where s^i is the spin operator, $v^i = \hbar^{-1} \partial/\partial k_i H_{\mathbf{k}}$ is the velocity operator, and the expectation value is defined as $O_{ab}^i(\mathbf{k}) \equiv \langle a\mathbf{k}|O^i|b\mathbf{k}\rangle$. The disorder-averaged Green's function (see Fig.(5.4a)) is given by $G_a^{R/A} = (E_F - \epsilon_{\mathbf{k}a} \pm i\hbar(2\tau_0)^{-1})^{-1}$ in this eigenbasis, where τ_0 corresponds to the band- and momentum-dependent single particle lifetime. The single particle lifetime τ_0 of the quasiparticles is given to leading order, by

$$
\frac{\hbar}{\tau_{0a}} = 2\pi \sum_{a'\mathbf{k}'} n_{imp} \left| \frac{v(q)}{\epsilon(q)} \right|^2 |\langle a'\mathbf{k}'|a\mathbf{k}\rangle|^2 \delta(\epsilon_{a,\mathbf{k}} - \epsilon_{a',\mathbf{k}'}) , \tag{5.11}
$$

where $\mathbf{k}$, and $\mathbf{k}'$ correspond to the incoming and outcoming momentum, and $\mathbf{q} =$

$\mathbf{k} - \mathbf{k}'$. n_{imp} is a 2D effective impurity density, which throughout this work is equal to $n_{imp} = 1 \times 10^{12} \mathrm{cm}^{-2}$. $v(q) = 2\pi e^2 e^{-qd}/(\kappa q)$ is the Fourier transform of the potential generated by the charged impurities located at an effective distance d away from the TI surface, and κ is the static dielectric constant appropriate for graphene on TI. The static dielectric constant κ for TIs is usually large [30]. For example, $\kappa_1 \approx 100\epsilon_0$ for Bi_2Se_3. The effective dielectric constant appropriate for graphene is then $\kappa = (\kappa_{TI} + \kappa_{top})/2$, where we assume $\kappa_{top} = 1$. The dielectric function $\epsilon(q)$ is calculated in the random phase approximation (RPA), and is given by $\epsilon^{RPA}(q) \approx 1 - v_c(q)\chi_{nn}^0(q)$, where $v_c(q) = 2\pi e^2/(\kappa q)$ is the Fourier transform of the Coulomb potential generated by electron-electron interactions and $\chi_{nn}^0(q)$ is the zeroth order density-density response function (also known as the Linhard function) defined as [191]

$$\chi_{nn}^0(q) = \sum_{ab} \int \frac{d\mathbf{k}}{(2\pi)^2} |\langle a\mathbf{k}|b\mathbf{k}\rangle|^2 \frac{f_{a,\mathbf{k}} - f_{b,\mathbf{k}+\mathbf{q}}}{\epsilon_{a,\mathbf{k}} - \epsilon_{b,\mathbf{k}+\mathbf{q}} + i0^+} , \qquad (5.12)$$

where $f_{a,\mathbf{k}}$ corresponds to the Fermi distribution function. In the low wavelength limit and at $T = 0$, the Linhard function can be approximated as

$$\chi_{nn}^0(\mathbf{q} \to 0) \approx -\nu(E_F) + \sum_{a \neq b} \int \frac{d\mathbf{k}}{(2\pi)^2} |\langle a\mathbf{k}|b\mathbf{k}\rangle|^2 \frac{\Theta(E_F - \epsilon_{a,\mathbf{k}}) - \Theta(E_F - \epsilon_{b,\mathbf{k}})}{\epsilon_{a,\mathbf{k}} - \epsilon_{b,\mathbf{k}} + i0^+} ,$$

$$(5.13)$$

where $\nu(E_F)$ corresponds to the density of states (DOS) at the Fermi level. As a first-order approximation we ignore the inter-band contribution such that $\chi_{nn}^0 \approx \nu(E_F)$.

A quantity related to the single particle lifetime is the transport time, given to

leading order by

$$\frac{\hbar}{\tau_a} = 2\pi \sum_{a'\mathbf{k}'} n_{imp} \left| \frac{v(q)}{\epsilon(q)} \right|^2 |\langle a'\mathbf{k}'|a\mathbf{k}\rangle|^2 \delta(\epsilon_{a,\mathbf{k}} - \epsilon_{a',\mathbf{k}'}) \times (1 - \hat{\mathbf{k}} \cdot \hat{\mathbf{k}}') . \qquad (5.14)$$

In Figs. (5.5) we plot the average single particle lifetime, and average transport time for the cases of TI (black dashed line), TI|SLG (blue dotted line), and TI|BLG (red solid line). The average is defined as

$$\langle \tau_0 \rangle = \frac{\sum_{\mathbf{k}a} \tau_{0a}(\mathbf{k}) \delta(E_F - \epsilon_{\mathbf{k}a})}{\sum_{\mathbf{k}a} \delta(E_F - \epsilon_{\mathbf{k}a})} , \qquad (5.15)$$

We observe that on average the TI|BLG heterostructure presents the largest single-particle lifetime, followed by the TI|SLG, and finally by the TI, as we were expecting.

Fig. (5.5a) shows the average lifetime as a function of the Fermi energy for the TI surface states (dashed line), TI|SLG (dotted line), and TI|BLG (solid line) heterostructures. The larger DOS in the heterostructure provides better screening of the charged impurities, leading to a narrower spectral broadening, which in turn enables larger responses compared with the TI alone. Fig. (5.5b) shows average transport time as a function of the Fermi energy. This quantity is associated with the electronic mobility of the system and is a measure of the ease with which current can be driven through the system. The result for the TI diverges as $E_F \to 0$ because the carrier density goes to zero at the Dirac point.

Now we proceed to evaluate the non-equilibrium current-induced response function (5.10), evaluating separately inter- and intra-band contributions. Although products of Green's functions of the type $G^R G^R$ and $G^A G^A$ are small compared with those of $G^R G^A$ type, we retain them in the numerical evaluation of the response since they cancel unphysical logarithmic divergences from high energy states
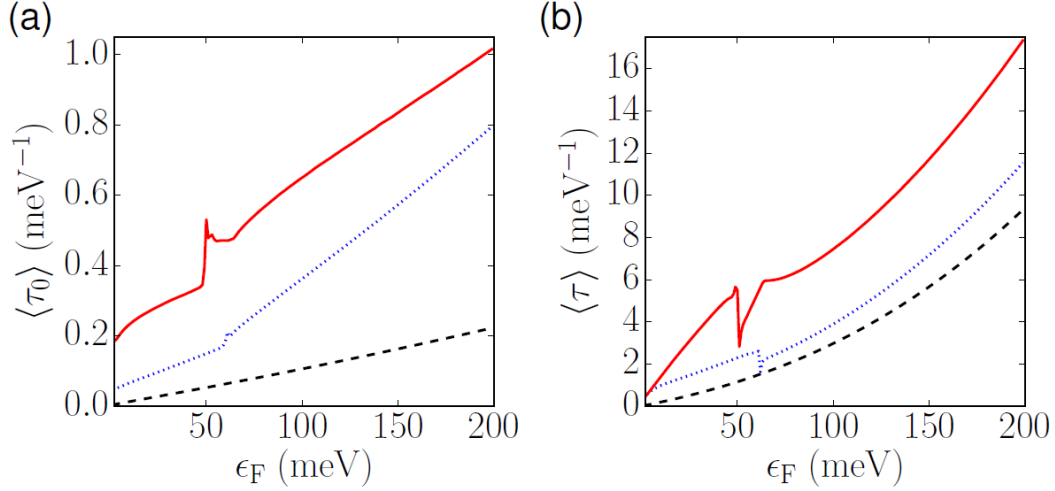
FIG. 5.5: (a) Averaged single particle lifetime, and (b) transport time as a function of the Fermi energy for TI (dashed line), TI|SLG (dotted line), and TI|BLG (solid line) with tunneling amplitude $t = 45$ meV, and chemical potentials $\mu_{TI} = \mu_g = 0$ meV. The impurity density is $n_{imp} = 1 \times 10^{12}$ cm^{-2}.

[192]. Fig.(5.6a) shows the intra-band contribution to the spin accumulation in the x-direction as a response to a current applied in the y-direction, χ^{xy}. The solid line corresponds to the TI|BLG heterostructure, the dotted line to TI|SLG, and the dashed line to the TI surface states. The presence of a graphenic layer not only does not destroy the original TI response but enhances it in some regimes due to a larger DOS and consequently smaller spectral broadening present in combined TI-graphene systems compared with TI alone. A resonance in the TI|BLG response is obtained at the same energy ($E_F \approx 50$ meV, for $t = 45$ meV) where the minimum of the Rashba split bands is located, as shown in Fig.(5.2b). For $E_F \gtrsim 50$ meV, a competition between the Rashba-type contribution and the TI-type contribution causes the TI|BLG response to fall below the TI response. This effect is not observed in the TI|SLG system due to a weaker Rashba splitting [180]. For $E_F \lesssim 100$ meV TI|BLG presents the largest response among the three systems, while TI|SLG dominates for $E_F \gtrsim 100$ meV. The interband contribution is shown in Fig.(5.6b). For the three

120

systems considered, the interband contribution is much smaller than the intraband contribution, and they become comparable only for $E_F \to 0$ meV. For the TI case, $\chi_{inter}^{xy}(E_F = 0) = \chi_{intra}^{xy}(E_F = 0)$. Given that the intraband contributions are much
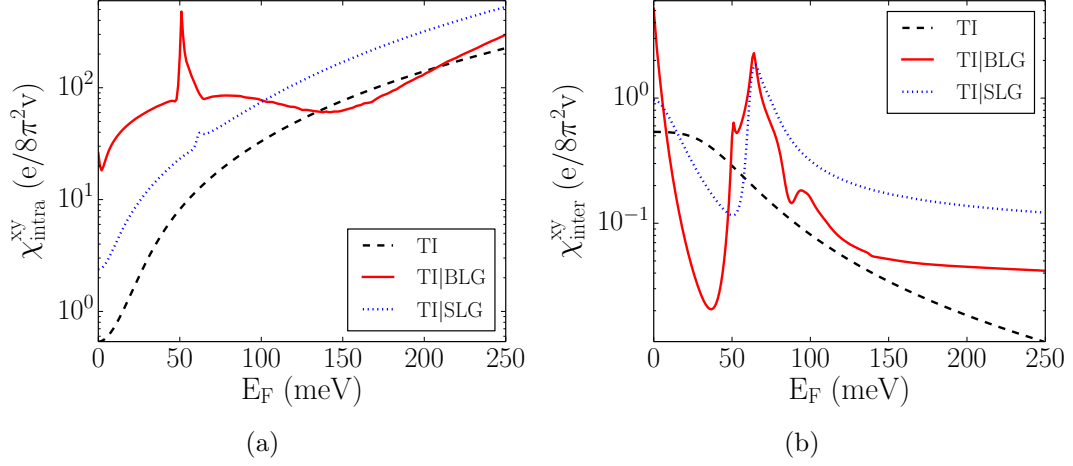
FIG. 5.6: Non-equilibrium current-induced spin density response function χ^{xy} as a function of the Fermi energy. Fig. (a) shows the intraband contribution χ_{intra}^{xy} for TI|BLG (solid line), TI|SLG (dotted line), and TI (dashed line). Fig. (b) shows the interband contribution χ_{inter}^{xy}. Intraband transitions constitute the dominant contribution to the spin response.

larger than the interband contributions from now on only the intraband contributions will be considered. We also will neglect $G^R G^R$- and $G^A G^A$-type contributions since they are systematically smaller than the $G^R G^A$ type. When neglecting these contributions, a momentum cut-off is introduced, $k_{max} = 1\text{nm}^{-1}$. Under these approximations, the band-diagonal, AR-type dressed velocity operator $\tilde{v}_{aa}^i(\mathbf{k})$ is shown diagrammatically in Fig.(5.4d). The corresponding Dyson equation is given by

$$\tilde{v}_{aa}^i(\mathbf{k}) = v_{aa}^i(\mathbf{k}) + \sum_{a'\mathbf{k}'} n_{imp} \left| \frac{v(q)}{\epsilon(q)} \right|^2 |\langle a'\mathbf{k}'|a\mathbf{k}\rangle|^2 G_{\mathbf{k}'a'}^A G_{\mathbf{k}'a'}^R \tilde{v}_{a'a'}^i(\mathbf{k}') , \qquad (5.16)$$

with solution $\tilde{v}_{aa}^i(\mathbf{k}) = \tau_a/\tau_{0a} v_{aa}^i(\mathbf{k})$ [193]. The current-induced spin density is then

approximated as shown diagrammatically in Fig.(5.4c),

$$\chi^{xy} \approx \frac{e}{2\pi V} \operatorname{Re} \sum_{\mathbf{k},a} s_{aa}^x(\mathbf{k}) \tilde{v}_{aa}^y(\mathbf{k}) G_{\mathbf{k}a}^A G_{\mathbf{k}a}^R . \tag{5.17}$$

Fig. (5.7a) shows the current-induced spin density response function χ^{xy} including

(a) $\Delta = 0$meV
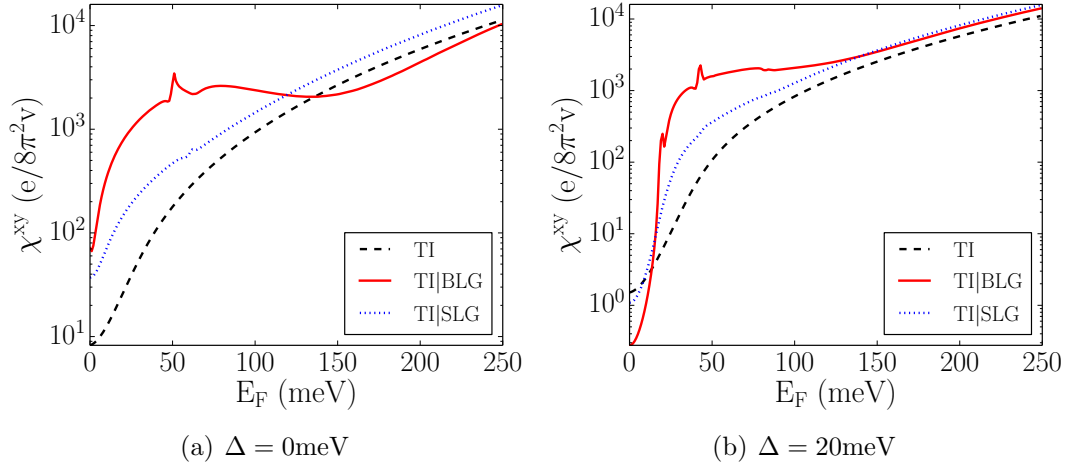
(b) $\Delta = 20$meV

FIG. 5.7: Non-equilibrium current-induced spin response function χ^{xy} as a function of the Fermi energy E_F for TIs (dashed lines), TI|SLG|FM (dotted lines), and TI|BLG|FM (solid lines) with $t = 45$ meV, and TI|FM. (a) shows the case $\Delta = 0$ meV, and (b) case $\Delta = 20$ meV, both for $\delta\mu = 0$ meV. The vertical thin line is located at $E_F = \Delta$. This results include band-diagonal, AR-type vertex corrections to the velocity matrix elements.

band-diagonal, AR-type vertex corrections for TI (black dashed line), TI|SLG (blue dotted line), and TI|BLG (red solid line) for a tunneling amplitude $t = 45$ meV, and $\delta_\mu \equiv \mu_{TI} - \mu_g = 0$ meV. The TI|SLG presents a larger spin-density response than the TI by itself for all the Fermi energies considered. TI|BLG presents an even larger response for $E_F \leq 100$ meV. For higher Fermi energies, the large Rashba splitting induced by the proximity with the TI causes the response to fall below the TI response. Also, a peak in the response is obtained at the bottom of the Rashba

split bands, where the density of states has a peak as well. Fig. (5.7b) shows the response of TI|BLG|FM, TI|SLG|FM, and TI|FM for a FM with out-of-plane magnetization and $\Delta = 20$ meV.

As we discussed before, the TI|FM presents a non-zero χ^{yy} component which is much smaller than the χ^{xy} component. For TI|SLG|FM systems, a χ^{yy} response is also present. A careful calculation of the χ^{yy} component requires taking into account off-diagonal vertex corrections to the velocity operator [194]. A recent work [195] pointed out that double-crossing diagrams give rise to contributions of the same order as the non-crossing diagrams, which makes this calculation very challenging. Vertex corrections are expected to mix the χ^{yy} and χ^{xy} components, but because χ^{yy} is much smaller than χ^{xy} in the regime considered ($E_F \gg \gamma$), we will focus only on the dominant contribution.

In the DC limit achieved by letting $\mathbf{q} \to 0$ first, and then $\omega \to 0$ the conductivity is given by

$$\sigma^{yy} \approx \frac{e^2}{2\pi V} \operatorname{Re} \sum_{\mathbf{k},a} v_{aa}^y(\mathbf{k}) \tilde{v}_{aa}^y(\mathbf{k}) G_{\mathbf{k}a}^A G_{\mathbf{k}a}^R \ . \tag{5.18}$$

This conductivity is calculated in the same way as the current induced spin density response function, to obtain a consistent result. Numerical evaluation of Eq. 5.18 leads to the results shown in Fig. (5.8). Panel (5.8a) shows the conductivity for TI, TI|SLG, and TI|BLG as a function of the Fermi energy. The TI|BLG system shows the highest conductivity among the three systems considered. Panel (5.8c) shows the efficiency for the spin accumulation creation which is the product of the current-induced spin density and the conductivity, as a function of the Fermi energy. The TI|BLG is the system with the most efficient response, despite the fact that the spin density is affected by the development of the Rashba split bands.
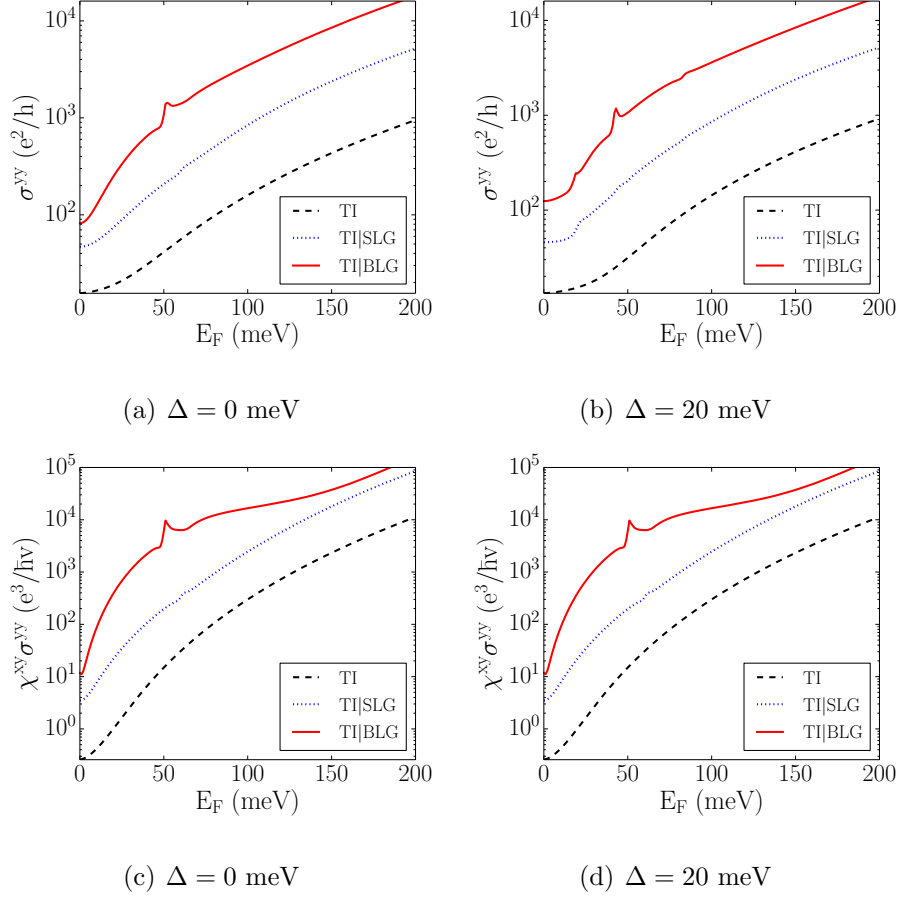
FIG. 5.8: (a) Conductivity σ^{yy} as a function of the Fermi energy E_F for a TI|FM (black dashed lines), TI|SLG|FM (blue dotted lines), and TI|BLG|FM (red solid lines). The tunneling in the heterostructures is $t = 45$ meV, and no coupling to the FM. (b) shows the corresponding case for an exchange coupling $\Delta = 20$ meV. Panles (c), and (d) show the efficiency of the creation of the spin accumulation. TI|BLG clearly shows to be the most efficient heterostructure.

As we have discussed, the presence of the impurities might shift the relative location of the TI and SLG Dirac points (or quadratic band crossing point for the case of BLG). This difference is given by $\delta\mu = \mu_{TI} - \mu_g$. Although experiments have shown the possibility to tune the Fermi level by different techniques [187], it is still interesting to study the spin response as a a function of the mismatch $\delta\mu$. Fig. (5.9) shows a color plot of the ratio between the spin density response function

in TI|BLG and TI alone, $\chi^{xy}/(\chi^{xy})_{TI}$, as a function of the Fermi energy and the relative difference $\delta\mu$. Larger values of $\delta\mu$ lead to larger spin responses due to a reduction of the induced Rashba splitting of the electron bands. On the other hand, the hole bands experience an increase of the Rashba splitting.
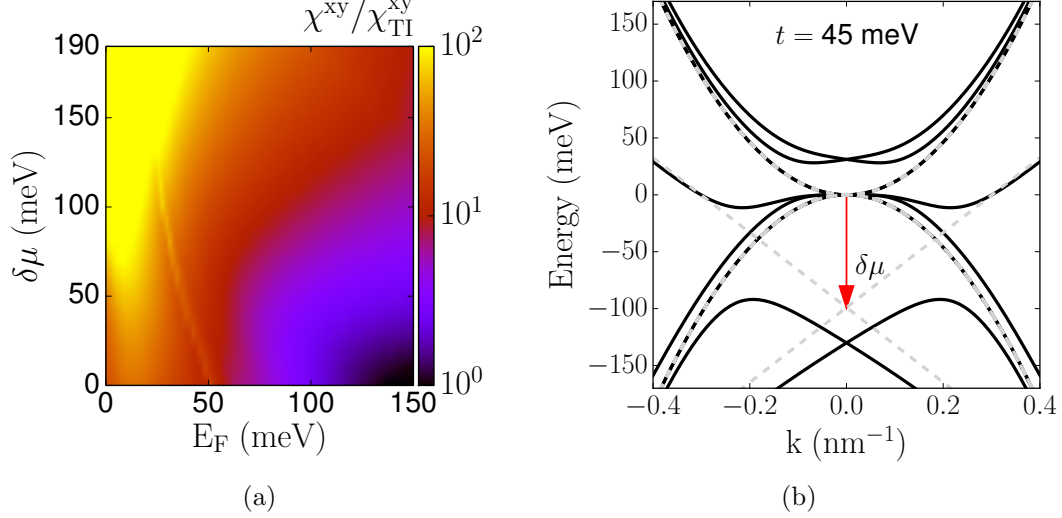
FIG. 5.9: (a) Current-induced spin density response function for a TI|BLG heterostructure normalized to the TI response, χ^{xy}/χ_{TI}^{xy}, as a function of the Fermi energy and $\delta\mu = \mu_{TI} - \mu_g$. (b) Band structure for a TI|BLG heterostructure with Dirac point mismatch $\delta\mu = 100$ meV. The solid lines correspond to the TI and BLG bands. Dashed lines correspond the TI|BLG hybridized bands with $t = 45$ meV.

5.3   Random tunneling regime

Recent experiments on the fabrication of TI|BLG heterostructures [32] suggest that roughness at the interface of the 3DTI and graphene might lead to random tunneling processes, instead of coherent tunneling. In this section we study the inverse spin galvanic effect in weakly coupled systems dominated by random tunneling processes. In the case of graphene, the low-energy states are located around the K point, while the TI low-energy states lie around the Γ point. This momentum

mismatch leads to a vanishing induced spin accumulation on graphene. However, it is interesting to study the case of systems which low-energy states lie around the Γ point. Specifically, we consider a two-dimensional relativistic electron gas (2DREG) with low energy states around the Γ point, in the proximity of a three-dimensional topological insulator (TI). The Hamiltonian for the 2DREG is given by $H_g(\mathbf{k}) = \hbar v_g k \sigma_0$, where σ_0 is the identity in spin space. The Hamiltonian for the TI is given by $H_{TI} = \hbar v_{TI} (k_y \sigma_x - k_x \sigma_y)$. Short-range, spin independent, uncorrelated disorder $V(\mathbf{r}) = V_0 \delta(\mathbf{r})$ is also assumed for TI and 2DREG. We assume that tunneling events conserve neither spin nor momentum. The response function is calculated in the diffusive regime, following Ref. [193]. The current-induced spin density, in the diffuson language, is shown diagrammatically in Fig.(5.10a). Explicitly, it can be written as

$$\chi^{ij} = \frac{\hbar}{2\pi} \operatorname{Re} \operatorname{Tr} \{ \hat{s}^i G^R \hat{j}^j G^A \} + \frac{\hbar}{2\pi} \operatorname{Re} \operatorname{Tr} \{ \hat{s}^i G^R G^A D G^R G^A \hat{j}^j \} , \qquad (5.19)$$

where $\hat{j}^j = ev^j$ is the current operator and the trace is taken over spin, and momentum. D corresponds to the 2DREG diffuson induced by impurity scattering and tunneling to the TI. Fig. (5.10c) shows diagrammatically the equation for the disorder-induced diffuson which it is given by the ladder sum.

Fig. (5.10d) shows an approximation to the tunneling and disorder induced 2DREG diffuson D in the limit where the tunneling time τ_t is much larger than the scattering time τ_0.

The self-energy, shown diagrammatically in Fig. (5.10b), has two contributions, Σ_0 and Σ_t. The first contribution, Σ_0, is induced by disorder on 2DREG, and is given by

$$\Sigma_{dis} = -i u_0^g \nu_g \pi \sigma_0 , \qquad (5.20)$$
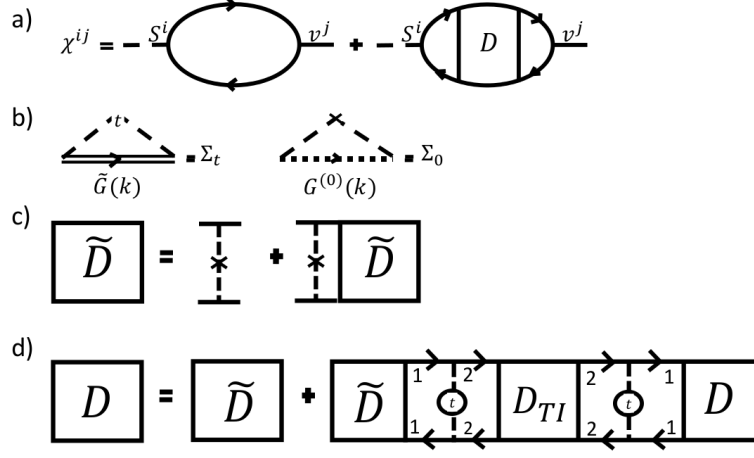
FIG. 5.10: Feynman diagrams for (a) the current-induced spin density in the diffuson language, (b) the tunneling and disorder induced self-energies for 2DREG in the proximity of a TI, (c) the disorder-induced 2DREG diffuson, and (d) the tunneling-dressed 2DREG diffuson in the limit $\tau_t \gg \tau_0$.

where ν_g corresponds to the density of states in 2DREG at the Fermi level, and $u_0^g = n_{imp}V_0^2$ corresponds to the product of the impurity density n_{imp} and the strength of the disorder potential V_0 on the 2DREG. The second contribution, Σ_t, is induced by tunneling to the TI. This self-energy has an imaginary part that corresponds to an extra spectral broadening and a real part that is the one responsible for inducing spin-orbit coupling on 2DREG

$$\Sigma_t = -i2\pi^2(\hbar v_{TI})^2 \nu_{TI}\hat{t}^2\sigma_0 + \hat{t}^2\hbar v_{TI}(\mathbf{k}\times\vec{\sigma})_z \ , \tag{5.21}$$

where the normalized tunneling amplitude $\hat{t}^2$ is defined as $\hat{t}^2 = t^2/(4\pi(\hbar v_{TI})^2)$, ν_{TI} corresponds to the TI density of states at the Fermi level, and v_{TI} corresponds to the Fermi velocity. In order to correctly derive the real part we have to introduce a momentum cutoff in the tunneling amplitude. To induce this self-energy, is crucial that the low-energy states of both the 2DREG and the TI lie around the Γ point.

The disorder- and tunneling-dressed 2DREG Green's function is then given by

$$G^{R/A} = \frac{(\epsilon_{R/A} - \epsilon_{\mathbf{k}})\sigma_0 + \hat{t}^2 \hbar v_{TI} \left(-k_y \sigma_x, k_x \sigma_y\right)}{(\epsilon_{R/A} - \epsilon_{\mathbf{k}})^2 - \hat{t}^4 (\hbar v_{TI})^2 k^2} , \qquad (5.22)$$

where $\epsilon_{R/A} = \epsilon + i\tilde{\gamma}_1$, with $\tilde{\gamma}_1 = \gamma_{10} + \gamma_{1t} = u_0^g \nu_g \pi + t^2 \nu_{TI} \pi/2$. With these results, we can calculate the contribution to the current-induced spin density of the first diagram in Fig.(5.10a). It is given by

$$(\chi^{xy})_1 \approx \frac{\hbar^2 e v_{TI}}{4\pi u_g} \hat{t}^2 + O(\hat{t}^4). \qquad (5.23)$$

Now calculate the vertex correction in the diffuson language. The equation for the disorder induced 2DREG diffuson is shown in Fig.(5.10c) and explicitly is given by

$$\tilde{D}(\mathbf{q}) = (\sigma_0 \otimes \sigma_0 - P_g(\mathbf{q}))^{-1} u_0^g \sigma_0 \otimes \sigma_0 , \qquad (5.24)$$

where the 2DREG quantum probability $P_g(\mathbf{q}, \omega)$ is given by

$$P_g(\mathbf{q}, \omega) = u_g \int \frac{d^2\mathbf{k}}{(2\pi)^2} G_{\epsilon_F}^R(\mathbf{k}) \otimes G_{\epsilon_F - \omega}^A(\mathbf{k} - \mathbf{q}) \approx (1 - \tau_{0g} D_g q^2 + i\omega\tau_{0g} - \tau_{0g}/\tau_{tg})\sigma_0 \otimes \sigma_0 ,$$
$$(5.25)$$

in the diffusion limit ($\omega\tau_{0g} \ll 1$ and $v_g \tau_{0g} q \ll 1$). Also $E_F/\tilde{\gamma}_1 \gg 1$, and $\tau_{0g}/\tau_{tg} \ll 1$. $D_g = \tau_{0g} v_g^2/2$ corresponds to the 2DREG diffusion constant. Then, the disorder-dressed 2DREG diffuson is simply given by

$$\tilde{D}(\mathbf{q}, \omega) = \frac{u_0^g}{\tau_{0g}} \frac{1}{D_g q^2 - i\omega + \frac{1}{\tau_{tg}}} \sigma_0 \otimes \sigma_0 . \qquad (5.26)$$

The TI diffuson is obtained by solving a Dyson equation equivalent to the 2DREG

diffuson, and shown in Fig.(5.10c). The TI quantum diffusion probability $P_{TI}(\mathbf{q}, \omega)$ is given by

$$P_{TI}(\mathbf{q}, \omega) = u_{TI} \int \frac{d^2\mathbf{k}}{(2\pi)^2} G^R_{TI\epsilon_F}(\mathbf{k}) \otimes G^A_{TI\epsilon_F - \omega}(\mathbf{k} - \mathbf{q}) \tag{5.27}$$

$$= a(\mathbf{q}, \omega)\sigma_0 \otimes \sigma_0 + b_a(\mathbf{q}) (\sigma_0 \otimes \sigma^a + \sigma^a \otimes \sigma_0) + d_{ab}(\mathbf{q}, \omega)\sigma^a \otimes \sigma^b ,$$

where the coefficients are given by

$$a(\mathbf{q}, \omega) = 1/2(1 - \tau_{0TI} D_{TI} q^2 + i\omega\tau_{0TI} - \tau_{0TI}/\tau_{tTI}),$$

$$b_1(\mathbf{q}) = -i(1 - \tau_{0TI}/\tau_{tTI})q_y \tau_{0TI} v_{TI}/4,$$

$$b_2(\mathbf{q}) = i(1 - \tau_{0TI}/\tau_{tTI})q_x \tau_{0TI} v_{TI}/4,$$

$$d_{11}(\mathbf{q}, \omega) = 1/4(1 - \tau_{0TI} D/2(q_x^2 + 3q_y^2) + i\omega\tau_{0TI} - \tau_{0TI}/\tau_{tTI}),$$

$$d_{22}(\mathbf{q}, \omega) = 1/4(1 - \tau_{0TI} D/2(3q_x^2 + q_y^2) + i\omega\tau_{0TI} - \tau_{0TI}/\tau_{tTI}),$$

$$d_{12} = d_{21} = 1/4(1 - \tau_{0TI}/\tau_{tTI})\tau_{0TI} D q_x q_y,$$

where $D_{TI} = \tau_{0TI} v_{TI}^2/2$ is the TI diffusion constant, and $\tau_{0TI}/\tau_{tTI} \ll 1$. Then the TI diffuson is given by

$$D_{TI}(\mathbf{q}, \omega) = (\sigma_0 \otimes \sigma 0 - P_{TI}(\mathbf{q}, \omega))^{-1} u_{TI} . \tag{5.28}$$

Explicitly we have

$$D_{TI}(\mathbf{q}, \omega) = u_{TI} \begin{pmatrix} A & 0 & 0 & B \\ 0 & \frac{1}{2} + C & -\frac{1}{2} + C & 0 \\ 0 & -\frac{1}{2} + C & \frac{1}{2} + C & 0 \\ B & 0 & 0 & A \end{pmatrix} \tag{5.29}$$

where

$$A = \frac{-8 + 4i\omega\tau_{0TI}}{(\tau_{0TI}D_{TI}q^2)^2 + (\omega\tau_{0TI} + 2i)^2} \tag{5.30}$$

$$B = -\frac{i\tau_{0TI}D_{TI}q^2}{\omega\tau_{0TI} + i} \tag{5.31}$$

$$C = \frac{1}{4\tau_{0TI}D_{TI}q^2 - i\omega\tau_{0TI}}. \tag{5.32}$$

Following Ref. [196], we transform the quantum probability P_{TI} to the more physical charge-spin representation of the diffuson using the identity $1/2\sigma^\alpha_{s1s2}\sigma^\alpha_{s2s1}$, $s_1, s_2 = 1, 2$ and $\alpha = 0, x, y$. The inverse diffuson $D(\mathbf{q}, \omega)^{-1}_{TI\alpha\beta}$ gives the equations that describe the coupled charge-spin transport on the TI surface [196]

$$\frac{\partial n}{\partial t} = D_{TI}\nabla^2 n + 2\sqrt{D_{TI}/2\tau_{0TI}}(\hat{z} \times \nabla) \cdot \vec{S} \tag{5.33}$$

$$\frac{\partial S^x}{\partial t} = \frac{D_{TI}}{2}\frac{\partial^2 S^x}{\partial x^2} + \frac{3D_{TI}}{2}\frac{\partial^2 S^x}{\partial y^2} - D_{TI}\frac{\partial^2 S^y}{\partial x\partial y} - \frac{S^x}{\tau_{0TI}} + \sqrt{D_{TI}/2\tau_{0TI}}(\hat{z} \times \nabla)_x n$$

$$\tag{5.34}$$

$$\frac{\partial S^y}{\partial t} = \frac{D_{TI}}{2}\frac{\partial^2 S^y}{\partial x^2} + \frac{3D_{TI}}{2}\frac{\partial^2 S^y}{\partial y^2} - D_{TI}\frac{\partial^2 S^x}{\partial x\partial y} - \frac{S^y}{\tau_{0TI}} + \sqrt{D_{TI}/2\tau_{0TI}}(\hat{z} \times \nabla)_y n$$

$$\tag{5.35}$$

where $\vec{S}$ corresponds to the non-equilibrium spin density, and n is the charge density.

The fully-dressed 2DREG diffuson is calculated in the limit $\tau_0/\tau_t \ll 1$ in the charge-spin representation. The corresponding equation is shown diagrammatically in Fig.(5.10d). Explicitly, it is given by

$$D = \tilde{D} + \tilde{D}\left(\frac{P_1}{u_g^g}\right)T^2\left(\frac{P_2}{u_0^{TI}}\right)D_{TI}\left(\frac{P_2}{u_0^{TI}}\right)T^2\left(\frac{P_1}{u_g^g}\right)D$$

where the tunneling matrix elements are given by $T^2_{\alpha\beta} = t^2\delta_{\alpha\beta}$. To leading order

130

in the tunneling amplitude, and in the diffusive limit, the fully-dressed 2DREG diffuson is given by

$$
D = \frac{u_0^g}{\tau_{0g}/\tau_{tg}} \begin{pmatrix} 1 - i\frac{\tau_{0TI}/\tau_{tTI}}{\omega\tau_{0TI}} & & \\ & 1 + \frac{\tau_{0TI}/\tau_{tTI}(1-i\omega\tau_{0TI})}{2(1+\omega^2\tau_{0TI}^2)} & \\ & & 1 + \frac{\tau_{0TI}/\tau_{tTI}(1-i\omega\tau_{0TI})}{2(1+\omega^2\tau_{0TI}^2)} \end{pmatrix} . \quad (5.36)
$$

Now we are ready to calculate the contribution from the second diagram in Fig. (5.10a). The dominant contribution to the spin density accumulation response function is

$$
(\chi^{xy})_2 \approx \frac{e}{8\pi^2 v_{TI}} \frac{\nu_g}{\nu_{TI}} + O(\hat{t}^2) . \quad (5.37)
$$

Thus, to leading order the current-induced spin accumulation for a 2DREG in the proximity of a TI is tunneling independent. This is the result of a competition between the fact that as we increase the tunneling amplitude we lose more quasi-particles to the TI, but at the same time, we obtain larger spin-orbit coupling.

5.4   Conclusions

We have proposed the use of topological insulator-graphene-FM vertical heterostructures as systems with very efficient spin accumulation creation for spintronic applications. We have studied the non-equilibrium current-induced spin accumulation and transport in the DC limit in Dirac heterostructures with spin-orbit coupling. We have considered the effect of disorder induced by charged impurities in these systems.

Also, we considered two limiting tunneling regimes: a coherent tunneling regime and a random tunneling regime. In the coherent tunneling regime, after carefully

taking into account vertex corrections, we have shown that the presence of graphene or bilayer graphene significantly increases the efficiency of the spin accumulation creation, due to the higher mobility of the graphene layers and consequently a better screening of the charged impurities. We have compared the efficiency of the spin density accumulation creation in three different systems: TI, TI|SLG, and TI|BLG, and it was shown that the TI|BLG heterostructure offers the most efficient creation of spin accumulations. In the random tunneling regime, we have calculated the current-induced spin accumulation in the diffusive regime for a 2DRGE in the proximity of a TI. We have shown that in the limit considered, a tunneling-amplitude-independent spin accumulation is induced on he 2DRGE.

CHAPTER 6

Effect of inhomogeneities on the dynamics of the metal-insulator transition in VO2

6.1   Introduction

This chapter is based on the work that can be found in Ref. [33]. The author of this dissertation carried out the theoretical calculations. The experimental component of this work was performed by E. Radue and M. Simons.

Vanadium dioxide (VO_2) undergoes a metal-insulator transition (MIT) around room temperature [197] enabling a wide range of potential applications. It has recently been shown that it is possible to photo-induce the insulator-to-metal transition in VO_2 in the sub-picosecond timescale [198–204]. This finding makes VO_2 a material of great interest for electronic and photonic applications, such as ultra-fast switches or transistors. The realization of VO_2-based switches requires the ability

to control the VO$_2$ MIT dynamics using external fields, as well as a better understanding of the recovery mechanisms after the external field is turned off and the material returns to its normal state. The mechanism by which the photo-induced insulator-to-metal transition takes place in VO$_2$ is still not fully understood due to the complexity of the electronic behavior of VO$_2$ arising from the presence of strong electron-lattice coupling and electron-electron interactions [205–208]. As a result, VO$_2$ is a unique material of great fundamental and practical interest.

At low temperatures ($T \lesssim 340$ K) the VO$_2$ lattice has a monoclinic structure, whereas at high temperatures ($T \gtrsim 340$ K) it has a tetragonal structure. This difference in lattice structure is reflected in the band structure: VO$_2$ is an insulator in the monoclinic phase and a metal in the tetragonal phase. This simple picture is complicated by the fact that in VO$_2$ electron-electron correlations are very strong and can provide an important contribution to the localization of the electronic states via the Mott mechanism [206, 207, 209, 210]. It appears that a full account of the MIT must take into account the interplay of the lattice dynamics and the electron dynamics driven by strong electron-electron interactions. This is a fascinating and extremely challenging problem that in addition is complicated by the unavoidable presence of inhomogeneities [211, 212].

Several works [202, 213–221] have investigated the short timescale dynamics after the photo-induced transition. In particular, Ref. [222] presented a comparison of the long timescale recovery dynamics between VO$_2$ films on a crystal substrate or a glass substrate and found that the recovery time for the films on the glass substrate was much longer than for the films on a crystal substrate. The recovery time was modeled using the heat equation to describe the heat flow across the interface between the VO$_2$ film and the substrate. The difference in the characteristic time between the two types of substrates was attributed to the fact that the thermal

conductivity of the interface was expected to be much smaller for glass substrates than for crystal substrates.

In this work we present a theory to properly take into account the effect of inhomogeneities on the recovery dynamics of VO_2 films. Our theory describes simultaneously: (i) the profile of the reflectivity across a thermal induced MIT; (ii) the long timescale recovery dynamics of the reflectivity after a photo-induced insulator-to-metal transition; (iii) the observed difference of two orders of magnitude between samples with different substrates. Inhomogeneities are due to the fact that the film is comprised of grains with different sizes and different local properties, such as strain [223, 224] and chemical composition.

The presence of inhomogeneities induces a distribution of values for the transition temperature T_c within the film. To take this into account we derive a generalized heat equation that includes the fact that during the recovery from the photo-induced insulator-to-metal transition, at any given time a fraction of the sample is undergoing the metal-to-insulator transition, another fraction is still cooling in the metallic phase, and another fraction is already cooling in the insulating phase. A key ingredient of the generalized heat equation is the correct description of the time evolution of the fraction of the sample that is metallic, insulating, or undergoing the phase transition. We then use our theoretical model to obtain the scaling relation between the characteristic recovery time τ and the parameters of the films. Our theoretical model, and the underlying assumptions, are strongly supported by our experimental results. Differently than in Ref. [222] our VO_2 films have all crystal substrates, no glass. Yet, we find that τ can be more than two orders of magnitude different depending on the crystal substrate, TiO_2 or Al_2O_3, Fig. 6.1.

The generalized heat equation, Eqs. (6.9), which properly takes into account the effect of the films inhomogeneities on the recovery dynamics is the main result of our

work. Our theory allows the description of the recovery dynamics consistently with the measurements obtained for the thermally driven MIT. The scaling between the characteristic recovery time τ and the parameters of the film is another important result of our work.
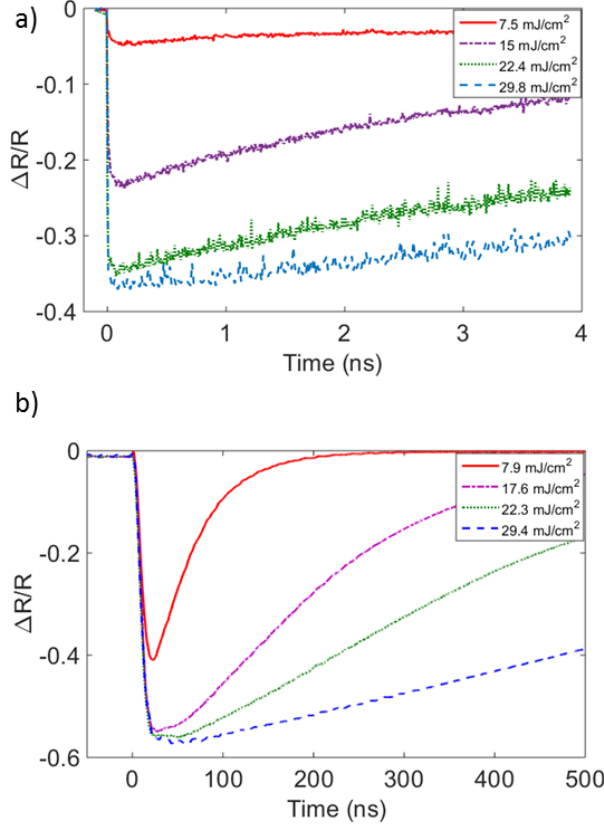
FIG. 6.1: Relative change in reflectivity ($\Delta R/R$) for the VO$_2$ film on (a) Al$_2$O$_3$ substrate and (b) TiO$_2$ substrate as a function of time after the MIT is induced at time $t = 0$ by a strong ultrafast pump pulse. The values of the pump fluence are shown in the legend, and the sample temperature is set to 311 K in (a) and 280 K in (b), which correspond to approximately 30 K below the critical temperature T_c for thermally-induced MIT for each sample.

Our work is relevant to the more general problem of how spatial inhomogeneities affect a first order phase transition. The ability of our treatment to contribute to this general problem relies on the fact that in VO$_2$ the two phases across the

first-order phase transition have very different electronic properties (metallic vs. insulating behavior) that allows us to get an accurate phase mapping, via optical reflectivity measurement, of the time evolution of the metallic (insulating) fraction and, indirectly, of the spatial inhomogeneities present during the transition.

The work is organized as follows. Sec. 6.2 describes the experimental arrangements to measure the optical reflectivity time-evolution. The details of the theoretical model that we use to characterize the distribution of the films' inhomogeneities and the long-time dynamics of the reflectivity after a photo-induced insulator-to-metal transition are presented in Secs. 6.3 and 6.4, respectively. In Sec. 6.5 we demonstrate how the variations in statistical properties of the two films result in a significant difference in the relaxation timescales, and in Sec. 6.6 we provide our conclusions.

6.2 Experimental setup

In our experiments we studied two VO_2 thin-film samples, both of which were produced using reactive-bias target ion beam deposition (RBTIBD) [225]. One sample was grown on 0.5 mm thick c-Al_2O_3, and the thickness of the VO_2 film was 80 nm. The other sample was grown on a 0.5 mm thick TiO_2 (011) substrate, and was measured to be 110 nm thick. X-ray diffraction (XRD) evaluation of both films showed them to be crystalline, and detailed characterization information is available in previous reports [226, 227].

For the photo-induced insulator-to-metal transition experiments we used an ultrafast laser system (Coherent Mantis oscillator and Legend Elite regenerative amplifier) with approximately 100 fs pulses with a central wavelength at 800 nm and a repetition rate of 1 kHz. The properly attenuated output of the laser was split into
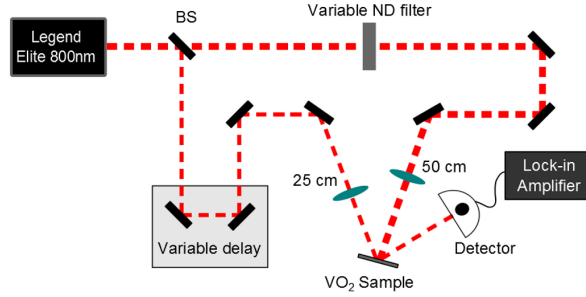
FIG. 6.2: Schematic of the ultrafast pump-probe setup. BS is an 80/20 beam splitter.

strong pump pulses and weaker probe pulses using a beam splitter in a standard pump-probe configuration, shown in Fig. 6.2. The more powerful pump beam, focused to a 180 μm diameter spot on the surface of the sample, was used to induce the insulator-to-metal transition, and its fluence was controlled using a variable neutral-density filter (VF). The fluence of the probe beam was further attenuated to a value well below the insulator-to-metal threshold ($\phi_{\text{probe}} \leq 100~\mu\text{J/cm}^2$), and we used its reflectivity from the sample to monitor the instantaneous optical properties of the VO$_2$ film. The probe pulses were directed along a variable delay stage to accurately control the relative timing between the pump and probe pulses by up to 4 ns with a few fs precision. The probe beam was focused on the sample at the same spot as the pump beam, using a shorter focal length lens. When tuned to the center of the pump beam focal spot, the smaller probe beam diameter (90 μm) ensured probing a region of uniform pump intensity.

The reflected probe power was measured using a silicon photodetector, and further analyzed using a lock-in amplifier. To minimize the effects of probe pulse instabilities, as well as long-terms drifts due to environmental changes, we report the relative change in probe reflection $\Delta R/R$ with the pump beam on or off.

Notably the MIT relaxation of the VO$_2$/TiO$_2$ sample was not measurable with
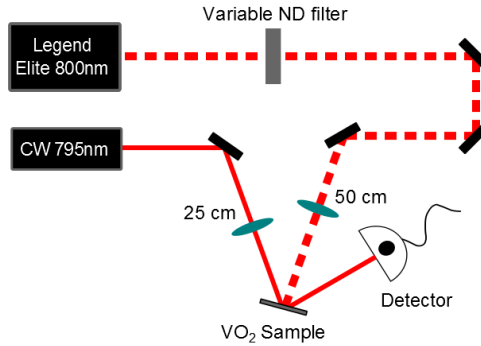
FIG. 6.3: Schematic of the experimental setup using a continuous-wave probe laser.

the femtosecond probe, as its characteristic decay time exceeded the 4 ns maximum pulse separation, determined by the length of the delay stage. To measure the relaxation of the metallic VO_2 grown on the rutile sample we modified our experimental setup by replacing the femtosecond probe pulses with a continuous-wave (CW) diode laser operating at 785 nm and a fast photodiode (measured response time of approximately 10 ns), as shown in Fig. 6.3. This detection method allowed us to measure changes in reflectivity for times longer than $\approx$ 20 ns after the insulator-to-metal transition, that were inaccessible with the femtosecond probe arrangement.
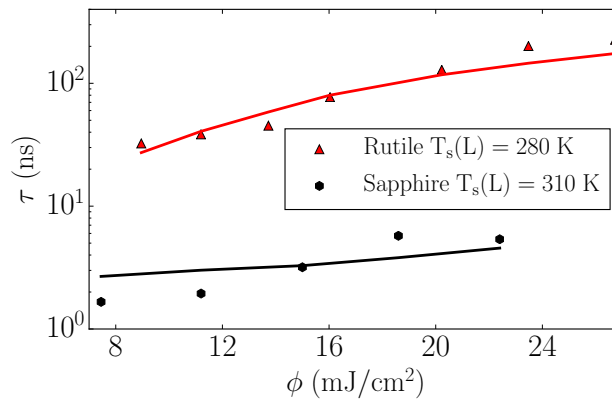
FIG. 6.4: Dependence of metal state decay constant τ on the laser pump fluence and substrate temperature. Dots represent experimental data, and lines corresponds to the results of the theoretical calculations. The initial temperature T_s for both sample substrates was approximately 30 K below their respective MIT critical temperatures.

139

Figure 6.1 shows sample measurements of both the VO_2/Al_2O_3 and VO_2/TiO_2 films, using the femtosecond and CW probe arrangements respectively. The overall reflectivity depends on the refractive index of both the film and the substrate, and the refractive indices of TiO_2 and Al_2O_3 are different. Because it is easier to average the CW laser reflection signal, the curves for VO_2/TiO_2 are smoother than the curves for the VO_2/Al_2O_3. The rutile reflection spectra recorded using the ultrafast probe had the same noise as for the sapphire samples, indicating that the differences in the noise are due to differences in the probes, not in the samples.

For values of the pump fluence higher than a threshold, which depends on the substrate temperature, we can see that the reflectivity, soon after the pump pulse, remains almost constant for some time, i.e. its dynamics exhibits a "flat" region, see in particular Fig. 6.1 (b). The observed "flattening" of the curves is due to the pump pulse heating the sample to a temperature above the threshold value for the thermally-induced insulator-to-metal transition [219, 221]. In this case the reflectivity stays unchanged at the level corresponding to a fully metallic phase until a non-negligible fraction of the sample cools down to the transition temperature. For all experimental curves only the later exponential part of the measured reflectivity was included into the fitting thermal relaxation time analysis.

The analysis of the relative reflectivity for both VO_2 samples demonstrate that after the initial rapid change during the ultra-fast insulator-to-metal transition, its time evolution during the recovery is well fitted by a single exponential function with a recovery time constant τ:

$$R_{\text{fit}}(t) = R_I + (R_0 - R_I)\, e^{-t/\tau}, \tag{6.1}$$

where R_I corresponds to the reflectivity in the insulating phase, and R_0 corresponds

to the reflectivity at $t = 0$ s. The results of such measurements are shown in Fig. 6.4: for VO$_2$/Al$_2$O$_3$ films we obtained values of τ of the order of few nanoseconds, whereas it took the VO$_2$/TiO$_2$ sample a few hundred nanoseconds to relax back to the insulating state. This two orders of magnitude difference in the recovery times was even more surprising considering that the characteristic times for the transition itself were quite similar, as demonstrated in previous studies [221]. In the discussion below we demonstrate that the relaxation dynamics strongly depend on the microstructure of the VO$_2$ films which in turn is strongly influenced by the properties of the substrate and their interface. Figure 6.4 also reveals that the rate of thermal relaxation for both samples increases with higher pump power.

6.3 Theoretical modeling of inhomogeneities

In order to take into account the effect of the inhomogeneities on the MIT dynamics the first step is to characterize them. To do this we can use the profile of the reflectivity across the thermally induced MIT. The dotted lines in Figures 6.5 (a), and (b) show the measured reflectivity as a function of temperature across the thermally induced MIT for a VO$_2$ film grown on sapphire and TiO$_2$, respectively. The temperature driven MIT in VO$_2$ is a first-order transition. In the ideal case the reflectivity is expected to exhibit a finite, step-like, change at the critical temperature T_c, at which the sample goes from a low-temperature insulating state to a high-temperature metallic state. In thin films, however, the optical reflectivity smoothly changes from the value corresponding to the insulating phase (R_I) to the value characteristic to the metallic phase (R_M) as the temperature increases, as Fig. 6.5 illustrates. For our samples the hysteresis loop is very narrow [227]. The fact that the MIT takes place over a range of temperatures implies that different regions of
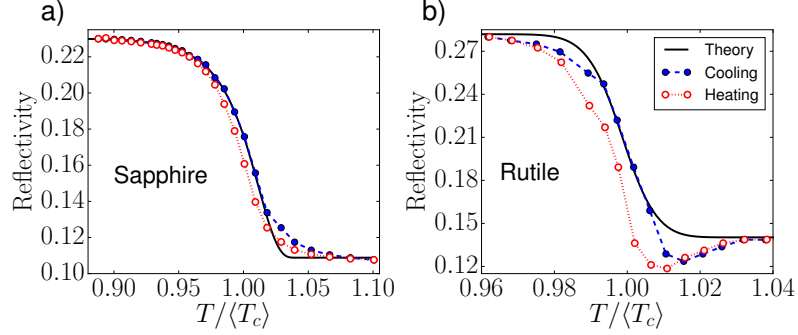
FIG. 6.5: Evolution of the reflectivity across the thermally induced MIT for the case of sapphire and rutile substrates normalized to the average critical transition temperature. The open circles (red) correspond to the measured reflectivity in the heating branch, the solid circles (blue) correspond to the measured reflectivity in the cooling branch, and the solid curve corresponds to the theoretical result. For rutile substrate $\langle T_c \rangle = 314.0$ K, and for the sapphire substrate $\langle T_c \rangle = 340.1$ K.

the sample have different values of T_c. This is different from the case of an ideal, homogeneous, system for which the whole sample exhibits the coexistence of metallic and insulating regions only for $T = T_c$. As a consequence the MIT in the films is characterized not by a single critical temperature but by a distribution $P(T_c)$ of critical temperatures. This is due to the fact that the VO$_2$ films are inhomogeneous: they are formed by crystal grains with different local properties. Different grains in general have different sizes, slightly different stoichiometry, and experience different local strains. It is very challenging to characterize the distribution of all the local properties that can affect the transition temperature of each grain. However, for our purposes, we only need $P(T_c)$ and, as we show below, this can obtained directly from the profiles of $R(T)$ without having to characterize the distribution of the local properties affecting T_c. Let η_I be the fraction of the sample in the insulating phase. At a given temperature T we have:

$$\eta_I(T) = \int_T^\infty P(T_c) dT_c. \tag{6.2}$$

Let $\eta_m(T) = 1 - \eta_I(T)$ be the fraction of the film in the metallic phase. To obtain the evolution of $\eta_I(T)$ across the MIT, and therefore $P(T_c)$, considering that changes in the fraction of the film that is metallic (insulating) are the dominant cause of changes in the reflectivity, we can use a two-fluid effective medium theory (EMT) [111, 228–230]. In the EMT the inhomogeneous system is replaced by an effective homogeneous medium having the same, bulk, electric properties. Let ϵ_M, ϵ_I be the dielectric constants (at the probing frequency) of VO$_2$ in the metallic and insulating phase respectively. Then, the dielectric constant of the effective medium, ϵ_{EMT}, is given by the following equation:

$$\frac{\eta_I(\epsilon_I - \epsilon_{EMT})}{\epsilon_{EMT} + g(\epsilon_I - \epsilon_{EMT})} + \frac{\eta_M(\epsilon_M - \epsilon_{EMT})}{\epsilon_{EMT} + g(\epsilon_M - \epsilon_{EMT})} = 0. \tag{6.3}$$

In Eq. (6.3) g is a factor that depends on the shape of the grain. Without loss of generality we set $g = 1/3$. Let n and k be the real and imaginary parts respectively of the index of refraction, so that for the effective medium $n + ik = \sqrt{\epsilon_{EMT}}$ and therefore

$$R = \left| \frac{\cos\theta_0 - \sqrt{(n+ik)^2 - \sin^2\theta_0}}{\cos\theta_0 + \sqrt{(n+ik)^2 - \sin^2\theta_0}} \right|^2, \tag{6.4}$$

where $\theta_0 \approx 15°$ corresponds to the probe incidence angle. Given our experimental setup we can reliably obtain the imaginary part of the index of refraction by measuring the absorption. For this reason we set the value of the imaginary part of the complex index of refraction k_M, (k_I) for the metallic and (insulating) phase to the measured values, consistent with the values reported in the literature [231, 232], and then use Eq. (6.4) and the measured value of R_M (R_I) in the metallic (insulating) phase to fix the corresponding value of n_M (n_I) (see Table 6.1).

Using Eqs. (6.2)-(6.4) we can obtain the profile of $R(T)$ across the MIT for a

given $P(T_c)$. Assuming $P(T_c)$ to be a Gaussian distribution, by fitting the measured profile of $R(T)$ to the one obtained using Eqs. 6.2-6.4 we can obtain the average value of the critical temperature $\langle T_c \rangle$ and its standard deviation σ_{T_c}. For VO_2/TiO_2 samples we find $\langle T_c \rangle = 314$ K, $\sigma_{T_c} = 2.6$ K, for VO_2/Al_2O_3 samples $\langle T_c \rangle = 340$ K, $\sigma_{T_c} = 8.8$ K. The solid lines in Fig. 6.5 show the profiles of $R(T)$ obtained using Eqs. (6.2)-(6.4) and the above values for $\langle T_c \rangle$ and σ_{T_c}.

The difference in the value of T_c between VO_2/TiO_2 and VO_2/Al_2O_3 samples can be attributed to the fact that TiO_2, having a rutile structure, might induce strains into the VO_2 film that should favor the metallic phase of VO_2. In general, strain effects are expected to play an important role in the physics of the MIT phase transition of VO_2 films. In our approach such effects enter indirectly, via the form of the probability distribution $P(T_c)$, and the value of the thermal conductivity of the interface between the VO_2 film and the substrate.

As we discuss in the following section, for our theoretical treatment of the recovery dynamics over long timescales of VO_2 films the knowledge of $P(T_c)$, i.e., $\langle T_c \rangle$ and σ_{T_c}, is all that is needed. As mentioned before the fact that σ_{T_c} is nonzero is due to inhomogeneities, of different nature, present in the VO_2 film. It is practically impossible to know the distribution in the films of the properties affecting T_c. However, it is interesting to consider the limit in which the grain size D is the dominant property affecting T_c. The reason is that in this limit it is possible to extract, using strong and fundamental arguments, the distribution, $P(D)$, for the grain size. In particular, it is possible to obtain the average grain size, $\langle D \rangle$, and its standard deviation, quantities that are of great practical interest. $\langle D \rangle$ can be compared to estimates obtained using more direct experimental techniques, such as XRD. In the remainder of this section we use the experimental results for $R(T)$ across the MIT to extract $\langle D \rangle$ and its standard deviation.

Theoretical and experimental evidence[233] indicates that for thin films the distribution $P(D)$ of the grain size D typically follows a logarithmic-normal distribution,

$$P(D) = \frac{1}{\sqrt{2\pi}\sigma D} \exp\left[-\frac{\left[\ln D/\hat{D}\right]^2}{2\sigma^2}\right].$$ (6.5)

In Eq. (6.5) D is the effective diameter of a grain, $\hat{D}$ is the grain size (diameter) such that $\ln \hat{D} = \langle \ln D \rangle$, and σ is the standard deviation of $\ln(D)$.

From general and fundamental arguments [234–237] we have:

$$T_c = T_c^{\text{(bulk)}} \left(1 - \frac{1}{D/D_0}\right) ,$$ (6.6)

where $T_c^{\text{(bulk)}}$ is the bulk transition temperature and D_0, equal to 2 nm in our case, is the grain's diameter below which the grain is so small that is not possible to unambiguously identify its crystal structure. We set $T_c^{\text{(bulk)}} = 355$ K, that is the temperature above which the VO_2/Al_2O_3 samples is completely metallic. This value is higher than the value of bulk VO_2 due to the strain experienced by the films [223, 224]. The relation between $P(D)$ and $P(T_c)$ is given by:

$$P(T_c) = P(D(T_c))\frac{dD}{dT_c}.$$ (6.7)

Using Eqs. (6.2)-(6.7), by fitting the measured profile of $R(T)$ across the MIT, we can obtain $P(D)$ and therefore $\langle D \rangle$ and its standard deviation. Figures 6.6 (a), (b) show the profiles of $P(D)$ used to obtain the good theoretical fit to the evolution of $R(T)$ shown in Fig. 6.5. These profiles correspond to $\langle D \rangle = 64.7$ nm $\sigma_D = 38.5$ nm for VO_2/Al_2O_3 samples, and $\langle D \rangle = 17.4$ nm $\sigma_D = 1.1$ nm VO_2/TiO_2 samples. It is interesting to compare the values of $\langle D \rangle$ obtained using this approach to the

values estimated using XRD. From XRD data [221] we estimated $\langle D \rangle \approx 45$ nm for VO_2/Al_2O_3 and $\langle D \rangle \approx 13$ nm for VO_2/TiO_2 (see Table 6.1). These values are in remarkable semi-quantitative agreement with the values extracted from the profiles of $R(T)$ across the MIT suggesting that the assumption that the grain size is the dominant property affecting the local value of T_c might be qualitatively correct. It is therefore interesting to obtain the profiles of $P(T_c)$ corresponding to the distributions of grain sizes shown in Figs. 6.6 (a), (b). Such profiles are shown in Figs. 6.6 (c), (d). The evolution of $\eta_I(T)$ across the MIT obtained using these profiles is shown in Fig. 6.7.

	VO_2/TiO_2	VO_2/Al_2O_3
$\langle T_c \rangle$	314.0 K	340.1 K
σ_{T_c}	2.6 K	$8.8K$
$\langle D \rangle$	17.4 nm	64.7 nm
$\langle D \rangle_{Exp}$ [221]	13 nm	45 nm
σ_D	1.1 nm	38.5 nm
$n_M + ik_M$	$1.53 + i0.8$	$1.49 + i0.65$
R_M	0.14	0.11
$n_I + ik_I$	$3.03 + i0.57$	$2.60 + i0.60$
R_I	0.28	0.23
σ_K	$1,100$ W/(K cm^2)	$13,000$ W/(K cm^2)

TABLE 6.1: Comparative table between VO_2/TiO_2, and VO_2/Al_2O_3 sample parameters.

Our analysis suggest that the $R(T)$ profiles could be an indirect method to characterize the distribution of grain sizes in VO_2 films, a very challenging quantity to obtain using direct imaging experiments.
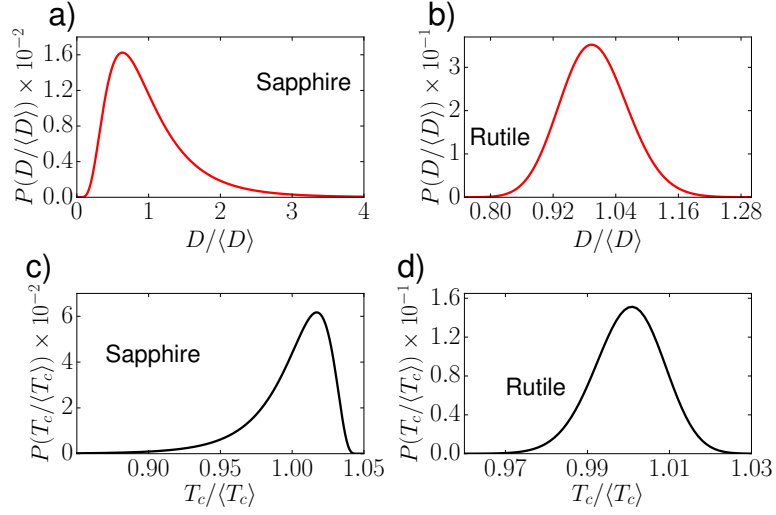
FIG. 6.6: (a) and (b) show the grain size distributions normalized to the average grain size for sapphire ($\langle D \rangle = 64.7$ nm) and rutile ($\langle D \rangle = 17.4$ nm) substrate respectively. (c) and (d) show the critical temperature distribution normalized to the average critical temperature for sapphire ($\langle T_c \rangle = 340.1$ K) and rutile ($\langle T_c \rangle = 314.0$ K) respectively. The bulk critical temperature is taken to be $T_c^{(bulk)} = 355$ K.

6.4   Theoretical modeling of the relaxation dynamics of the MIT

In our experiment the VO$_2$ films have a thickness d equal to or smaller than 110 nm (see Fig. 6.8), which is comparable with the laser $1/e$ penetration depth $\delta \simeq 110 - 130$ nm [221]. Thus, we can assume that the pump pulse heats the film uniformly throughout its thickness. To describe the heat transfer process between the film and the substrate, we assume the temperature to be uniform throughout the film for all times. Effectively, given these conditions, the heat transfer problem becomes a one-dimensional problem, and the equation for the rate of change of the heat (Q) in the film takes the form:

$$\frac{dQ}{dt} = A \times d \times \left(\rho_I C_I \eta_I(T_f) + \rho_M C_M \eta_M(T_f) + L(T_f)P(T_f)\rho_{av} \right) \frac{\partial T_f}{\partial t} , \qquad (6.8)$$
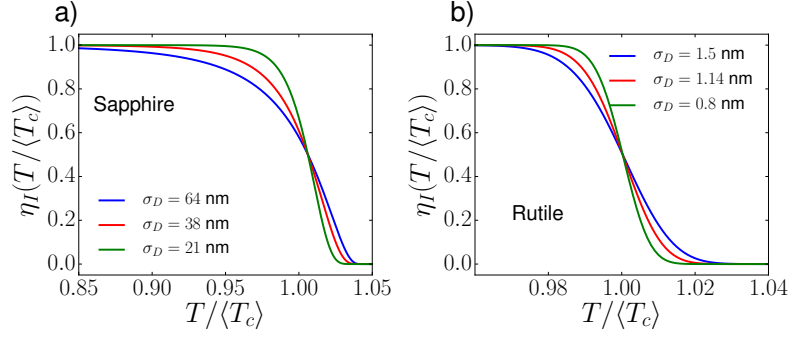
FIG. 6.7: Evolution of the insulating partial volume η_I across the thermally induced MIT for case of (a) sapphire and (b) rutile substrates. For rutile, $\langle T_c \rangle = 314.0$ K, and for sapphire $\langle T_c \rangle = 340.1$ K.
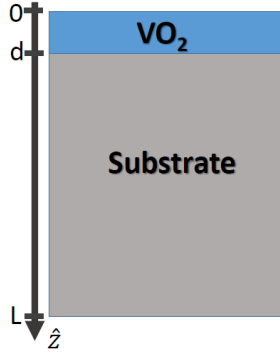
FIG. 6.8: Sketch of the heterostructure considered in this work. It is composed of a vanadium dioxide (VO$_2$) thin-film deposited on top of a substrate. The substrates considered in this work are titanium dioxide (TiO$_2$), and aluminum oxide (Al$_2$O$_3$). For VO$_2$/TiO$_2$ $d = 110$ nm while for VO$_2$/Al$_2$O$_3$ $d = 80$ nm. For both substrates, $L = 0.5$ mm.

where T_f is the film temperature, A is the area of the film, ρ_I (ρ_M) is the density in the insulating (metallic) phase, $\rho_{av} \equiv (\rho_I + \rho_M)/2$, C_I (C_M) is the heat capacity in the insulating (metallic) phase, L is the specific heat and $P(T_f)dT_f$ is the fraction of the sample undergoing the MIT in the time interval dt during which the film temperature is in the interval $[T_f, T_f + dT_f]$. Here $P(T_f)$ is the distribution of critical temperatures due to the inhomogeneities that we have obtained in the previous section. Using Eq. (6.2) and the fact that $\eta_M = (1 - \eta_I)$ we can rewrite Eq. (6.8) in a form that more explicitly shows the effect due to the inhomogeneities, i.e. the

148

fact that the MIT is not characterized by a single T_c, but by a distribution of T_c's:

$$\frac{dQ}{dt} = A \times d \times \left[\rho_M C_M + (\rho_I C_I - \rho_M C_M) \int_{T_f}^{\infty} P(T_c) dT_c + L(T_f) P(T_f) \rho_{av} \right] \frac{\partial T_f}{\partial t} \ .$$

$$(6.9)$$

Equation (6.9) is the main result of our work: it allows to properly take into account the effect of inhomogeneities on the long timescale dynamics across a first order phase transition. The key quantity entering Eq. (6.9) is the distribution $P(T_c)$ that, as we have shown in the preceding section, can be obtained from the profile of $R(T)$ across the thermally activated MIT. Our work is the first to combine the information from the thermally activated MIT to obtain a physically accurate heat equation to describe the recovery dynamics after a photo-induced MIT. For the latent heat we have [234–236]

$$L = L^{(\text{bulk})} \frac{T_c}{T_c^{(\text{bulk})}}. \tag{6.10}$$

where $L^{(\text{bulk})}$ is the value of the specific heat for bulk VO$_2$. Given Eq. (6.6), Eq. (6.10) implies $L = L^{(\text{bulk})}(1 - D_0/D)$.

The rate of change of heat in the film given by Eq. (6.8) must be equal to the heat current (J_Q) across the interface between the film and the substrate:

$$J_Q = -\sigma_K A(T_f - T_s(d)) \tag{6.11}$$

where σ_K is the Kapitza constant characterizing the thermal conductivity of the interfaces [238–241], and $T_s(d)$ is the temperature of the substrate at the surface facing the VO$_2$ film. Combining Eq. (6.9) and Eq. (6.11), for T_f we obtain the

equation:

$$\left[\rho_M C_M + (\rho_I C_I - \rho_M C_M) \int_{T_f}^{\infty} P(T_c) dT_c + L(T_f) P(T_f) \rho_{av}\right] \frac{\partial T_f}{\partial t} = -\frac{\sigma_K}{d}(T_f - T_s(d)).$$

(6.12)

In Eq. (6.12) the only undetermined quantity is σ_K. We fix σ_K by fitting the theoretically obtained time evolution of $R(t)$ to the one measured experimentally, *for fixed experimental conditions* such as the temperature of the substrate and the pump fluence. The robustness of the theory presented is evidenced by the fact that, the same *fixed* value of σ_K provides a good agreement between the theoretical and the experimental results for a broad range of experimental conditions.

To completely define the problem we need to supplement Eq. (6.12) with proper boundary conditions. The temperature distribution within the substrate, $T_s(z,t)$, satisfies the diffusion equation:

$$\frac{\partial T_s(z,t)}{\partial t} = \frac{k_s}{C_s \rho_s} \frac{\partial^2 T_s(z,t)}{\partial z^2}$$

(6.13)

where k_s, C_s, ρ_s are the thermal conductivity, heat capacity, and mass density, respectively, of the substrate. The bottom of the substrate, for which $z = L$ (see Fig. 6.8), is kept at a fixed temperature $T_s^{(B)}$. At the film/substrate interface the heat transferred from the film must be equal to the heat current $k_s \partial T_s / \partial z|_{z=d}$. We then have that the boundary conditions completing Eq. (6.13) are:

$$T_s(z = L, t) = T_s^{(B)};$$

(6.14)

$$k_s \left.\frac{\partial T_s(z,t)}{\partial z}\right|_{z=d} = -\sigma_K(T_f(t) - T_s(z = d, t)).$$

(6.15)

Equations (6.10),(6.12)-(6.15), combined with knowledge of the distribution $P(T_c)$ completely define the temperature evolution of the VO$_2$ film. Notice that in these equations the only unknown parameter is the Kapitza constant σ_K. All the other quantities are known from direct measurements. $P(T_c)$ is obtained from the profile of $R(T)$ across the MIT, independently from the dynamics of R after the photo-induced insulator-to-metal transition. Also, the relation between the specific heat L and T is fixed by general and fundamental results [234–236].

While these equations can in general be solved only numerically, some qualitative understanding of the decay time τ can be gained if we make some simplifications. Let $P(T_c) = 1/(\sqrt{2\pi}\sigma_{T_c}) \exp\{-(T_c - \langle T_c \rangle)^2/(2\sigma_{T_c}^2)\}$. At a temperature T the insulating volume fraction is given by $\eta_I(T) = \frac{1}{2}\left[1 - \text{erf}\left((T - \langle T_c \rangle)/(\sqrt{2}\sigma_{T_c})\right)\right]$. Then assuming that the pump pulse is strong enough to drive the entire film into a fully metallic state at $t = 0$, the time-dependence of the insulating volume fraction can be approximated by a simple exponential form $\eta_I(t) = 1 - Ae^{-t/\tau}$. In this case, an expression for the temperature can be obtained through the relationship $\eta_I(T(t)) = \eta_I(t)$. Furthermore, assuming that the substrate temperature T_s does not change with time, and the latent heat L to be temperature-independent, we can calculate the decay constant τ:

$$\tau = Cd\frac{\sigma_{T_c}}{\sigma_K}\frac{(C_M\rho_M + L\rho_{av}P(T_0))}{T_0 - T_s} + \tau_0 , \tag{6.16}$$

where the constants $C > 0$, and τ_0 can only be determined by solving the full system of equations (6.12)-(6.15)

It is interesting to note that despite its many limitations, Eq.(6.16) captures many important qualitative traits of the actual relaxation process. For example, Figure (6.9) shows a plot of the decay constant as a function of σ_{T_c} obtained solving

151

the full system of equations (6.12)-(6.14) for two different values of the average critical temperature, and same initial temperature $T_0 = 360$ K. It is easy to see that the decay time τ follows the linear trend predicted by Eq. (6.16) in the limit $(T_0 - \langle T_c \rangle) \gg \sqrt{2}\sigma_{T_c}$. Similarly, an exact solution shows the inverse dependence of τ on the Kapitza constant, $\tau \propto \sigma_K^{-1}$, as shown in Figure 6.10.

The relation (6.16) is another important result of our work, it shows how the characteristic time of the recovery dynamics is related to the properties of the VO$_2$ films. In particular it shows the novel result that τ grows linearly with σ_{T_c}, the standard deviation of $P(T_c)$. σ_{T_c} can be reliably obtained from the profile of $R(T)$ across the MIT.
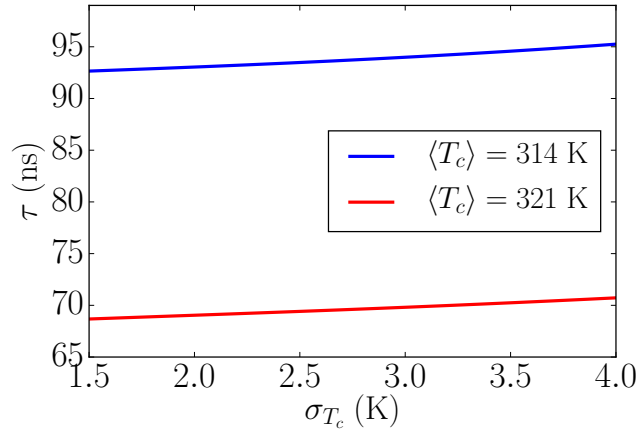
FIG. 6.9: Full numerical calculation of the dependence of metal state decay constant τ on σ_{T_c} for two different values of the sample average critical temperature $\langle T_c \rangle$, and $T_s(L) = 280$ K. The initial temperature $T_0 = 360$ K is such that the sample is initially fully metallic, and $(T_0 - \langle T_c \rangle)/(\sqrt{2}\sigma_{T_c}) \approx 9$.
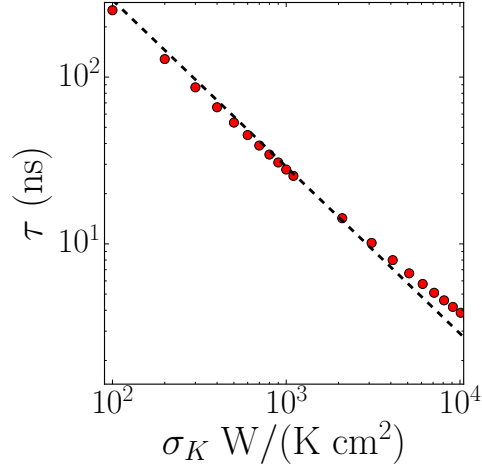
FIG. 6.10: VO_2/Al_2O_3 metal state decay time τ dependence on the Kapitza constant σ_k for $\langle D \rangle = 64.7$ nm, $\sigma_D = 38.5$ nm, substrate temperature $T_s(L) = 310$ K, and fluence $\phi = 8$ mJ/cm^2. The red dots correspond to numerical calculations, and the dashed line is given by $\tau \propto \sigma_K^{-1}$

6.5 Effect of inhomogeneities on the relaxation dynamics of the photo-induced MIT

Using the theoretical approach described in Sec. 6.4 we can obtain the time evolution of the optical reflectivity R through the MIT, as well as explain the significant difference in relaxation timescales between the two VO_2 samples considered. In all the numerical calculations we assume C_I, ρ_I, C_M, ρ_M to be equal to the bulk values for insulating and metallic VO_2, see Table 6.2.

The initial film temperature is fixed by the pump fluence taking into account the Gaussian profile of the pulse and the fact that some of the heat is lost by the film during the time interval $[0, t_0]$ for which our analysis does not apply, $t = 0$ is time at which the pump pulse hits the VO_2 film and $t_0 = 10$ ns for VO_2/TiO_2 films and $t_0 = 0.5$ ns for VO_2/Al_2O_3 films.

As discussed in Sec. 6.4, σ_K is the only unknown parameter. For the case of

VO$_2$ heat capacity insulating phase C_I [242]	0.656 J/(g K)
heat capacity metallic phase C_M [242]	0.78 J/(g K)
density insulating phase ρ_I [241]	4.57 g/cm^3
density metallic phase ρ_M [241]	4.65 g/cm^3
thermal conductivity insulating phase κ_I [243]	3.5 W/(m K)
thermal conductivity metallic phase κ_M [243]	6 W/(m K)
bulk latent heat $L^{(Bulk)}$ [242]	51.8 J/g
TiO$_2$ heat capacity C_s [244]	0.686 J/(g K)
density ρ_s [241]	4.25 g/cm^3
thermal conductivity κ_s [245]	8 W/(m K)
Al$_2$O$_3$ heat capacity C_s [246]	0.779 J/(g K)
density ρ_s [246]	3.98 g/cm^3
thermal conductivity κ_s [246]	30 W/(m K)
VO$_2$/TiO$_2$ absorption coefficient at 800 nm α [221]	0.01 nm^{-1}
VO$_2$/Al$_2$O$_3$ absorption coefficient at 800 nm α [221]	0.0076 nm^{-1}

TABLE 6.2: Parameters of VO$_2$ and substrates.

VO$_2$/TiO$_2$ samples, by fitting one of the curves for the dynamics of the reflectivity, we find $\sigma_K = 1100$ W/(K cm^2). We find that all experimental curves are well approximated assuming the same value for the Kapitza constant, see Fig. 6.11 (a). For the case of VO$_2$/Al$_2$O$_3$ the characteristic timescale of the recovery is much shorter than for VO$_2$/TiO$_2$ samples. As discussed in Sec. 6.3 the two samples have very different inhomogeneities: σ_{T_c} is almost 4 times larger in VO$_2$/Al$_2$O$_3$ than VO$_2$/TiO$_2$. All other things being equal, Eq. (6.16) implies, see Fig. 6.12, that τ should be larger in VO$_2$/Al$_2$O$_3$ than in VO$_2$/TiO$_2$, the opposite of what is observed experimentally. We are then led to conclude that σ_K in VO$_2$/Al$_2$O$_3$ must be much higher than in VO$_2$/TiO$_2$. Figure 6.13 shows the measured evolution of R for the VO$_2$/Al$_2$O$_3$ sample for a fixed value of the fluence ϕ and substrate temperature, and the theoretical curves for this case that we obtain using the distribution $P(T_c)$ obtained for VO$_2$/Al$_2$O$_3$ and two different values of σ_K. We see that by choosing

for σ_K the same value used for VO_2/TiO_2, there is no agreement between theory and experiment. By setting $\sigma_K = 13000$ W/(K cm^2) we obtain excellent agreement. Indeed, all the experimental curves $R(t)$ for VO_2/Al_2O_3 are well approximated by the theoretical results assuming $\sigma_K = 13,000$ W/(K cm^2).
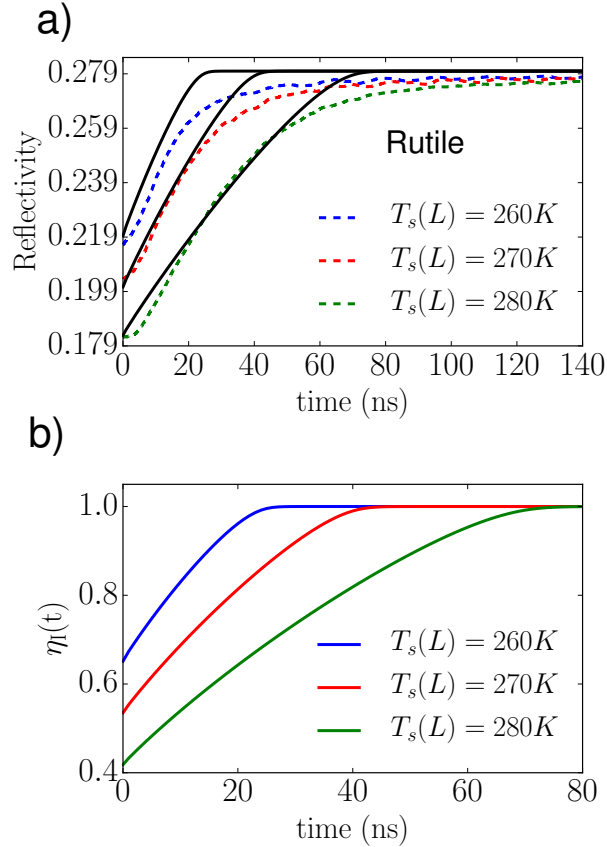
FIG. 6.11: (a) Time evolution of reflectivity after the photo-induced MIT for VO_2/TiO_2 for three different $T_s(L)$ and $\phi = 9$ mJ/cm^2. The solid curves correspond to the theoretical results, and the dashed curves correspond to the experimental results. For the three theory curves we use $\sigma_K = 1100$ W/(K cm^2). Panel (b) shows the corresponding insulating fraction time evolution.

Figure 6.14 shows the time evolution of the VO_2 film and substrate temperatures (close to the interface) for the VO_2/Al_2O_3 film, panel (a), and for the VO_2/TiO_2 film, panel (b), using the parameter values summarized in Table 6.2. It helps to qualitatively understand the differences in the thermal relaxation between the two
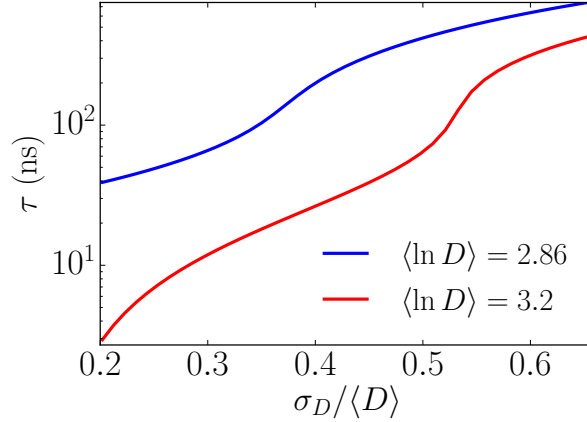
FIG. 6.12: Dependence of the VO_2/TiO_2 metal state decay time constant τ on σ_D for two values of $\langle \ln D \rangle$, as defined in Eq. (6.5), Kapitza constant $\sigma_K = 1100$ W/(K cm^2), substrate temperature $T_s(L) = 280$ K, and initial fluence $\phi = 9$ mJ/cm^2.

samples. Due to the lower values of the Kapitza constant, thermal energy stays more concentrated near the VO_2-TiO_2 interface, keeping the temperature of the VO_2 film above T_c longer.

To investigate the temperature dependence of the thermal relaxation we repeated the measurements while changing the base substrate temperature of the VO_2/TiO_2 sample. For these measurements the sample was placed inside a cryostat, and cooled down to temperatures $T_s(L)$ between 260 K and 298 K. The results of these measurements, along with the theoretical calculations, are shown in Figure 6.15. We again observe a good semiquantitative agreement between theoretical and experimental results. Also, note that the simple expression for the decay constant τ Eq. (6.16) captures the overall decay rate drop at lower substrate temperatures $T_s(L)$.

We point out that all the theoretical curves are obtained using the fixed set of parameters shown in Table 6.2. As mentioned above, the only unknown parameter that enters the theory is σ_K. In the results presented above σ_K was fixed to a
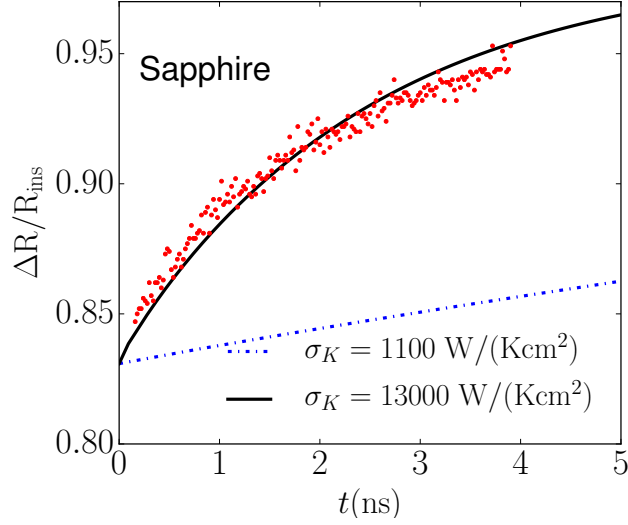
FIG. 6.13: VO_2/Al_2O_3 reflectivity time evolution after photo-induced MIT for $\phi = 7.5$ mJ/cm^2. The red dots correspond to the experimental result. The dotted curve correspond to the theory with $\sigma_K = 1100$ W/(K cm^2), and the solid curve corresponds to $\sigma_K = 13000$ W/(K cm^2).
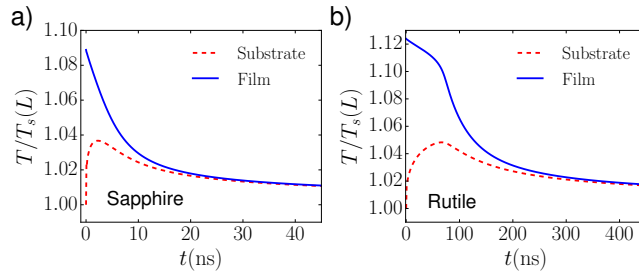
FIG. 6.14: Film and substrate temperature time evolution. For sapphire (a), $T_s(L) = 310$ K, and for rutile (b), $T_s(L) = 280$ K.

single value for each film, and this value was then used to obtain the results for a range of experimental conditions with different substrate temperatures and pump fluences. For example, Fig. 6.4 shows an excellent agreement between the experimental measurements and theoretical calculations across the entire range of pump fluences, limited on the lower end by our ability to reliably detect the variation in the probe reflectivity, and on the upper end by the damage threshold of our sample (pump fluence > 40mJ/cm^2).
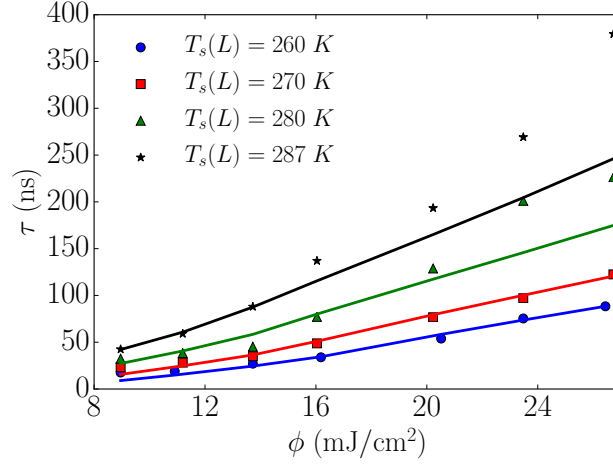
FIG. 6.15: Dependence of metal state decay constant τ on fluence and substrate temperature for VO_2/TiO_2.

6.6 Conclusions

In conclusion, we have presented a combined experimental and theoretical study of the long timescale recovery dynamics of VO_2 films following an ultrafast photo-induced insulator-to-metal transition. We have developed a theoretical approach that is able to properly take into account the effect of inhomogeneities. The main results of our work are: (i) The derivation of the generalized heat equation (6.9) that properly takes into account that during the recovery, due to the inhomogeneities, only fraction of the sample is undergoing the metal-to-insulator transition and correctly tracks the evolution in time of the metallic (insulating) phase; (ii) The clarification of the connection between the temperature dependent profile ($R(T)$) of the reflectivity across the thermally induced MIT and its dynamics after a photo-induced insulator-to-metal transition; (iii) The approximate relation, Eq. (6.16), between the characteristic time of the recovery dynamics and the parameters of the film, in particular to the standard deviation of the distribution of critical temperatures as extracted from $R(T)$; (iv) The ability of our theory to describe, using a

fixed value of the Kapitza constant, the recovery dynamics for different values of the substrate temperature and pump fluence. By changing the pump fluence the characteristic time of the recovery can be changed, experimentally, by two orders of magnitude: our theory is able to account for such a change.

The theoretical approach that we present is general and can be used to describe the dynamics (in the adiabatic limit) of inhomogeneous systems across a first order phase transition. The approximate relation between the characteristic time τ and the parameters of the system shows that τ is directly proportional to the width of the thermally activated transition. This result allows to estimate the recovery time of VO$_2$ films solely on the basis of a measurement of $R(T)$ across the MIT.

Assuming that variations of the size of the grains forming the films are the main source of inhomogeneities, using very general and fundamental relations between the grain size and the grain's critical temperature, we have been able to obtain the distribution of the grain sizes. In particular, we have been able to estimate the average grain's size and its standard deviation. We find that the calculated average grain's size is in remarkable semi-quantitative agreement with the one obtained from XRD measurements. For systems in which inhomogeneities are mostly due to variations of the size D of the grains, our analysis provides a way to obtain the size distribution $P(D)$ from the temperature dependent profile of the reflectivity across the thermally induced MIT. This could be very useful considering that $P(D)$ is a very challenging quantity to obtain via direct measurements.

CHAPTER 7

Conclusions

In summary, in this dissertation, we have studied the effect of disorder in Dirac heterostructures. We started with a heterostructure composed of two graphene layers separated by a dielectric field. We determined self-consistently the electronic ground state of the system implementing a density functional Thomas-Fermi-Dirac theory scheme, which allowed us to take into account nonlinear screening effects and consider large systems by doing averages over disorder realizations. We found that the disorder strength and density fluctuations were reduced in hybrid heterostructures composed of a layer of single-layer graphene and a layer of bilayer graphene, compared with SLG, and SLG-SLG systems. We proved that density fluctuations in the two graphenic layers were always correlated, and that the observed percolation-like metal-to-insulator transition in double-layer graphene heterostructures is driven by the reduction of electron-hole puddles due the additional screening provided by the second graphene layer.

We presented a summary of experimental results obtained on SLG-SLG heterostructures. It was demonstrated that the presence of a 2D crystal buffer (graphene)

between the substrate and the study layer (also graphene) reduces the effect of the substrate while preserving the electronic properties of the study layer, provided they are decoupled. This decoupling is achieved by twisting the layers with respect to each other.

Once the ground state of the SLG-SLG system was theoretically characterized, and experimental results were obtained, we considered the possible establishment of an exciton condensate without an applied magnetic field. Given the character of the screening of the interlayer Coulomb interactions is unknown, we considered the two limiting cases of unscreened and static screening electron-electron interactions between the two graphene layers. We found that the carrier density fluctuations play a crucial role. The exciton condensate has the possibility to be detected only in the case of unscreened interactions and spotless samples.

Then, we considered a Dirac heterostructures composed of a graphene layer placed on top of a three-dimensional topological insulator. This kind of heterostructure is expected to have spintronic applications, as a device that allows the manipulation of a ferromagnet magnetization using electric currents. We calculated the transport properties, and the current-induced spin density accumulation in the linear response regime using the Kubo formalism. We considered two limiting layer coupling regimes, a strong coupling regime characterized by coherent tunneling; and a weak tunneling regime, characterized by random tunneling events. The effect of long- and short-range disorder was considered in the calculation. We found that the TI|graphene system presented a more efficient spin accumulation creation, compared with the TI alone, and that such a spin accumulation is present even in the weak coupling regime.

Finally, we moved away from Dirac materials and considered the effect of long-range inhomogeneities in first-order phase transitions. Specifically, we examined

a metal-to-insulator transition in vanadium dioxide (VO_2). We determined the recovery dynamics of the VO_2 thin films grown in different substrates. Experiments performed on such systems allowed to test the model in various time scales.

We expect that the work presented in this dissertation will help to better understand the physics of systems in which long-range disorder plays an essential role.

BIBLIOGRAPHY

[1] K. S. Novoselov, A. K. Geim, S. V. Morozov, D. Jiang, Y. Zhang, S. V. Dubonos, I. V. Grigorieva, and A. A. Firsov, Science **306**, 666 (2004).

[2] C. L. Kane and E. J. Mele, Phys. Rev. Lett. **95**, 226801 (2005).

[3] B. A. Bernevig, T. L. Hughes, and S. C. Zhang, Science **314**, 1757 (2006).

[4] M. König, S. Wiedmann, C. Brüne, A. Roth, H. Buhmann, L. W. Molenkamp, X.-L. Qi, and S.-C. Zhang, Science **318**, 766 (2007).

[5] J.-H. Chen, C. Jang, M. Ishigami, S. Xiao, W. Cullen, E. Williams, and M. Fuhrer, Solid State Commun. **149**, 1080 (2009).

[6] A. V. Balatsky, I. Vekhter, and J. X. Zhu, Rev. Modern Phys. **78**, 373 (2006).

[7] T. Wehling, A. Black-Schaffer, and A. Balatsky, Advances in Physics **63**, 1 (2014).

[8] L. A. Ponomarenko, A. K. Geim, A. A. Zhukov, R. Jalil, S. V. Morozov, K. S. Novoselov, I. V. Grigorieva, E. H. Hill, V. V. Cheianov, V. I. Fal'Ko, et al., Nature Physics **7**, 958 (2011).

[9] L. Britnell, R. V. Gorbachev, R. Jalil, B. D. Belle, F. Schedin, A. Mishchenko, T. Georgiou, M. I. Katsnelson, L. Eaves, S. V. Morozov, et al., Science **335**, 947 (2012).

[10] S. J. Haigh, A. Gholinia, R. Jalil, S. Romani, L. Britnell, D. C. Elias, K. S. Novoselov, L. A. Ponomarenko, A. K. Geim, and R. Gorbachev, Nature Materials **11**, 764 (2012).

[11] R. V. Gorbachev, A. K. Geim, M. I. Katsnelson, K. S. Novoselov, T. Tudorovskiy, I. V. Grigorieva, A. H. MacDonald, S. V. Morozov, K. Watanabe, T. Taniguchi, et al., Nature Physics **8**, 896 (2012).

[12] M. Rodriguez-Vega, J. Fischer, S. Das Sarma, and E. Rossi, Phys. Rev. B **90**, 035406 (2014).

[13] C.-P. Lu, M. Rodriguez-Vega, G. Li, A. Luican-Mayer, K. Watanabe, T. Taniguchi, E. Rossi, and E. Y. Andrei, PNAS **13**, 6623 (2016).

[14] R. Nandkishore and L. Levitov, Physica Scripta **2012**, 014011 (2012).

[15] B. Feldman, J. Martin, and A. Yacoby, Nature Physics (advance online publication) 10.1038/nphys1406 (2009).

[16] J. Martin, B. E. Feldman, R. T. Weitz, M. T. Allen, and A. Yacoby, Phys. Rev. Lett. **105**, 256806 (2010).

[17] R. T. Weitz, M. T. Allen, B. E. Feldman, J. Martin, and A. Yacoby, Science **330**, 812 (2010).

[18] A. S. Mayorov, D. C. Elias, M. Mucha-Kruczynski, R. V. Gorbachev, T. Tudorovskiy, A. Zhukov, S. V. Morozov, M. I. Katsnelson, A. K. Geim, and K. S. Novoselov, Science **333**, 860 (2011).

[19] J. Velasco, L. Jing, W. Bao, Y. Lee, P. Kratz, V. Aji, M. Bockrath, C. N. Lau, C. Varma, R. Stillwell, et al., Nature Nanotechnology **7**, 156 (2012).

[20] F. Freitag, J. Trbovic, M. Weiss, and C. Schönenberger, Phys. Rev. Lett. **108**, 076602 (2012).

[21] W. Bao, J. Velasco, F. Zhang, L. Jing, B. Standley, D. Smirnov, M. Bockrath, A. H. MacDonald, and C. N. Lau, Proceedings of the National Academy of Sciences **109**, 10802 (2012).

[22] A. Veligura, H. J. van Elferen, N. Tombros, J. C. Maan, U. Zeitler, and B. J. van Wees, Phys. Rev. B **85**, 155412 (2012).

[23] F. Freitag, M. Weiss, R. Maurand, J. Trbovic, and C. Schönenberger, Phys. Rev. B **87**, 161402 (2013).

[24] C.-H. Zhang and Y. N. Joglekar, Phys. Rev. B **77**, 233405 (2008), URL http://link.aps.org/doi/10.1103/PhysRevB.77.233405.

[25] H. Min, R. Bistritzer, J.-J. Su, and A. H. MacDonald, Phys. Rev. B **78**, 121401 (2008), URL http://link.aps.org/doi/10.1103/PhysRevB.78.121401.

[26] D. S. L. Abergel, M. Rodriguez-Vega, E. Rossi, and S. Das Sarma, Phys. Rev. B **88**, 235402 (2013).

[27] C. R. Dean, A. F. Young, I. Meric, C. Lee., L. Wang, S. Sorgenfrei, K. Watanabe, T. Taniguchi, P. Kim, K. L. Shepard, et al., Nature Nanotechnology **5**, 726 (2010).

[28] M. Z. Hasan and C. L. Kane, Rev. Mod. Phys. **82**, 3045 (2010).

[29] E. Rossi and S. Das Sarma, Phys. Rev. Lett. **101**, 166803 (2008).

[30] D. Culcer, E. H. Hwang, T. D. Stanescu, and S. Das Sarma, Phys. Rev. B **82**, 155457 (2010).

[31] Q. Li, E. Rossi, and S. Das Sarma, Phys. Rev. B **86**, 235443 (2012).

[32] H. Steinberg, L. A. Orona, V. Fatemi, J. D. Sanchez-Yamagishi, K. Watanabe, T. Taniguchi, and P. Jarillo-Herrero, ArXiv:1504.08311 (2015).

[33] M. Rodriguez-Vega, M. T. Simons, E. Radue, S. Kittiwatanakul, J. Lu, S. A. Wolf, R. A. Lukaszew, I. Novikova, and E. Rossi, Phys. Rev. B **92**, 115420 (2015).

[34] J. Cayssol, Comptes Rendus Physique **14**, 760 (2013).

[35] P. A. M. Dirac, Proceedings of the Royal Society of London A: Mathematical, Physical and Engineering Sciences **117**, 610 (1928).

[36] A. H. Castro Neto, F. Guinea, N. M. R. Peres, K. S. Novoselov, and A. K. Geim, Rev. Mod. Phys. **81**, 109 (2009).

[37] R. S. Deacon, K.-C. Chuang, R. J. Nicholas, K. S. Novoselov, and A. K. Geim, Phys. Rev. B **76**, 081406 (2007).

[38] P. R. Wallace, Phys. Rev. **71**, 622 (1947).

[39] S. Das Sarma, S. Adam, E. H. Hwang, and E. Rossi, Rev. Mod. Phys. **83**, 407 (2011).

[40] A. H. Castro Neto, F. Guinea, N. M. R. Peres, K. S. Novoselov, and A. K. Geim, Rev. Mod. Phys. **81**, 109 (2009).

[41] A. Bostwick, T. Ohta, T. Seyller, K. Horn, and E. Rotenberg, Nature Physics **3**, 36 (2007).

[42] M. Sprinkle, D. Siegel, Y. Hu, J. Hicks, A. Tejeda, A. Taleb-Ibrahimi, P. Le Fèvre, F. Bertran, S. Vizzini, H. Enriquez, et al., Phys. Rev. Lett. **103**, 226803 (2009).

[43] G. M. Rutter, J. N. Crain, N. P. Guisinger, T. Li, P. N. First, and J. A. Stroscio, Science **317**, 219 (2007).

[44] Y. Zhang, Y.-W. Tan, H. L. Stormer, and P. Kim, Nature **438**, 201 (2005).

[45] M. Franz and L. Molenkamp, eds., *Topological Insulators*, vol. 6 of *Contemporary Concepts of Condensed Matter Science* (Elsevier, 2013).

[46] X.-L. Qi and S.-C. Zhang, Rev. Mod. Phys. **83**, 1057 (2011).

[47] M. Nakahara, *Geometry, topology, and physics*, Graduate student series in physics (Institute of Physics Publishing, Bristol, Philadelphia, 2003), ISBN 0-7503-0606-8, URL `http://opac.inria.fr/record=b1120046`.

[48] K. V. Klitzing, G. Dorda, and M. Pepper, Phys. Rev. Lett. **45**, 494 (1980).

[49] R. Kubo, Journal of the Physical Society of Japan **12**, 570 (1957).

[50] D. J. Thouless, M. Kohmoto, M. P. Nightingale, and M. den Nijs, Phys. Rev. Lett. **49**, 405 (1982).

[51] F. D. M. Haldane, Phys. Rev. Lett. **61**, 2015 (1988).

[52] R. Winkler, *Spin-orbit coupling effects in two-dimensional electron and hole systems*, Springer tracts in modern physics (Springer, Berlin, 2003).

[53] M. Dyakonov and V. Perel, Physics Letters A **35**, 459 (1971).

[54] S. Murakami, N. Nagaosa, and S. C. Zhang, Science **301**, 1348 (2003).

[55] J. Sinova, D. Culcer, Q. Niu, N. A. Sinitsyn, T. Jungwirth, and A. H. Mac-Donald, Phys. Rev. Lett. **92**, 126603 (2004).

[56] J. Maciejko, T. L. Hughes, and S.-C. Zhang, Annual Review of Condensed Matter Physics **2**, 31 (2011).

[57] Y. K. Kato, R. C. Myers, A. C. Gossard, and D. D. Awschalom, Science **306**, 1910 (2004).

[58] J. Wunderlich, B. Kaestner, J. Sinova, and T. Jungwirth, Phys. Rev. Lett. **94**, 047204 (2005).

[59] C. L. Kane and E. J. Mele, Phys. Rev. Lett. **95**, 146802 (2005).

[60] L. Fu and C. L. Kane, Phys. Rev. B **74**, 195312 (2006).

[61] A. Roth, C. Brüne, H. Buhmann, L. W. Molenkamp, J. Maciejko, X.-L. Qi, and S.-C. Zhang, Science **325**, 294 (2009).

[62] C. Liu, T. L. Hughes, X.-L. Qi, K. Wang, and S.-C. Zhang, Phys. Rev. Lett. **100**, 236601 (2008).

[63] L. Fu and C. L. Kane, Phys. Rev. B **76**, 045302 (2007).

[64] J. E. Moore and L. Balents, Phys. Rev. B **75**, 121306 (2007).

[65] R. Roy, Phys. Rev. B **79**, 195322 (2009).

[66] L. Fu and C. L. Kane, Phys. Rev. B **76**, 045302 (2007), URL http://link.aps.org/doi/10.1103/PhysRevB.76.045302.

[67] H. Nielsen and M. Ninomiya, Physics Letters B **105**, 219 (1981).

[68] F. Zhang, C. L. Kane, and E. J. Mele, Phys. Rev. B **86**, 081303 (2012).

[69] D. Hsieh, D. Qian, L. Wray, Y. Xia, Y. S. Hor, R. J. Cava, and M. Z. Hasan, Nature **452**, 970 (2008).

[70] H. Zhang, C.-X. Liu, X.-L. Qi, X. Dai, Z. Fang, and S.-C. Zhang, Nat Phys **5**, 438 (2009).

[71] D. Hsieh, Y. Xia, D. Qian, L. Wray, F. Meier, J. H. Dil, J. Osterwalder, L. Patthey, A. V. Fedorov, H. Lin, et al., Phys. Rev. Lett. **103**, 146401 (2009).

[72] Y. S. Hor, A. Richardella, P. Roushan, Y. Xia, J. G. Checkelsky, A. Yazdani, M. Z. Hasan, N. P. Ong, and R. J. Cava, Phys. Rev. B **79**, 195208 (2009).

[73] D. Hsieh, Y. Xia, D. Qian, L. Wray, J. H. Dil, F. Meier, L. Patthey, J. Oster-walder, A. V. Fedorov, H. Lin, et al., ArXiv e-prints (2009).

[74] J.-H. Chen, W. G. Cullen, C. Jang, M. S. Fuhrer, and E. D. Williams, Phys. Rev. Lett. **102**, 236805 (2009).

[75] S. R. Park, W. S. Jung, C. Kim, D. J. Song, C. Kim, S. Kimura, K. D. Lee, and N. Hur, Phys. Rev. B **81**, 041405 (2010).

[76] K. Novoselov, E. McCann, S. Morozov, V. Falko, M. Katsnelson, U. Zeitler, D. Jiang, F. Schedin, and A. Geim, Nature Physics **2**, 177 (2006).

[77] K. S. Novoselov, D. Jiang, F. Schedin, T. J. Booth, V. V. Khotkevich, S. V. Morozov, and A. K. Geim, Proc. Nat. Acad. Sci. (USA) **102**, 10451 (2005).

[78] Z. Q. Li, E. A. Henriksen, Z. Jiang, Z. Hao, M. C. Martin, P. Kim, H. L. Stormer, and D. N. Basov, Phys. Rev. Lett. **102**, 037403 (2009).

[79] A. Ismach, H. Chou, D. A. Ferrer, Y. P. Wu, S. McDonnell, H. C. Floresca, A. Covacevich, C. Pope, R. Piner, M. J. Kim, et al., Acs Nano **6**, 6378 (2012).

[80] S. Kim, J. Nah, I. Jo, D. Shahrjerdi, L. Colombo, Z. Yao, E. Tutuc, and S. K. Banerjee, Applied Physics Letters **94**, 062107 (2009).

[81] S. Kim and E. Tutuc, Solid State Communications **152**, 1283 (2012).

[82] B. Hunt, J. D. Sanchez-Yamagishi, A. F. Young, M. Yankowitz, B. J. LeRoy, K. Watanabe, T. Taniguchi, P. Moon, M. Koshino, P. Jarillo-Herrero, et al., Science **340**, 1427 (2013).

[83] L. Britnell, R. M. Ribeiro, A. Eckmann, R. Jalil, B. D. Belle, A. Mishchenko, Y. J. Kim, R. V. Gorbachev, T. Georgiou, S. V. Morozov, et al., Science **340**, 1311 (2013).

[84] G. H. Lee, Y. J. Yu, X. Cui, N. Petrone, C. H. Lee, M. S. Choi, D. Y. Lee, C. Lee, W. J. Yoo, K. Watanabe, et al., Acs Nano **7**, 7931 (2013).

[85] A. Gamucci, D. Spirito, M. Carrega, B. Karmakar, A. Lombardo, M. Bruna, A. C. Ferrari, L. N. Pfeiffer, K. W. West, M. Polini, et al., ArXiv e-prints (2014), `1401.0902`.

[86] W. H. Dang, H. L. Peng, H. Li, P. Wang, and Z. F. Liu, Nano Lett. **10**, 2870 (2010).

[87] C.-L. Song, Y.-L. Wang, Y.-P. Jiang, Y. Zhang, C.-Z. Chang, L. Wang, K. He, X. Chen, J.-F. Jia, Y. Wang, et al., Applied Physics Letters **97**, 143118 (2010).

[88] K.-H. Jin and S.-H. Jhi, Phys. Rev. B **87**, 075442 (2013).

[89] J. Zhang, C. Triola, and E. Rossi, Phys. Rev. Lett. **112**, 096802 (2014).

[90] J. Xue, J. Sanchez-Yamagishi, D. Bulmash, P. Jacquod, A. Deshpande, K. Watanabe, T. Taniguchi, P. Jarillo-Herrero, and B. J. Leroy, Nat. Mat. **10**, 282 (2011).

[91] M. Yankowitz, J. Xue, D. Cormode, J. D. Sanchez-Yamagishi, K. Watanabe, T. Taniguchi, P. Jarillo-Herrero, P. Jacquod, and B. J. Leroy, Nature Physics **8**, 382 (2012).

[92] A. K. Geim and I. V. Grigorieva, Nature **499**, 419 (2013).

[93] H. Min, G. Borghi, M. Polini, and A. H. MacDonald, Phys. Rev. B **77**, 041407 (2008).

[94] C. H. Zhang and Y. N. Joglekar, Phys. Rev. B **77**, 233405 (2008).

[95] M. Y. Kharitonov and K. B. Efetov, Phys. Rev. B **78**, 241401 (2008).

[96] M. Y. Kharitonov and K. B. Efetov, Semiconductor Science Technology **25**, 034004 (2010).

[97] F. Zhang, H. Min, M. Polini, and A. H. MacDonald, Phys. Rev. B **81**, 041402 (2010).

[98] J. Zhang and E. Rossi, Phys. Rev. Lett. **111**, 086804 (2013).

[99] J. Martin, N. Akerman, G. Ulbricht, T. Lohmann, J. H. Smet, K. von Klitzing, and A. Yacobi, Nature Physics **4**, 144 (2008).

[100] Y. Zhang, V. Brar, C. Girit, A. Zettl, and M. Crommie, Nature Physics **5**, 722 (2009).

[101] A. Deshpande, W. Bao, F. Miao, C. N. Lau, and B. J. LeRoy, Phys. Rev. B **79**, 205411 (2009).

[102] A. Deshpande, W. Bao, Z. Zhao, C. N. Lau, and B. J. LeRoy, Appl. Phys. Lett. **95**, 243502 (2009).

[103] D. S. L. Abergel, R. Sensarma, and S. Das Sarma, Phys. Rev. B **86**, 161412 (2012).

[104] D. K. Efimkin, V. A. Kulbachinskii, and Y. E. Lozovik, JETP Letters **93**, 219 (2011).

[105] R. Bistritzer and A. H. MacDonald, Phys. Rev. Lett. **101**, 256406 (2008).

[106] J. Zhang, R. Nandkishore, and E. Rossi, ArXiv e-prints (2014), `1401.0727`.

[107] J. C. W. Song and L. S. Levitov, Phys. Rev. Lett. **109**, 236602 (2012).

[108] J. C. W. Song, D. A. Abanin, and L. S. Levitov, ArXiv e-prints (2013), `1304.1450`.

[109] E. H. Hwang, S. Adam, and S. Das Sarma, Phys. Rev. Lett. **98**, 186806 (2007).

[110] S. Adam, E. H. Hwang, V. M. Galitski, and S. Das Sarma, Proc. Natl. Acad. Sci. USA **104**, 18392 (2007).

[111] E. Rossi, S. Adam, and S. D. Sarma, Phys. Rev. B **79**, 245423 (2009).

[112] M. M. Fogler, Phys. Rev. Lett. **103**, 236801 (2009).

[113] E. Rossi, J. H. Bardarson, M. S. Fuhrer, and S. Das Sarma, Phys. Rev. Lett. **109**, 096801 (2012).

[114] J. Oostinga, H. Heersche, X. Liu, A. Morpurgo, and L. Vandersypen, Nature Materials **7**, 151 (2008).

[115] Y. B. Zhang, T. T. Tang, C. Girit, Z. Hao, M. C. Martin, A. Zettl, M. F. Crommie, Y. R. Shen, and F. Wang, Nature **459**, 820 (2009).

[116] K. Nomura and A. H. MacDonald, Phys. Rev. Lett. **96**, 256602 (2006).

[117] J. H. Chen, C. Jang, S. Adam, M. S. Fuhrer, E. D. Williams, and M. Ishigami, Nature Physics **4**, 377 (2008).

[118] Q. Li, E. H. Hwang, E. Rossi, and S. Das Sarma, Phys. Rev. Lett. **107**, 156601 (2011).

[119] Q. Li, E. H. Hwang, and E. Rossi, Solid State Communications **152**, 1390 (2012).

[120] J. Yan and M. S. Fuhrer, Phys. Rev. Lett. **107**, 206601 (2011).

[121] A. H. C. Neto, F. Guinea, N. M. R. Peres, K. S. Novoselov, and A. K. Geim, Rev. Mod. Phys. **81**, 109 (2009).

[122] F. Amet, J. R. Williams, K. Watanabe, T. Taniguchi, and D. Goldhaber-Gordon, Phys. Rev. Lett. **110**, 216601 (2013).

[123] J. Jung, A. DaSilva, S. Adam, and A. H. MacDonald, ArXiv e-prints (2014), `1403.0496`.

[124] H. Min, B. Sahu, S. K. Banerjee, and A. H. MacDonald, Phys. Rev. B **75** (2007).

[125] C. Triola and E. Rossi, Phys. Rev. B **86**, 161408 (2012).

[126] D. S. L. Abergel, E. Rossi, and S. Das Sarma, Phys. Rev. B **86**, 155447 (2012).

[127] M. Polini, A. Tomadin, R. Asgari, and A. MacDonald, Phys. Rev. B **78**, 115426 (2008).

[128] S. D. Sarma, E. H. Hwang, and E. Rossi, Phys. Rev. B **81**, 161407(R) (2010).

[129] E. Rossi and S. Das Sarma, Phys. Rev. Lett. **107**, 155502 (2011).

[130] L. Brey and H. A. Fertig, Phys. Rev. B **80**, 035406 (2009).

[131] B. I. Shklovskii and A. L. Efros, *Electronic Properties of Doped Semiconductors* (Springer, New York, 1984).

[132] A. L. Efros, F. G. Pikus, and V. G. Burnett, Phys. Rev. B **47**, 2233 (1993).

[133] A. Perali, D. Neilson, and A. R. Hamilton, Phys. Rev. Lett. **110**, 146803 (2013).

[134] T. Taychatanapat and P. Jarillo-Herrero, Phys. Rev. Lett. **105**, 166601 (2010).

[135] K. Zou and J. Zhu, Phys. Rev. B **82**, 081407 (2010).

[136] J. Yan and M. S. Fuhrer, Nano Letters **10**, 4521 (2010).

[137] K. Kechedzhi, E. H. Hwang, and S. Das Sarma, Phys. Rev. B **86**, 165442 (2012).

[138] S. Das Sarma, E. H. Hwang, and Q. Li, Phys. Rev. B **85**, 195451 (2012).

[139] H. Min, R. Bistritzer, J. Su, and A. H. MacDonald, Phys. Rev. B, (R) **78**, 121401 (2008).

[140] Y. Lemonik, I. Aleiner, and V. I. Fal'ko, Phys. Rev. B **85**, 245451 (2012).

[141] J. Zhang, R. Nandkishore, and E. Rossi, Phys. Rev. B **91**, 205425 (2015).

[142] M. J. P. Gingras and D. A. Huse, Phys. Rev. B **53**, 15193 (1996).

[143] Y. Imry and S.-k. Ma, Phys. Rev. Lett. **35**, 1399 (1975).

[144] S. Sachdev, *Quantum phase transitions* (Cambridge University Press, Cambridge, 2011).

[145] A. *et. al.*. Dutta, ArXiv:1012.0653 (2015).

[146] N. Akino and J. M. Kosterlitz, Phys. Rev. B **66**, 054536 (2002).

[147] C. Monthus and T. Garel, Journal of Statistical Mechanics: Theory and Experiment **2012**, P09016 (2012).

[148] H. Yi, Phys. Rev. E **91**, 012146 (2015).

[149] E. Y. Andrei, G. Li, and X. Du, Reports on Progress in Physics **75**, 056501 (2012).

[150] A. Luican, G. Li, A. Reina, J. Kong, R. R. Nair, K. S. Novoselov, A. K. Geim, and E. Y. Andrei, Phys. Rev. Lett. **106**, 126802 (2011).

[151] L. V. Keldysh and A. N. Nozlov, Sov. Phys. JETP **27**, 521 (1967).

[152] Y. E. Lozovik and V. I. Yudson, Sov. Phys. JEPT **44**, 389 (1976).

[153] J. Zhang and E. Rossi, Phys. Rev. Lett. **111**, 086804 (2013), URL http://link.aps.org/doi/10.1103/PhysRevLett.111.086804.

[154] S. Kim, I. Jo, J. Nah, Z. Yao, S. K. Banerjee, and E. Tutuc, Phys. Rev. B **83**, 161401 (2011).

[155] M. Y. Kharitonov and K. B. Efetov, Phys. Rev. B **78**, 033404 (2008).

[156] Y. E. Lozovik and A. A. Sokolik, JETP Letters **87**, 55 (2011).

[157] I. Sodemann, D. A. Pesin, and A. H. MacDonald, Phys. Rev. B **85**, 195136 (2012).

[158] Y. E. Lozovik, S. L. Ogarkov, and A. A. Sokolik, Phys. Rev. B **86**, 045429 (2012).

[159] M. P. Mink, H. T. C. Stoof, R. A. Duine, and A. H. MacDonald, Phys. Rev. B **84**, 155409 (2011).

[160] R. Bistritzer, H. Min, J. J. Su, and A. H. MacDonald, ArXiv e-prints (2008), 0810.0331.

[161] S. Das Sarma, E. H. Hwang, and W.-K. Tse, Phys. Rev. B **75**, 121406 (2007).

[162] D. K. Efimkin, V. A. Kulbachinskii, and Y. E. Lozovik, JETP Letters **93**, 219 (2011).

[163] E. H. Hwang, B. Y.-K. Hu, and S. Das Sarma, Phys. Rev. B **76**, 115434 (2007).

[164] R. Decker, Y. Wang, V. W. Brar, W. Regan, H.-Z. Tsai, Q. Wu, W. Gannett, A. Zettl, and M. F. Crommie, Nano Letters **11**, 2291 (2011).

[165] D. Kim, S. Cho, N. P. Butch, P. Syers, K. Kirshenbaum, J. Paglione, and M. S. Fuhrer, arXiv:1105.1410v2 (2011).

[166] C. Huan, Contemporary Physics **55**, 127 (2014).

[167] J. Katine and E. E. Fullerton, Journal of Magnetism and Magnetic Materials **320**, 1217 (2008).

[168] J. E. Hirsch, Phys. Rev. Lett. **83**, 1834 (1999).

[169] V. Edelstein, Solid State Communications **73**, 233 (1990).

[170] A. Chernyshov, M. Overby, X. Liu, J. K. Furdyna, Y. Lyanda-Geller, and L. P. Rokhinson, Nat Phys **5**, 656 (2009).

[171] M. I. Dyakonov, *Spin physics in semiconductors*, Springer series in solid state sciences (Springer, Dordrecht, 2008).

[172] I. Garate and A. H. MacDonald, Phys. Rev. B **80**, 134403 (2009).

[173] I. Garate and M. Franz, Phys. Rev. Lett. **104**, 146802 (2010).

[174] T. Yokoyama, Y. Tanaka, and N. Nagaosa, Phys. Rev. B **81**, 121401 (2010).

[175] A. Sakai and H. Kohno, Phys. Rev. B **89**, 165307 (2014).

[176] M. Fischer H., A. Vaezi, A. Manchon, and E.-A. Kim, arXiv:1305.1328 (2013).

[177] A. R. Mellnik, J. S. Lee, A. Richardella, J. L. Grab, P. J. Mintun, M. H. Fischer, A. Vaezi, A. Manchon, E.-A. Kim, N. Samarth, et al., Nature **511**, 449 (2014).

[178] D. A. Kozlov, Z. D. Kvon, E. B. Olshanetsky, N. N. Mikhailov, S. A. Dvoretsky, and D. Weiss, Phys. Rev. Lett. **112**, 196801 (2014).

[179] D. Kim, S. Cho, N. P. Butch, P. Syers, K. Kirshenbaum, S. Adam, J. Paglione, and M. S. Fuhrer, Nature Phys. **8**, 458 (2012).

[180] J. Zhang, C. Triola, and E. Rossi, Phys. Rev. Lett. **112**, 096802 (2014).

[181] Y. A. Bychkov and E. I. Rashba, Journal of Physics C: Solid State Physics **17**, 6039 (1984).

[182] P. D. C. King, R. C. Hatch, M. Bianchi, R. Ovsyannikov, C. Lupulescu, G. Landolt, B. Slomski, J. H. Dil, D. Guan, J. L. Mi, et al., Phys. Rev. Lett. **107**, 096802 (2011).

[183] S. Wang, L. Zhu, Q. Chen, J. Wang, and F. Ding, Journal of Applied Physics **109** (2011).

[184] Z. Ren, A. A. Taskin, S. Sasaki, K. Segawa, and Y. Ando, Phys. Rev. B **85**, 155301 (2012).

[185] G. Hao, X. Qi, L. Xue, C. Cai, J. Li, X. Wei, and J. Zhong, Journal of Applied Physics **113** (2013).

[186] T.-H. Kim, K. Jeong, B. C. Park, H. Choi, S. H. Park, S. Jung, J. Park, K.-H. Jeong, J. W. Kim, J. H. Kim, et al., Nanoscale **8**, 741 (2016).

[187] M. Aitani, Y. Sakamoto, T. Hirahara, M. Yamada, H. Miyazaki, M. Matsunami, S. ichi Kimura, and S. Hasegawa, Japanese Journal of Applied Physics **52**, 110112 (2013).

[188] N. Bansal, Y. S. Kim, M. Brahlek, E. Edrey, and S. Oh, Phys. Rev. Lett. **109** (2012).

[189] G. D. Mahan, *Many-Particle Physics* (Plenum, New York, N.Y., 1993), 2nd ed.

[190] W. Luo and X.-L. Qi, Phys. Rev. B **87**, 085431 (2013).

[191] G. F. Giuliani and G. Vignale, *Quantum theory of the electron liquid* (Cambridge Univ. Press, Cambridge, 2005).

[192] R. R. Biswas and S. Ryu, Phys. Rev. B **89**, 014205 (2014).

[193] I. Garate and L. Glazman, Phys. Rev. B **86**, 035422 (2012).

[194] N. A. Sinitsyn, A. H. MacDonald, T. Jungwirth, V. K. Dugaev, and J. Sinova, Phys. Rev. B **75**, 045315 (2007).

[195] I. A. Ado, I. A. Dmitriev, O. P. M., and M. Titov, ArXiv:1504.03658 (2015).

[196] A. A. Burkov and D. G. Hawthorn, Phys. Rev. Lett. **105**, 066802 (2010).

[197] F. J. Morin, Phys. Rev. Lett. **3**, 34 (1959).

[198] A. Cavalleri and D. V. D. Linde, Applied Physics A **579**, 577 (1999).

[199] A. Cavalleri, C. Tóth, C. Siders, J. Squier, F. Ráksi, P. Forget, and J. Kieffer, Physical Review Letters **87**, 237401 (2001).

[200] A. Cavalleri, T. Dekorsy, H. Chong, J. Kieffer, and R. Schoenlein, Physical Review B **70**, 3 (2004).

[201] A. Cavalleri, M. Rini, H. Chong, S. Fourmaux, T. Glover, P. Heimann, J. Kieffer, and R. Schoenlein, Physical Review Letters **95**, 067405 (2005).

[202] P. Kim, private communication and unpublished (2006).

[203] M. Nakajima, N. Takubo, Z. Hiroi, Y. Ueda, and T. Suemoto, Journal of Luminescence **129**, 1802 (2009).

[204] T. L. Cocker, L. V. Titova, S. Fourmaux, H. C. Bandulet, D. Brassard, J. C. Kieffer, M. A. El Khakani, and F. A. Hegmann, Applied Physics Letters **97**, 221905 (2010).

[205] J. B. Goodenough, Journal of Solid State Chemistry **3**, 490 (1971).

[206] A. Zylbersztejn and N. F. Mott, Phys. Rev. B **11**, 4383 (1975), URL http://link.aps.org/doi/10.1103/PhysRevB.11.4383.

[207] J. P. Pouget, H. Launois, J. P. D'Haenens, P. Merenda, and T. M. Rice, Phys. Rev. Lett. **35**, 873 (1975), URL http://link.aps.org/doi/10.1103/PhysRevLett.35.873.

[208] V. Eyert, Annalen der Physik **514**, 650 (2002), arXiv:cond-mat/0210558.

[209] D. Paquet and P. Leroux-Hugon, Phys. Rev. B **22**, 5284 (1980).

[210] G. Stefanovich, A. Pergament, and D. Stefanovich, Journal of Physics: Condensed Matter **12**, 8837 (2000).

[211] M. M. Qazilbash, M. Brehm, B. G. Chae, P. C. Ho, G. O. Andreev, B. J. Kim, S. J. Yun, A. V. Balatsky, M. B. Maple, F. Keilmann, et al., Science **318**, 1750 (2007).

[212] L. Wang, I. Novikova, J. M. Klopf, S. Madaras, G. P. Williams, E. Madaras, J. Lu, S. A. Wolf, and R. A. Lukaszew, Advanced Optical Materials **2**, 30 (2014).

[213] M. F. Becker, A. B. Buckman, R. M. Walser, T. Lpine, P. Georges, and A. Brun, Applied Physics Letters **65**, 1507 (1994).

[214] C. Kübler, H. Ehrke, R. Huber, R. Lopez, A. Halabica, R. Haglund, and A. Leitenstorfer, Physical Review Letters **99**, 116401 (2007).

[215] D. J. Hilton, R. P. Prasankumar, S. Fourmaux, A. Cavalleri, D. Brassard, M. A. El Khakani, J. C. Kieffer, A. J. Taylor, and R. D. Averitt, Phys. Rev. Lett. **99**, 226401 (2007).

[216] M. Rini, Z. Hao, R. W. Schoenlein, C. Giannetti, F. Parmigiani, S. Fourmaux, J. C. Kieffer, A. Fujimori, M. Onoda, S. Wall, et al., Applied Physics Letters **92** (2008).

[217] A. Pashkin, C. Kübler, H. Ehrke, R. Lopez, A. Halabica, R. F. Haglund, R. Huber, and A. Leitenstorfer, Physical Review B **83**, 195120 (2011).

[218] E. Abreu, M. Liu, J. Lu, K. G. West, S. Kittiwatanakul, W. Yin, S. A. Wolf, and R. D. Averitt, New Journal of Physics **14**, 083026 (2012).

[219] T. L. Cocker, L. V. Titova, S. Fourmaux, G. Holloway, H.-C. Bandulet, D. Brassard, J.-C. Kieffer, M. A. El Khakani, and F. A. Hegmann, Physical Review B **85**, 155120 (2012).

[220] S. Wall, L. Foglia, D. Wegkamp, K. Appavoo, J. Nag, R. F. Haglund, J. Stähler, and M. Wolf, Phys. Rev. B **87**, 115126 (2013), URL `http://link.aps.org/doi/10.1103/PhysRevB.87.115126`.

[221] E. Radue, L. Wang, S. Kittiwatanakul, J. Lu, S. A. Wolf, E. Rossi, R. A. Lukaszew, and I. Novikova, Journal of Optics **17**, 025503 (2015).

[222] S. Lysenko, A. Rúa, V. Vikhnin, F. Fernández, and H. Liu, Phys. Rev. B **76**, 035104 (2007), URL `http://link.aps.org/doi/10.1103/PhysRevB.76.035104`.

[223] D. Brassard, S. Fourmaux, M. Jean-Jacques, J. C. Kieffer, and M. A. El Khakani, Applied Physics Letters **87**, 051910 (2005).

[224] R. Aliev, V. Andreev, V. Kapralova, V. Klimov, A. Sobolev, and E. Shadrin, Physics of the Solid State **48**, 929 (2006).

[225] K. G. West, J. Lu, J. Yu, D. Kirkwood, W. Chen, Y. Pei, J. Claassen, and S. a. Wolf, Journal of Vacuum Science & Technology A: Vacuum, Surfaces, and Films **26**, 133 (2008).

[226] L. Wang, E. Radue, S. Kittiwatanakul, C. Clavero, J. Lu, S. a. Wolf, I. Novikova, and R. a. Lukaszew, Optics letters **37**, 4335 (2012).

[227] E. Radue, E. Crisman, L. Wang, S. Kittiwatanakul, J. Lu, S. A. Wolf, R. Wincheski, R. A. Lukaszew, and I. Novikova, Journal of Applied Physics" **113**, 233104 (2013), URL `http://scitation.aip.org/content/aip/journal/jap/113/23/10.1063/1.4811689`.

[228] D. A. G. Bruggeman, Ann. Physik **416**, 636 (1935).

[229] R. Landauer, J. Appl. Phys. **23**, 779 (1952).

[230] X. C. Zeng, D. J. Bergman, P. M. Hui, and D. Stroud, Phys. Rev. B **38**, 10970 (1988).

[231] H. W. Verleur, A. S. Barker Jr, and C. N. Berglund, Physical Review **172**, 788 (1968).

[232] J. Kana Kana, J. Ndjaka, G. Vignaud, a. Gibaud, and M. Maaza, Optics Communications **284**, 807 (2011).

[233] C. G. Granqvist and R. A. Buhrman, Journal of Applied Physics **47**, 2200 (1976).

[234] M. E. Fisher and A. N. Berker, Phys. Rev. B **26**, 2507 (1982), URL `http://link.aps.org/doi/10.1103/PhysRevB.26.2507`.

[235] M. S. S. Challa, D. P. Landau, and K. Binder, Phys. Rev. B **34**, 1841 (1986), URL http://link.aps.org/doi/10.1103/PhysRevB.34.1841.

[236] M. Zhang, M. Y. Efremov, F. Schiettekatte, E. A. Olson, A. T. Kwan, S. L. Lai, T. Wisleder, J. E. Greene, and L. H. Allen, Phys. Rev. B **62**, 10548 (2000).

[237] Q. Jiang, J. Li, and B. Chi, Chemical Physics Letters **366** (2002).

[238] P. L. Kapitza, J. Phys. USSR **4** (1941).

[239] G. L. Pollack, Reviews of Modern Physics **41**, 48 (1969).

[240] R. Stoner and H. Maris, Physical review. B, Condensed matter **48**, 16373 (1993).

[241] H. Wen, L. Guo, E. Barnes, J. H. Lee, D. A. Walko, R. D. Schaller, J. A. Moyer, R. Misra, Y. Li, E. M. Dufresne, et al., Phys. Rev. B **88**, 165424 (2013).

[242] C. N. Berglund and H. J. Guggenheim, Phys. Rev. **185**, 1022 (1969).

[243] D.-W. Oh, C. Ko, S. Ramanathan, and D. G. Cahill, Applied Physics Letters **96**, 151906 (2010).

[244] D. de Ligny, P. Richet, E. F. W. Jr, and J. Roux, Physics and Chemistry of Minerals **29**, 267 (2002).

[245] W. R. Thurber and A. J. H. Mante, Phys. Rev. **139**, A1655 (1965).

[246] V. Pishchik, L. a. Lytvynov, and E. R. Dobrovinskaya, *Sapphire: Material, Manufacturing, Applications* (Springer US, 2009), 1st ed., ISBN 978-0-387-85694-0.

VITA

Martin Rodriguez-Vega

Martin is a physics student from Colima, Mexico. He earned his Bachelor of Science at the Universidad de Colima, Mexico in 2011. After that, he started his graduate studies at William and Mary working on condensed matter physics under the supervision of Professor Enrico Rossi. His dissertation focuses on the study of disorder effects in Dirac heterostructures. After graduation, he will work as a postdoc in the condensed matter theory group at Indiana University.